Doctoral Dissertation

Study on advanced electrolytes for improving electrochemical performance of sodium and lithium metal batteries

Yongwon Lee

Department of Energy Engineering
(Battery Science and Technology)

Graduate School of UNIST

2019

Study on advanced electrolytes for improving electrochemical performance of sodium and lithium metal batteries

Yongwon Lee

Department of Energy Engineering
(Battery Science and Technology)

Graduate School of UNIST

Study on advanced electrolytes for improving electrochemical performance of sodium and lithium metal batteries

A dissertation
submitted to the Graduate School of UNIST
in partial fulfillment of the
requirements for the degree of
Doctor of Philosophy

Yongwon Lee

12. 14. 2018
Approved by

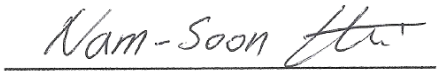

Advisor
Nam-Soon Choi

Study on advanced electrolytes for improving electrochemical performance of sodium and lithium metal batteries

Yongwon Lee

This certifies that the dissertation of Yongwon Lee is approved.

12. 14. 2018

Nam-Soon Choi

Advisor: Nam-Soon Choi

Kyeong-Min Jeong

Sung You Hong

Seok Ju Kang

Hyun-Wook Lee

Abstract

Alkali metals such as lithium (Li) and sodium (Na) have been considered as an ideal anode for rechargeable batteries in next generation. Li metal has the high specific capacity of 3860 mAh g^{-1} with reduction potential of -3.04 (versus standard hydrogen electrode) and low density of 0.534 g cm^{-3}. And Na metal has the high specific capacity of 1165 mAh g^{-1} with reduction potential of -2.71 V (versus standard hydrogen electrode). Nevertheless, the practical application of Na metal and Li metal batteries is quite challenging because the high chemical and electrochemical reactivity of Na metal and Li metal electrodes with organic liquid electrolytes leads to low Coulombic efficiencies and limited cycling performance. Severe electrolyte decomposition at the reactive metal electrode results in the formation of a resistive and nonuniform surface film, leading to dendritic metal growth. To control the Na metal and Li metal electrode−electrolyte interfaces for high performance Na metal and Li metal batteries, considerable efforts will be made to find electrolyte systems that are stable at the metal electrode. Moreover, the underlying mechanism of electrolytes at the electrode−electrolyte interface will be clearly elucidated through electrochemical method and characterization of the electrode−electrolyte interface.

I) For the electrolytes of Na metal batteries, degradation mechanism of Na metal in conventional carbonate–based electrolyte is studied. To mitigate the parasitic reaction between Na metal anode and electrolyte, fluoroethylene carbonate (FEC) is employed as additive and solvent in electrolyte to construct the protective layer on Na metal anode. The underlying mechanism of FEC at the electrode–electrolyte interface is clearly demonstrated by ^{13}C nuclear magnetic resonance, X-ray photoelectron spectroscopy, in–situ differential electrochemical microscopy and in–situ optical microscopy.

II) For the electrolytes of Li metal batteries, fluorinated compounds can be employed as interface modifiers to extend the applicable voltage range of ether-based electrolytes, which are commonly used in Li metal batteries with charging cut-off voltages of lower than 4 V (*vs.* Li/Li^+). In particular, we reveal that 1,1,2,2-tetrafluoroethyl-2,2,3,3-tetrafluoropropyl ether promotes the construction of a solid electrolyte interphase as a shield accommodating the destructive stress induced by Li plating and stripping on the Li metal anode, while FEC makes the interface of the Ni-rich cathode electrochemically robust and prevents severe intergranular cracking of the cathode during pre-cycling. Thus, this study provides a promising method of tackling the reductive and oxidative decomposition of labile ether-based electrolytes and allows one to enhance the electrochemical performance of Li metal anodes and Ni-rich cathodes.

Contents

List of Figures

and (f) DEC+FEC-added electrolytes during precycling at a current rate of C/20 and 30 °C. For comparison, voltage profiles of the $Na_4Fe_3(PO_4)_2(P_2O_7)$ cathode in the Ref electrolyte are represented by black dashed lines.

Fig. 2.10 Photographs of Na metal electrodes and GFF separators (a) without FEC and (b) with FEC after precycling at a rate of C/20.

Fig. 2.11 Cycling performance and Coulombic efficiency of $Na_4Fe_3(PO_4)_2(P_2O_7)$ cathodes with (a,b) DMC-added electrolyte or DMC+FEC-added electrolyte, (c,d) EMC-added electrolyte or EMC+FEC-added electrolyte, and (e,f) DEC-added electrolyte or DEC+FEC-added electrolyte at a current rate of C/2 and 30 °C. Filled and empty symbols represent charge and discharge capacities, respectively.

Fig. 2.12 F 1s XPS spectra of the $Na_4Fe_3(PO_4)_2(P_2O_7)$ cathodes precycled in (a) Ref electrolyte with FEC (FEC-added electrolyte), (b) DMC+FEC-added electrolyte, (c) EMC+FEC-added electrolyte, and (d) DEC+FEC-added electrolyte. Black dashed line represents the pristine (non-cycled) cathode. (e) Cycling performance and (f) Coulombic efficiency of $Na/Na_4Fe_3(PO_4)_2(P_2O_7)$ cells cycled in DEC+FEC-added electrolyte with a PE separator during 300 cycles at a current rate of C/2 and 30 °C.

Fig. 2.13 P 2p XPS spectra of the $Na_4Fe_3(PO_4)_2(P_2O_7)$ cathodes precycled in (a) Ref electrolyte with FEC, (b) DMC+FEC-added electrolyte. Black dashed line represents the pristine (non-cycled) cathode.

Fig. 2.14 Photographs of Na metal electrodes and GFF separators cycled in electrolytes (a) without FEC, (b) with FEC after 100 cycles at a rate of C/2.

Fig. 2.15 (a) Cycling performance (filled symbols for charge capacity and empty symbols for discharge capacity) and (b) Coulombic efficiency of $Na_4Fe_3(PO_4)_2(P_2O_7)$/Na half cells with DEC+FEC-added electrolytes during 50 cycles at a rate of C/2. GFF (red) or PE (blue) was used as a separator.

Fig. 3.1 HOMO-LUMO energy level diagram of conventional carbonates, FEC, and DME. μ_A and μ_C indicate the Fermi level of the Na metal anode and sodium-containing cathode, respectively. For the ab initio calculation, molecular optimization was carried out using density functional theory (DFT) at the B3LYP/6-311+G level of theory.

Fig. 3.2 (a) The Coulombic efficiency of Na/Cu coin-type cells in 1 M NaFSI-EC/PC (1/1), 1 M NaFSI-EC/PC (1/1) + 1 wt.% FEC and 1 M NaFSI-FEC at 0.28 mA cm^{-2}. (b) Rate capability of Na/Cu coin-type cells evaluated at the same current density for the Na plating and stripping process. (c) The electrochemical characteristics and physical properties of 1 M NaFSI in EC/PC (1/1) or FEC. Optical images showing in situ plated Na metal on a Cu substrate and voltage profiles during the initial Na plating process in (d) 1 M NaFSI-EC/PC (1/1) and (e) 1 M NaFSI-FEC at 0.28 mA cm^{-2} and 25 °C. Schematic drawing of Na deposition at the beginning of the Na plating process in (f) 1 M NaFSI-EC/PC

(1/1) and (g) 1 M NaFSI-FEC.

Fig. 3.3 (a) Voltage profiles for initial Na plating/stripping of Na/Cu cells in 1 M NaFSI-EC/PC (1/1) with 0, 1, 5, or 10 wt.% FEC and 1 M NaFSI-FEC at 0.056 mA cm^{-2} under 25 °C. The inset displays ICE as a function of FEC content. (b) Coulombic efficiency of Na/Cu cells at 0.282 mA cm^{-2} is shown. The areal capacity utilized from the counter Na metal electrode was 0.56 mAh cm^{-2}. Coulombic efficiency of Na/Cu cells in (c) FEC-free electrolytes and (d) FEC-containing electrolytes at 25 °C and 0.056 mA cm^{-2} over 15 cycles. (e) Coulombic efficiency of Na/Cu cells in 1 M $NaClO_4$-EC/PC (1/1)+1 wt.% FEC at 25 °C and current densities of 0.056, 0.169 and 0.282 mA cm^{-2}. Cell failure indicates that the cell voltage does not reach the cut-off condition of 1 V versus Na/Na^+ because of a short circuit by the formation and severe growth of Na dendrites on Na metal.

Fig. 3.4 Voltage variation for Na plating and stripping reactions at 0.28 mA cm^{-2} during 100 cycles. Voltages for Na plating and stripping are gradually decreased in 1M NaFSI-EC/PC (1/1). 1M NaFSI-FEC exhibits very stable voltage values. The areal capacity utilized from the counter Na metal electrode was 0.56 mAh cm^{-2}. Average voltage in plateau of Na plating and stripping is calculated.

Fig. 3.5 FT-IR spectra in the FEC ring breathing mode with an increase of NaFSI concentration and the fraction of solvated FEC coordinating with Na^+ ions.

Fig. 3.6 (a) The initial Coulombic efficiency of Na/Cu coin-type cells with 1 M NaFSI-FEC and 1M NaFSI-EC/PC (1/1) at a current density of 0.5 mA cm^{-2}. (b) Capacity retention and (c) Coulombic efficiency of Na/Cu cells at various areal capacities of 1, 3 and 5 mAh cm^{-2}. The cells were cycled at 1 mA cm^{-2}.

Fig. 3.7 Voltage profiles of initial Na plating on a Cu substrate in Na/Cu beaker cells and snapshot of Na metal plated on Cu substrates at specific points. Na plating was performed at 0.282 mA cm^{-2} under 25 °C. Voltage profile of a Na/Cu cell with (a) 1 M NaFSI-EC/PC (1/1) or (b) 1 M NaFSI-FEC is shown. (c) Non-uniform and thick Na metal deposition appears for 1 M NaFSI-EC/PC (1/1). (d) Uniform Na metal plating occurs in 1 M NaFSI-FEC. The areal capacity utilized from the counter Na metal electrode was 2.82 mAh cm^{-2}.

Fig. 3.8 (a) Galvanostatic cycling of Na/Na symmetric cells at various current densities of 0.056, 0.169, 0.282, 0.565, 1.69, 2.82 and 5.65 mA cm^{-2}. (b) Enlarged region showing the voltage profiles for the 96th to 100th cycle at 5.65 mA cm^{-2}.

Fig. 3.9 (a) Schematic of the in situ optical microscopy setup for monitoring Na metal deposition. (b) Electrochemical impedance spectra of the two cells using 1 M NaFSI-EC/PC (1/1) and 1 M NaFSI-FEC electrolytes. (c) Magnification of the electrochemical impedance spectra in (b) to compare the intrinsic resistance of the two cells. (d) The average height and standard deviation of the Na deposition as a

function of time for the two cells during the initial Na plating at 0.463 mA cm^{-2}. Cross-sectional optical images of Na plated on Cu substrates with (e) 1 M NaFSI-EC/PC (1/1) and (f) 1 M NaFSI-FEC obtained using in situ optical microscopy. All white scale bars represent 500 μm.

Fig. 3.10 Voltage profiles of Na deposition on the two cells, corresponding to the snapshots in Fig 3.9e and f.

Fig. 3.11 Surface morphology of Na metal electrochemically plated on a Cu substrate in (a) 1 M NaFSI-EC/PC (1/1) and (b) 1 M NaFSI-FEC at 0.28 mA cm^{-2} during the initial Na plating process. The insets of (a) and (b) show optical images of Na metal plated on a Cu substrate.

Fig. 3.12 Cross-sectional SEM images of Na deposits on a Cu substrate in a coin-type Na/Cu cell with (a) 1 M NaFSI-EC/PC (1/1) or (b) 1 M NaFSI-FEC after initial Na plating at 0.28 mA cm^{-2}. Surface morphology of Na deposits with (c) 1 M NaFSI-EC/PC or (d) 1 M NaFSI-FEC after initial Na plating at 0.28 mA cm^{-2} and Na plating during 2 cycles at 1.41 mA cm^{-2}. The areal capacity utilized from the counter Na metal electrode was 2.82 mAh cm^{-2}. F 1s XPS spectra of Na metal surface electrochemically plated on a Cu substrate with (e) 1M NaFSI-EC/PC or (f) 1M NaFSI-FEC during the initial Na plating at 0.28 mA cm^{-2} and Na plating during 2 cycles at 1.41 mA cm^{-2}.

Fig. 3.13 Surface morphology of Na metal electrochemically plated on a Cu substrate in 1 M NaFSI-EC/PC (1/1) and 1 M NaFSI-FEC at current densities of 0.28, 1, 5 and 10 mA cm^{-2} during the initial Na plating process. The areal capacity utilized from the counter Na metal electrode was 2.8 mAh cm^{-2}.

Fig. 3.14 Side-view images of Na metal electrochemically plated on a Cu substrate in 1 M NaFSI-EC/PC (1/1) and 1 M NaFSI-FEC at a high current density of 10 mA cm^{-2} during the initial Na plating process. The areal capacity utilized from the counter Na metal electrode was 2.8 mAh cm^{-2}.

Fig. 3.15 Surface morphology of Na metal electrochemically plated on a Cu substrate in 1 M NaFSI-EC/PC (1/1) and 1 M NaFSI-FEC at a current density of 0.5 mA cm^{-2} during the initial Na plating process. The areal capacities utilized from the counter Na metal electrode were 1, 3 and 5 mAh cm^{-2}.

Fig. 3.16 The C 1s, F 1s and N 1s core level spectra of Na metal surface electrochemically plated on a Cu substrate during the initial Na plating at a current density of 0.28 mA cm^{-2}.

Fig. 3.17 Possible mechanisms for the construction of the FEC-derived interlayer. The reductive decomposition reactions of FEC molecules for the formation of ionic compounds possessing carbonyl-functionalized moieties, such as -OCO_2CO_2- and -OCO_2-, highlighted in green, and NaF as main interlayer components.

Fig. 3.18 Typical force–distance loading curves corresponding to indent locations on the EC/PC- or FEC-derived interlayer formed on the Cu substrate during initial Na plating process at 0.28 mA cm^{-2}. A

cathodic current (0.28 mA cm^{-2}) was applied during 70 s for EC/PC-1M NaFSI and 60 s for FEC-1M NaFSI with negligible Na plating.

Fig. 3.19 In situ DEMS analysis of gas evolution in the Na|electrolyte|Cu cell configuration. Voltage profiles and in situ DEMS data for C_2H_4, H_2, CO_2, C_2H_2, and HF gases in the Na/Cu cells during the initial Na plating in (a) 1 M NaFSI-EC/PC (1/1) and (b) 1 M NaFSI-FEC at 0.282 mA cm^{-2} under 25 °C. The insets show the possible decomposition mechanisms of EC and FEC, which are subject to gas evolution. The OCV represents the open circuit voltage.

Fig. 3.20 Surface structure characterization of Na deposits by XPS. C 1s core level of Na metal plated on a Cu substrate with 1 M NaFSI-FEC and 1 M NaFSI-VC. The initial Na plating was carried out at 0.28 mA cm^{-2} and the areal capacity utilized from the Na metal electrode was 2.82 mAh cm^{-2}.

Fig. 3.21 (a) Voltage profiles for initial Na plating and stripping process in Na/Cu cells at 0.056 mA cm^{-2}. (b) Coulombic efficiency of Na/Cu cells at 0.28 mA cm^{-2}. The areal capacity utilized from the counter Na metal electrode was 0.56 mAh cm^{-2}. The electrochemical performance of Na/Cu cells with 1 M NaFSI-vinylene carbonate (VC) was evaluated at 25 °C to verify that the use of reducible compounds as the main solvent assures good cycling performances of Na metal electrodes without cell failure.

Fig. 3.22 Surface structure characterization of fully sodiated hard carbon anodes by XPS. C 1s core level of the surface of hard carbon electrode with 1 M NaFSI-FEC or 1 M NaFSI-EC/PC (1/1) is compared after full sodiation at 0.045 mA cm^{-2}. The Na plating on Cu substrate was carried out at 0.28 mA cm^{-2}. The areal capacity utilized from the Na metal electrode was 2.82 mAh cm^{-2}.

Fig. 4.1 HOMO-LUMO energy level of 1,2-dimethoxyethane (DME), ethylene carbonate (EC), fluoroethylene carbonate (FEC) and 1,1,2,2-tetrafluoroethyl-2,2,3,3-tetrafluoropropyl ether (TTE) in neutral charge of molecule through density functional theory (DFT) calculation.

Fig. 4.2 HOMO-LUMO energy level of DME, EC, FEC and TTE in singly negatively charged states through DFT calculation. +1e and –1e represents that molecule accepts and loses one electron, respectively. Gray, white, red, and cyan spheres denote C, H, O, and F atoms, respectively.

Fig. 4.3 (a) Voltage profiles for the initial Li plating and stripping reactions in Li/Cu cells with various electrolytes at a current density of 0.2 mA cm^{-2} and 25 °C. (b) Coulombic efficiency of Li/Cu cells at a current density of 1 mA cm^{-2} and 25 °C. Voltage profiles of Li/Cu cells in (c) DME (3M LiFSI-DME), (d) DME+FEC (3M LiFSI-DME+1% FEC), (e) DME+TTE+FEC (3M LiFSI-DME/TTE (8/2)+1% FEC) and (f) Carbonate+FEC (1.15M $LiPF_6$-EC/EMC/DEC (2/5/3)+1% FEC). The areal capacity utilized from the counter Li metal electrode was 2 mAh cm^{-2}.

Fig. 4.4 Voltage profiles for the initial Li plating and stripping reactions in Li|Cu cells with various

electrolytes at a current density of 0.2 mA cm^{-2} and 25 °C (DME+TTE: 3M LiFSI-DME/TTE (8/2)).

Fig. 4.5 Adsorption energy of (a) FEC and (b) TTE on Li(001) surface. LUMO energy level of (c) adsorbed FEC and (d) TTE on Li(001) surface.

Fig. 4.6 dQ/dV curves of Cu|NCM811 cells in DME+FEC, DME+TTE and DME+TTE+FEC electrolyte at 0.05 mA cm^{-2}. Schematic showing the effect of FEC regulating the decomposition of TTE

Fig. 4.7 TOF-SIMS LiF^- ion maps of Li metal contacting (a) neat FEC and (b) neat TTE at 25 °C for 1 day. Schematic illustration of decomposition of (c) FEC and (d) TTE on Li metal anode. Relative Gibbs free energy (ΔG) diagram for the reduction of (e) FEC and (f) TTE molecules. Gray, white, red and cyan spheres denote C, H, O and F atoms, respectively. F 1s XPS spectra of Li metal in Li/NCM cell with (g) DME+FEC electrolyte and (h) DME+TTE+FEC electrolyte after precycle at a rate of 0.1C.

Fig. 4.8 TOF-SIMS LiF^- ion maps of Li metal anodes retrieved from Li|NCM811 full cells precycled in (a) DME, (b) DME+FEC, (c) DME+TTE, (d) DME+TTE+FEC using at a 0.1C rate and 25 °C.

Fig. 4.9 Scheme showing the unique feature of TTE constructing SEI on Li metal at initial Li plating and repairing damaged SEI during cycling. FEC, which favorably adsorbed on the Li metal thanks to its low adsorption energy, tunes the reductive decomposition of TTE on the Li metal.

Fig. 4.10 SEM images of Li deposits on Cu substrate in (a, e) DME, (b, f) DME+FEC, (c, g) DME+TTE+FEC and (d, h) Carbonate+FEC electrolyte at a current density of 0.2 mA cm^{-2}. (a, b, c, d : top-view, e, f, g, h : side-view) The areal capacity utilized from the counter Li metal electrode was 2 mAh cm^{-2}. Scale bars in (a-d) and (e-h) are 50 μm and 20 μm, respectively.

Fig. 4.11 Electrochemical performance of Li|NCM811 full cells. (a) Voltage profiles during pre-cycling at a 0.1C rate and 25 °C. (b) Specific discharge capacity of Li|NCM811 full cells at a 0.5C rate and 25 °C. Foil-type Li metal with thickness of 100 μm was employed as an anode. (c) Voltage profile and hysteresis of charge and discharge at 90^{th} cycle. (d) Specific discharge capacity and Coulombic efficiency of Li|NCM811 full cells with 20 μm Li metal anode in DME+TTE+ FEC electrolyte at a 0.5C rate and 25 °C. (e) Interfacial engineering function of TTE and FEC protecting electrode interfaces in Li|NCM811 full cells.

Fig. 4.12 Electrochemical performance of Li|NCM811 cell in precycle and wetting property of electrolytes toward the NCM811 cathodes and separators. (a) Initial Coulombic efficiency of Li|NCM811 full cells at a 0.1C rate and 25 °C. (b) Contact angle of the electrolyte on the NCM811 cathode and photographs of the separators after there one side were immersed in the electrolytes for 2 min.

Fig. 4.13 Coulombic efficiency of Li/NCM cells at a rate of 0.5C and 25 °C.

Fig. 4.14 Specific discharge capacity and Coulombic efficiency of Li/NCM cells at a rate of 0.5C and 25 °C.

Fig. 4.15 Anodic stability of electrolytes on an SS working electrode at a scan rate of 1 mV s^{-1}.

Fig. 4.16 (a) Specific discharge capacity and (b) Coulombic efficiency of Li/NCM cells at a rate of 0.1C and 25 °C.

Fig. 4.17 Charge-discharge voltage profiles (top) and enlarged voltage profiles (bottom) of Li/NCM cells at 1^{st}, 10^{th} and 100^{th} cycle.

Fig. 4.18 Potentiostatic profiles of Li/NCM cells at a constant voltage of 4.2V during 11^{th} charge process after 10 cycles at a rate of 0.5C.

Fig. 4.19 Cross-sectional SEM images of NCM811 cathode. (a, b) pristine NCM811 cathode. Cycled NCM811 cathodes retrieved from Li|NCM811 cells with (c, d) DME, (e, f) DME+FEC, and (g, h) DME+TTE+FEC electrolyte after 20 cycles at a 0.5C rate and 25 °C. ΔT is the change in thickness of the NCM811 cathodes after cycling. Yellow arrows indicate microcracking of secondary NCM811 particles induced by roll pressing process. Schematic illustration of (i) the interfacial degradation of the NCM811 cathode in DME electrolyte and (j) robust and uniform CEI constructed by TTE+FEC.

Fig. 4.20 F 1s XPS spectra of NCM cathode in Li/NCM cell with (a) DME electrolyte, (b) DME+FEC electrolyte and (c) DME+TTE+FEC electrolyte after precycle at a rate of 0.1C.

Fig. 4.21 Transition metal dissolution of NCM811 cathode. (a) Schematic of sample preparation procedure for ICP analysis. (b) Amounts of transition metal (Co, Mn and Ni) dissolved in the electrolyte storing with fully charged NCM811 cathode up to 4.2 V *vs.* Li/Li^+ at 60 °C for 24 h. (DM+FEC: 3M LiFSI-DME/TTE (8/2)+1% FEC, $LiPF_6$-based: 1.15M $LiPF_6$-EC/EMC/DEC (2/5/3))

List of Tables

I. Introduction

1.1 Na metal batteries

Na metal batteries have been gained considerable attention as promising next-generation rechargeable batteries, especially for large-scale energy storage systems (ESS), because of the natural abundance of Na, the high theoretical specific capacity (1165 mAh g^{-1}) and low redox potential (-2.71 V versus standard hydrogen electrode).[1-3] Much efforts have been exerted to improve electrochemical performance of Na metal batteries through cathode side such as S and O_2.[4-6] But the problem on Na metal anode side is unresolved due to high electrochemical and chemical reactivity of Na metal electrode toward liquid electrolytes.[7] Highly reactive Na metal electrode leads to low Coulombic efficiency and poor cyclability. Liquid electrolytes react with Na metal surface and decomposes to form resistive and non-uniform passivation layer on Na metal surface. Resistive passivation layer on Na metal influences the impedance of Na metal electrode resulting in polarization.[8-9] Non-uniform surface film also causes dendritic growth of Na metal (Fig. 1.1).[10] Dendritic Na dissolves from the base of needles on the Na metal during Na stripping from Na deposits and detaches from Na metal. This isolated Na, known as 'dead Na' is electrochemically inactive and leads limited cycle life of Na metal batteries.[11] Recently, Jang et al. elucidated that the linear carbonate diethyl carbonate (DEC), in EC/DEC/1 M $NaClO_4$, reacts with the Na metal electrode; the resulting decomposition products, such as active radicals ($R–CH_2·$, R=H or CH_3) and sodium alkyl carbonates ($R'OCO_2Na$), diffuse to the cathode and stimulate electrolyte decomposition at high potentials of around 4.2 V (*vs.* Na/Na^+).[12] To build stable solid electrolyte interphase (SEI) layer on Na metal, fluoroethylene carbonate (FEC) was added into electrolytes.[7] FEC-derived SEI layer mitigates reactivity of Na metal. Thus, parasitic reaction between Na metal and electrolyte is effectively reduced.

Herein, we study the degradation mechanism of Na metal toward liquid electrolyte. The underlying reaction mechanism of electrolyte decomposition on Ne metal anode is clearly demonstrated with ^{13}C nuclear magnetic resonance study and X-ray photoelectron spectroscopy in chapter II (Highly stable linear carbonate-containing electrolytes with fluoroethylene carbonate for high-performance cathodes in sodium-ion batteries). In chapter III (Fluoroethylene carbonate-based electrolyte with 1 M sodium bis(fluorosulfonyl)imide enables high-performance sodium metal electrodes), evolution of dendritic Na and the structure of Na metal–electrolyte interphase are observed with in-situ optical microscopy and ex-situ XPS, respectively. we demonstrate a FEC-based electrolyte with 1M sodium bis(fluorosulfonyl)imide (NaFSI) salt for the stable and dense deposition of the Na metal during electrochemical cycling. The novel electrolyte combination developed here circumvents the dendritic Na deposition that is one of the primary concerns for battery safety and constructs the uniform ionic

interlayer achieving highly reversible Na plating/stripping reactions. The FEC−NaFSI constructs the mechanically strong and ion-permeable interlayer containing NaF and ionic compounds such as Na_2CO_3 and sodium alkylcarbonates.

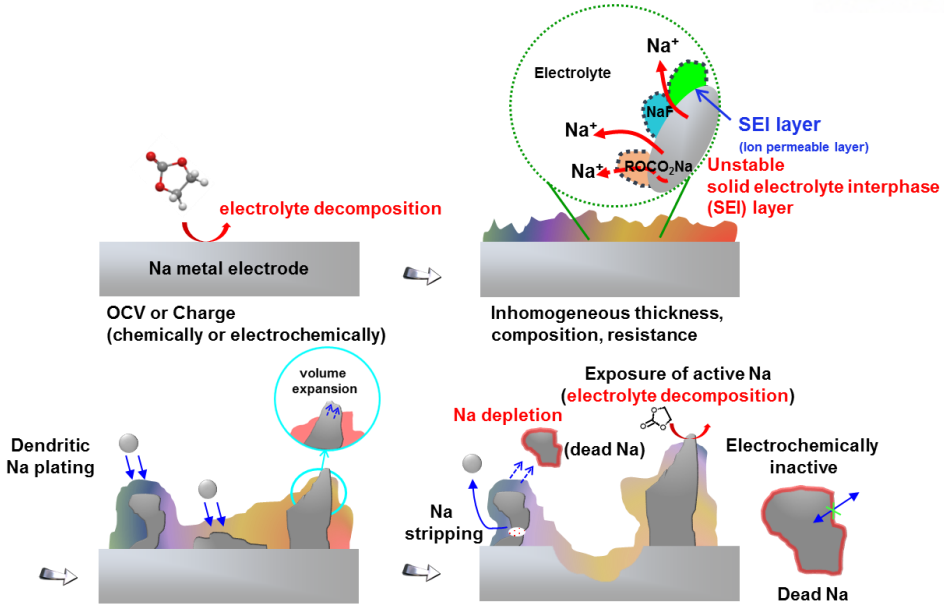

Fig. 1.1 Schematic illustration showing the formation of dendritic Na and dead Na induced inhomogeneous solid electrolyte interphase (SEI) on Na metal electrode.

1.2 Li metal batteries

Li metal has been regarded as an ideal anode for energy storage system because it has high theoretical specific capacity (3860 mAh g^{-1}) and the most negative electrochemical potential (-3.04 V versus standard hydrogen electrode) and it is the lightest metal (0.534 g cm^{-3}).[13] However, dendritic growth of Li and low Coulombic efficiency of Li plating and stripping reaction impede the practical application of Li metal on battery due to safety concerns and low lifespan of battery.[14-15] Formation of undesirable SEI on Li metal is one of the governing factors aggravating dendritic growth of Li and low CE.[16-17] Non-aqueous electrolyte is promptly decomposed on Li metal with highly reducing environment, constructing heterogenous and resistive SEI layer on Li metal. It generates uneven distribution of current density on Li metal leading dendritic growth of Li.[17-18] Moreover, interfacial fluctuation of vulnerable SEI layer due to volume change of Li metal anode during repeated Li plating and stripping can cause expose the active Li metal surface resulting in further decomposition of electrolytes. FEC additive could form compact and stable SEI layer on Li metal anode, mitigating uncontrollable dendritic growth of Li.[19-22] Especially, highly concentrated lithium bis(fluorosulfonyl)imide (LiFSI) with 1,2-dimethoxyethane (DME) electrolytes which remarkably prevented growth of dendritic Li and enhanced the electrochemical performance of Li metal batteries are feasible electrolyte composition for utilizing Li metal anode.[23] However, ether-based electrolytes cannot be used in Li batteries with 4V class cathodes, mainly because of the low upper voltage limits (<4 V *vs.* Li/Li^+) and high flammability of ethers.[24] Bis(2,2,2-trifluoroethyl) ether-added electrolytes displayed good compatibility toward 4 V-class $LiNi_{1/3}Mn_{1/3}Co_{1/3}O_2$ cathode and achieved improved cycle performance of $Li/LiNi_{1/3}Mn_{1/3}Co_{1/3}O_2$ cells with high CE of ca. 99.5% and capacity retention of >80% after 700 cycles.[25] Recently, it was demonstrated that strong Lewis basicity of ethers, which readily lose their oxygen lone pair electrons at high voltages, can be modulated by the coordination with high concentration of Li ions lowering highest occupied molecular orbital (HOMO) energy levels of ethers. This decreased HOMO energy indicates that the oxidation durability of ethers at high voltages is enhanced.[26] Although highly concentrated electrolytes inhibited growth of dendritic Li and enhanced cycling performance of Li metal anodes,[23, 27] their unsatisfactory adoptability with 4 V-class cathodes hampers practical viability of Li metal batteries. Furthermore, the introduction of electrolyte additives constructing protective layer on the surface directly above cathode can prevent the direct contact of ethers with the cathode resulting in the alleviation of unwanted oxidative decomposition of ethers.[28-29] Because severe and inhomogeneous volume changes of Li metal anodes induced by repeated Li plating and stripping reactions inflict volumetric stress on the interface, highly stress-tolerant interlayer with good ion permeability is strictly required to circumvent critical issues such as dendritic Li growth and significant CE decay of Li metal electrodes. It is noteworthy that achievement of high CE is indispensable the conservation of limited

amount of Li metal anodes and long cycle life of Li metal batteries coupled with 4 V-class cathodes. However, to date, finding electrolytes with good compatibility toward the 4 V-class cathodes as well as the protection the bare Li metal anode without Li dendrite growth has remained elusive.

In chapter IV (Fluorine-enriched interfaces enhance cycling stability of 4 V class Li metal batteries in ether-based electrolytes), we show that the use of concentrated electrolytes containing 1,1,2,2-tetrafluoroethyl-2,2,3,3-tetrafluoropropyl ether (TTE) as co-solvent and FEC as additive allows for homogeneous and reversible reactions at Li metal anodes and results in improved anodic stability at high-capacity Ni-rich cathodes with charging cut-off voltages of >4 V *vs.* Li/Li^+. Notably, TTE promotes the formation of a stable interlayer that helps to protect the reactive Li metal, while FEC manipulates the structure of the cathode-electrolyte interface to mitigate the mechanical cracking of Ni-rich secondary particles. Furthermore, we suggest a mechanistic explanation of how TTE-promoted solid electrolyte interphase formation preserves the electrochemical reversibility of Li metal and use cross-sectional imaging to rationalize the ability of FEC to maintain the mechanical integrity of the Ni-rich cathode.

II. Highly stable linear carbonate-containing electrolytes with fluoroethylene carbonate for high-performance cathodes in sodium-ion batteries

2.1 Introduction

In most studies for sodium-ion batteries (SIBs) are composed of polar solvents such as ethylene carbonate (EC) and propylene carbonate (PC).[30] Accordingly, instead of commercially available polyethylene (PE) membranes, glass fiber filters (GFFs), which easily uptake polar solvents, have been used as separators for SIBs. However, the too thick, mechanically weak, and highly porous GFF is not suitable as a separator because it can reduce the volumetric energy density and cannot guarantee the safety of batteries. To readily absorb polar solvents with high dielectric constants, their inherent hydrophobic surfaces can be modified by using the surfactants. However, this treatment is temporary because the surfactants are washed away from the separator surface by the electrolyte solution upon the repeated cycling. For the introduction of a conventional PE separator into SIBs, the inclusion of linear carbonate as a cosolvent was attempted, motivated by the fact that this material has been widely used owing to its low viscosity and good compatibility with conventional PE separators. However, the use of linear carbonates such as dimethyl carbonate (DMC) has been limited because of their severe decomposition at the surface of Na metal electrodes and sodiated anodes in SIBs. The Komaba group demonstrated that hard carbon anodes with DMC-containing electrolyte exhibit significant capacity fading.[31] It was proposed that by-products resulting from unwanted reactions between linear carbonates and the Na metal electrode may move to a cathode during cycling and that the migrated byproducts can undergo oxidative decomposition at the cathode.[12] Jang et al. elucidated that the linear carbonate diethyl carbonate (DEC), in EC/DEC/1 M $NaClO_4$, reacts with the Na metal electrode; the resulting decomposition products, such as active radicals ($R–CH_2·$, R=H or CH_3) and sodium alkyl carbonates ($R'OCO_2Na$), diffuse to the cathode and stimulate electrolyte decomposition at high potentials of around 4.2 V (*vs.* Na/Na^+).[12] To properly design electrolyte systems for high-performance SIBs, the high reactivity of linear carbonates toward the Na metal electrode and sodiated anodes should be reduced. Recent studies have reported that fluoroethylene carbonate (FEC) as an additive improved the cycling performance of hard carbon anodes with linear carbonate-containing electrolytes.[7] It was mentioned that FEC readily decomposes on the anode prior to the reductive decomposition of linear carbonates and builds up a protective surface film. Several studies have shown positive effects of FEC on the interfacial stabilization of anodes.[32-34] In addition, the FEC additive improved the Coulombic efficiency of $NaNi_{1/2}Mn_{1/2}O_2$ cathodes through the suppression of the oxidative decomposition of byproducts generated by the electrolyte decomposition at the Na metal electrode.[35] Recently, our group

demonstrated that the byproducts produced from linear carbonate decomposition at the Na metal electrode in Na/$Na_4Fe_3(PO_4)_2(P_2O_7)$ half cells led to the degradation of the electrochemical performance of cathodes.[12] To avoid unwanted electrolyte decomposition on the surfaces of Na metal electrodes in half cells and at sodiated anodes in full cells, electrolyte additives for the formation of protective surface films should be introduced.[7, 36-39] There is no report for detailed failure mechanisms of linear carbonates in SIBs and the unique function of the FEC additive.

Herein, we provide linear carbonate-containing electrolytes with a FEC additive that could be utilized as a universal electrolyte system for high-performance SIBs to replace lithium-ion batteries. We clearly demonstrate the underlying reaction mechanisms of electrolyte decomposition at the Na metal electrode and the $Na_4Fe_3(PO_4)_2(P_2O_7)$ cathode charged up to high voltage of 4.2 V (*vs.* Na/Na^+) by means of ^{13}C nuclear magnetic resonance (NMR) study. Additionally, we propose a possible mechanism, which the FEC additive renders linear carbonate containing electrolytes stable at the Na metal electrode and improves the cycling performance of the cathodes.

2.2 Experimental method

Electrolytes and electrodes

The electrolytes were 0.5 M sodium perchlorate ($NaClO_4$, Aldrich, > 98.0%) dissolved in a solvent mixture of ethylene carbonate (EC)/propylene carbonate (PC) (5/5, v/v) or EC/PC/dimethyl carbonate (DMC) (5/3/2, v/v/v) or EC/PC/ethylmethyl carbonate (EMC) (5/3/2, v/v/v) or EC/PC/diethyl carbonate (DEC) (5/3/2, v/v/v). 5 wt% of FEC additive was introduced into each electrolyte. The composition of each electrolyte is listed in Table 2.1. All solvents (Soulbrain Co., Ltd.) were used as received. The $Na_4Fe_3(PO_4)_2(P_2O_7)$ cathode material was synthesized according to a procedure reported in the literature.[40] For the electrochemical tests, the electrode was prepared by spreading a slurry mixture of 70 wt% $Na_4Fe_3(PO_4)_2(P_2O_7)$ as an active material, 20 wt% super P as a conducting material, and 10 wt% polyvinylidene fluoride (PVDF) binder dissolved in anhydrous N-methyl-2-pyrrolidone (NMP, 99.5%, Aldrich) onto an aluminum (Al) foil. The slurry was dried in a convection oven at 110 °C for 1 h. After drying, the electrode was pressed and the thickness was around 50 μm. The electrodes were dried in vacuum at 120 °C for 2 h and at 80 °C for 2 h prior to their assembly into cells.

Table 2.1 Composition of electrolytes

Electrolyte	Salt	EC	PC	DMC	EMC	DEC
Ref	0.5M $NaClO_4$	5	5			
DMC-added		5	3	2		
EMC-added		5	3		2	
DEC-added		5	3			2

Electrochemical measurements

The anodic limits of the electrolytes were determined by means of linear sweep voltammetry (LSV) using an Iviumstat (Ivium Technologies, The Netherlands) at a scan rate of 1 mV/s; we used stainless steel as the working electrode and Na metal as the counter and reference electrodes. A 2032 coin-type half cell with an $Na_4Fe_3(PO_4)_2(P_2O_7)$ cathode, an Na metal electrode, and a glass fiber filter (GFF, Whatman, 260 μm thickness) or a polyethylene separator was assembled in an argon filled glove box with less than 1 ppm of both oxygen and moisture. Galvanostatic charge and discharge cycling (WonATech WBCS 3000) of the $Na_4Fe_3(PO_4)_2(P_2O_7)$ cells was performed in a potential window between 1.7 V and 4.2 V (*vs.* Na/Na^+). Precycling and cycling tests of the cells were carried out at rates of C/20 and C/2, respectively.

Characterization

The ionic conductivity and viscosity of the electrolytes were measured using an Oakton CON 11 standard conductivity meter and a BROOKFIELD viscometer (LVDV-ll + P), respectively, at room temperature. Contact angle measurements of the electrolytes on a polyethylene (PE, SK innovation Co. Ltd) separator were carried out using a KRUSS DSA100 apparatus within 5 s to minimize any possible contamination. The thickness and porosity of the microporous PE film used as a separator were 20 mm and 38%, respectively. To understand the reaction between the linear carbonate and the Na metal electrode, typical experiments were performed as follows. An Na metal electrode disk (1.77 cm^2) was soaked in a linear carbonate-containing electrolyte of 5 g under argon in a PE bottle; the PE bottle was stored in a glove box for 10 days at room temperature. ^{13}C nuclear magnetic resonance (NMR) spectra of the stored electrolytes were recorded on an Agilent (600 MHz, VNMRS 600) spectrometer using tetrahydrofuran (THF)-d_8 solvent. Ex situ X-ray photoelectron spectroscopy (XPS, Thermo Scientific K-Alpha System) measurements were performed on the dried cathodes using Al-Ka ($h\nu$ = 1486.6 eV) radiation under ultrahigh vacuum. XPS spectra were collected using a 0.10 eV step and an 80 eV pass energy. After precycling, the cells were carefully opened in a glove box to retrieve their cathodes. The cathodes were rinsed in dimethyl carbonate (DMC) to remove the residual electrolyte; the resulting electrodes were dried at room temperature for analysis by ex situ XPS.

2.3 Results and discussion

Fig. 2.1a shows the ionic conductivity and viscosity of the electrolytes at room temperature. The composition of each electrolyte is listed in Table 2.1. 0.5 M $NaClO_4$ in ethylene carbonate (EC)/propylene carbonate (PC) (5/5, v/v) (hereinafter referred to as "Ref" electrolyte) has a relatively high viscosity of 3.84 cP compared with those of other electrolytes. Since a high dielectric constant for salt dissociation and low viscosity for fast ion transport usually cannot be integrated into a single solvent, a solvent mixture with one of the components selected for dielectric constant and the other for viscosity was used to formulate the electrolytes. Moreover, for the introduction of linear carbonate, it is necessary to use a hydrophobic polyethylene (PE) separator. Linear carbonate-containing electrolytes exhibited enhanced ionic conductivities because the reduced viscosity of the electrolytes due to the addition of low viscous linear carbonates improved the movement of free ions in the electrolyte. The highest ionic conductivity of the electrolytes was achieved by the addition of dimethyl carbonate (DMC) with the lowest viscosity (0.55 cP), as shown in Fig. 2.1a. Ethylmethyl carbonate (EMC)-added (EC/PC/EMC (5/3/2, v/v/v)) and diethyl carbonate (DEC)-added (EC/PC/DEC (5/3/2, v/v/v)) electrolytes slightly reduced the ionic conductivities compared with those of the DMC-added (EC/PC/DMC (5/3/2, v/v/v)) electrolyte because the viscosity of EMC (0.62 cP) and DEC (0.76 cP) are higher than that of DMC. This indicates that the ionic conductivity of electrolytes with sufficient salt dissociation is most strongly affected by the viscosity of the electrolytes. Fig. 2.1b and c show the wettability and contact angle, respectively, of the electrolytes on a PE separator. Contact angle, which is one of the common ways to determine the wettability of a material, was measured to understand how the deposited liquid electrolyte spreads out on a PE separator. Ref electrolyte without linear carbonate solvents did not penetrate into the PE separator because polar solvents such as EC and PC are not compatible with the hydrophobic PE separator (Fig. 2.1b). However, the wettability of the electrolytes on the PE separator was drastically improved by adding linear carbonates such as DMC, EMC, and DEC. Interestingly, the best electrolyte wettability was observed for the DEC-added electrolyte, which showed a contact angle of 39.8° (Fig. 2.1c). To better understand the disparity in the wettability of electrolytes on the PE separators, a schematic representation depicting the effect of the chemical structure of the linear carbonates on the compatibility of the electrolytes on hydrophobic PE separators is given in Fig. 2.2. It is thought that the short hydrocarbon chains of DMC do not support interaction with the hydrophobic PE separator because the cohesive forces of the electrolyte are stronger than the adhesive forces toward the PE separator. The smaller contact angles of the EMC-added and DEC-added electrolytes indicate that the partially positively charged ethyl groups (CH_3CH_2–) of EMC and DEC are compatible with the hydrophobic PE separators and also their carbonate moieties (–OCO_2–) tend to interact with polar EC and PC solvents, as illustrated in Fig. 2.2. It can be thought that the hydrophobic alkyl chains of DMC, EMC, and DEC

act as a wetting agent to improve the wettability of the electrolytes toward the PE separator (Fig. 2.2).

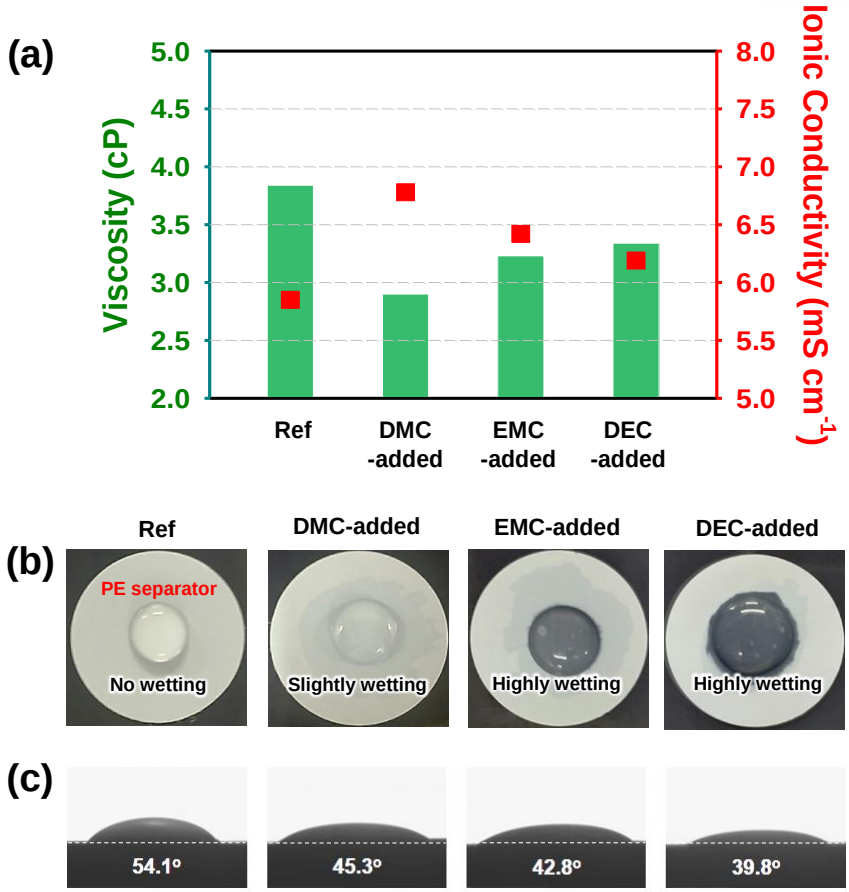

Fig. 2.1 (a) Viscosity and ionic conductivity of 0.5 M $NaClO_4$ in various carbonate solvent mixtures at room temperature. (b) Photographs of various electrolytes on PE separators in a dry room with an ultra low dew point of -56 °C. (c) Contact angle of the electrolytes on the PE separators.

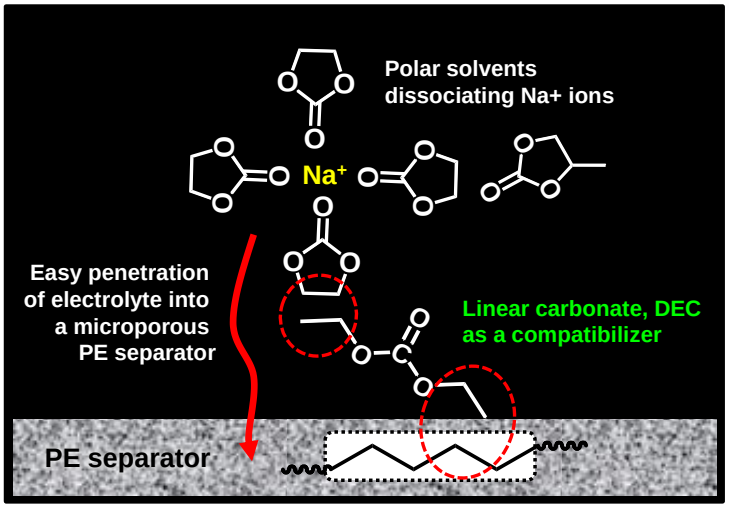

Fig. 2.2 Schematic representation of the improvement in the wettability of EC/PC-based electrolytes on PE separators by using linear carbonate (DEC) as a wetting agent.

The oxidation stability values of DMC-added, EMC-added, and DEC-added electrolytes with or without fluoroethylene carbonate (FEC) are displayed in Fig. 2.3. The Ref electrolyte started to oxidize at 4.5 V on a stainless steel (SS) working electrode, as shown in Fig. 2.3. The addition of DMC as a cosolvent generated an anodic current at around 3.7 V (*vs.* Na/Na^+) and led to appreciable oxidation currents at potentials greater than 4.6 V (*vs.* Na/Na^+). Recently, Komaba's group demonstrated that the EC/DEC-based electrolyte is very unstable against the highly reactive Na metal electrode and thereby loses its anodic stability at high voltages.[7] In this regard, it can be thought that DMC, a kind of linear carbonate, readily reacts with the Na metal electrode in a cell and the decomposed DMC becomes sodium alkyl carbonate, as depicted in Fig. 2.4a. The resulting sodium alkyl carbonate may participate in undesirable electrolyte decomposition at the cathode (Fig. 2.4a) and cause overcharge behavior of the cathode. The methyl radical ($CH_3\cdot$) species formed by the DMC decomposition leads to ring opening of the EC molecules; another sodium alkyl carbonate can be produced by the reaction of EC and the $CH_3\cdot$ radical. These sodium alkyl carbonates may undergo electrochemical oxidative decomposition at high voltages, as depicted in Fig. 2.4a. In addition, the $CH_3\cdot$ radical may accelerate the DMC-added electrolyte decomposition under high voltage conditions through recombination with the $ClO_4\cdot$ radical, which is formed by the oxidative decomposition of $ClO_4\cdot$. Although EMC-added and DEC-added electrolytes without the FEC additive did not produce appreciable oxidation currents at potentials lower than 4.6 V (*vs.* Na/Na^+), they showed relatively reduced overall anodic stability compared to that of the Ref electrolyte (Fig. 2.3b and c). Interestingly, the anodic stabilities of the DMC-added, EMC-added, and DEC-added electrolytes were discernibly improved by the addition of 5 wt% FEC, as shown in Fig. 2.3. To clarify the unwanted reactions between DMC and an Na metal electrode, the measurements of linear sweep voltammetry (LSV) of Na/SS and Li/SS cells with the DMC-added electrolyte were performed (Fig. 2.4b and c). The DMC-added electrolyte in an Na/SS cell started to generate the anodic currents at a relatively low potential of 3.7 V (*vs.* Na/Na^+) compared to the Ref electrolyte (Fig. 2.4b). On the contrary, the DMC-added electrolyte in a Li/SS cell did not generate appreciable anodic currents at around 4.0 V (*vs.* Li/Li^+) (corresponding to 3.7 V *vs.* Na/Na^+) and the anodic limit of the DMC-added electrolyte (Fig. 2.4c) was analogous with the Ref (DMC-free) electrolyte. This preliminary evidence indicates that DMC in the electrolyte undergoes irreversible decomposition at highly reactive Na metal electrode in Na/SS cells and the soluble by-products (DMC-d) formed by the DMC decomposition promote the oxidative decomposition of the electrolyte at high voltages. It should be noted that the electrolyte decomposition at high voltage conditions may generate the charge capacity, which is not related to the capacity of the cathode during a charge (desodiation) process. This phenomenon could be confirmed by a comparison of the voltage profiles of $Na/Na_4Fe_3(PO_4)_2(P_2O_7)$ and $Li/Na_4Fe_3(PO_4)_2(P_2O_7)$ cells with Ref or DMC-added electrolyte in the initial charge process. The DMC-added electrolyte

results in the overcharge behavior of the cathode in Na/$Na_4Fe_3(PO_4)_2(P_2O_7)$ cells, while this overcharge behavior was not observed for the cathode with the DMC-added electrolyte in Li/$Na_4Fe_3(PO_4)_2(P_2O_7)$ cells (Fig. 2.4d and e). From these results, the decomposition of DMC in the electrolyte at the Na metal electrode and the detrimental effect of formed by-products (DMC-d) on the anodic stability of the electrolyte appears to be a rational explanation. It is worth pointing out that coin-type half cells are stored during the given time at room temperature for the sufficient penetration of the electrolyte into the electrode and the Na metal electrode is inevitably exposed toward the electrolyte without applied potentials. This aging process for cells may lead to the formation of by-products produced by irreversible decomposition reactions of linear carbonates at the Na metal electrode. Among the formed by-products, soluble compounds may exist in the electrolyte and undergo the irreversible decomposition reactions at a cathode under an electric field. The undesirable decomposition of linear carbonates at the Na metal electrode in half cells is thought to be more severe during cycling.

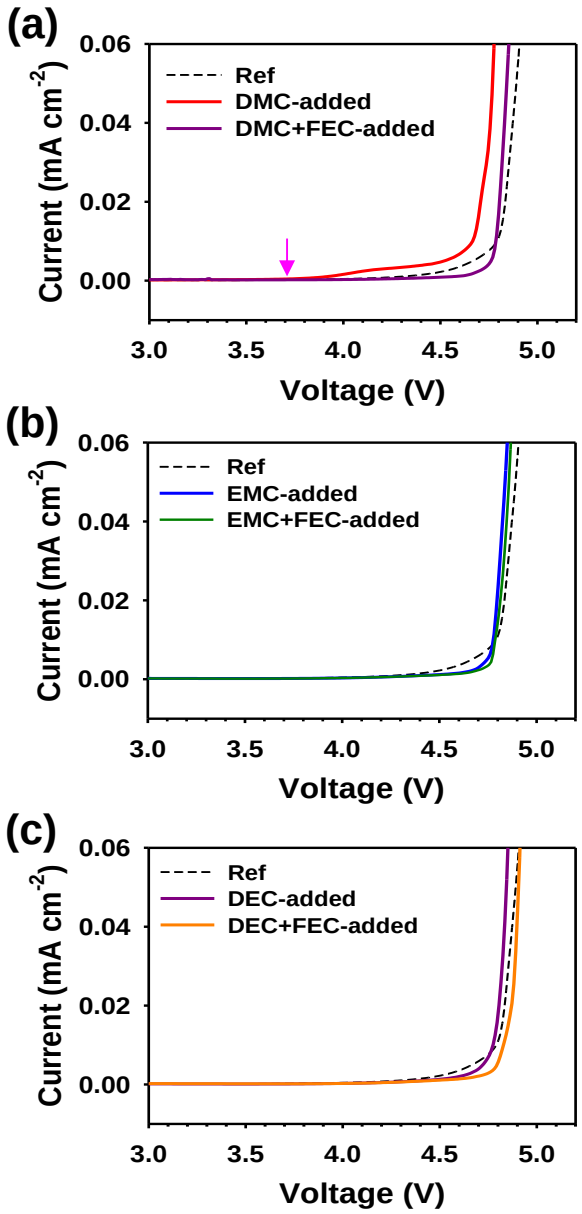

Fig. 2.3 Anodic limits of (a) DMC-added electrolytes with or without FEC, (b) EMC-added electrolytes with or without FEC, and (c) DEC-added electrolytes with or without FEC. Black dashed line represents the Ref electrolyte.

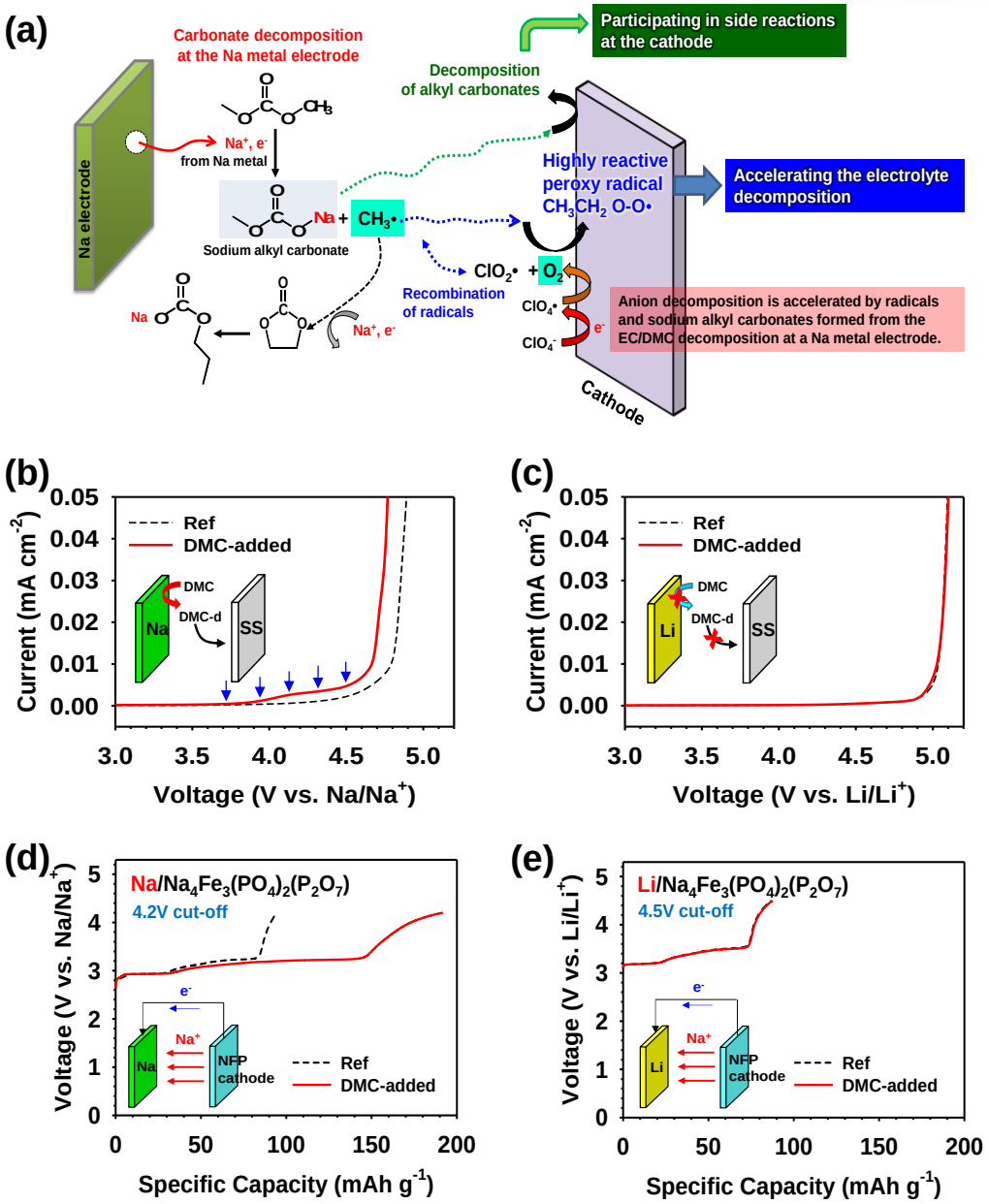

Fig. 2.4 (a) Schematic illustration of reduced anodic stability of electrolytes due to the decomposition of the linear carbonate DMC at the Na metal electrode. Comparison of anodic limits of DMC-added and Ref electrolytes in (b) Na/SS cell and (c) Li/SS cell. Voltage profiles of (d) Na/$Na_4Fe_3(PO_4)_2(P_2O_7)$ (NFP) cell and (e) Li/$Na_4Fe_3(PO_4)_2(P_2O_7)$ cell in the initial charge process at a current rate of C/20. DMC-d represents the by-products formed by the DMC decomposition at the Na metal electrode.

To investigate the reactivity of the DMC-added, EMC-added, and DEC-added electrolytes toward the Na metal electrode without any applied potentials, the chemical structures of the carbonate solvents in the electrolyte solution in contact with the Na metal electrode at room temperature for 10 days were examined by ^{13}C nuclear magnetic resonance (NMR) (Fig. 2.5). Clearly, new peaks appeared at 57.0 ppm and 68.1 ppm in the ^{13}C NMR spectra of the DMC-added electrolyte after contact with the Na metal electrode (Fig. 2.5a). The peak at 57.0 ppm can be thought to be characteristic of the methyl (-CH_3) group of the sodium methyl carbonate formed by the DMC decomposition at the Na metal, as depicted in Fig. 2.5c. The peak at 68.1 ppm can be attributed to the sodium propyl carbonate generated by the reaction between EC and the CH_3· radical species that resulted from the DMC decomposition. We infer that unstable by-products such as radicals and sodium alkyl carbonates due to decomposition of the linear carbonates at the Na metal electrode may diffuse to the cathode and lead to significant electrolyte decomposition under high voltage conditions. To alleviate any undesirable reaction between DMC and the Na metal electrode, the reducible FEC additive, which is responsible for the formation of stable solid electrolyte interphase (SEI) on the anode surface of SIBs, was introduced into the DMC-containing electrolyte solution.[7, 12] Surprisingly, the addition of FEC to the DMC-containing electrolyte led to the disappearance of the peaks attributed to sodium methyl carbonate (by DMC decomposition) and sodium propyl carbonate (produced by the reaction between EC and CH_3· species resulting from the DMC decomposition); the overall mechanism is shown in Fig. 2.5c. This result provides persuasive evidence that the FEC additive makes a protective surface film on the Na metal electrode and that the resulting film hinders the unwanted reaction of DMC with the Na metal electrode, as illustrated in Fig. 2.5d. From the NMR results, it is rational to suppose that the protection of the Na metal surface by the FEC additive suppresses the generation of anodic currents of the DMC-containing electrolyte at high voltages (Fig. 2.3a). Significant differences are observed for voltage profiles of Na/SS cells showing Na deposition/stripping (Fig. 2.6). After the first cathodic direction scan (Na deposition on an SS electrode), Na stripping took place from the Na deposits on the SS electrode, while Na was deposited on the Na counter electrode. FEC-free electrolytes exhibited Coulombic efficiency of lower than 21%. On the other hand, high Coulombic efficiency of greater than 85% could be achieved for the FEC-added electrolytes during the initial Na deposition/stripping process. More importantly, the greatly improved Coulombic efficiency (ca. 90%) was obtained for the DEC-added electrolyte with the FEC additive. This is presumably because FEC forms a stable protective film on the Na metal electrode and effectively mitigates irreversible side reactions between the Na metal electrode and the electrolyte. Moreover, it is thought that FEC produces the FEC-derived SEI on the SS electrode and allows the reversible deposition/stripping of Na. Interestingly, the DMC-added (11.2%) and DMC + FEC-added (85.6%) electrolytes showed relatively low Coulombic efficiency during the initial Na deposition/stripping

process, compared to the Ref (20.7%) and FEC-added (89.6%) electrolytes. This result appears to be caused by high reactivity of DMC toward the Na metal electrode. The reactivity of the EMC-added electrolytes toward the Na metal electrode was also investigated by means of ^{13}C NMR (Fig. 2.7a and b). For the EMC-added electrolytes, six new peaks appeared after contact with the Na metal electrode for 10 days; these peaks were observed at 68.1 ppm, 67.8 ppm, 66.5 ppm, 66.0 ppm, 57.0 ppm, and 56.8 ppm. Two peaks at 66.5 ppm and 57.0 ppm can be attributed to two sodium alkyl carbonate species resulting from the decomposition of EMC molecules at the Na metal electrode, as shown in possible mechanisms given in Fig. 2.7c. These two sodium alkyl carbonate species undergo further reaction with $CH_3\cdot$ or ethyl radical ($CH_2CH_3\cdot$) resulting in EMC and DMC molecules which indicated at 66.0 ppm and 56.8 ppm. Additionally, two peaks at 68.1 ppm and 67.8 ppm corresponding to decomposition products of EC molecules formed by reaction between EC and $CH_3\cdot$ or $CH_2CH_3\cdot$. Importantly, the addition of FEC to the EMC-containing electrolyte effectively suppressed the EMC decomposition at the Na metal electrode and thereby there were no new peaks ascribed to the EMC decomposition products (Fig. 2.7b). The ^{13}C NMR spectra of the DEC-added electrolytes with and without FEC before and after contact with Na metal for 10 days at room temperature are shown in Fig. 2.8. Because the DEC solvent in EC/PC/DEC (5/3/2)/0.5 M $NaClO_4$ reacted with Na metal and decomposition products (radicals, sodium alkyl carbonates) were formed in the electrolyte solution, new peaks appeared at 67.8 ppm (2’ of the decomposed EC molecule) and 66.5 ppm (1’ of the decomposed DEC molecule). Importantly, the peaks attributed to the DEC decomposition products completely disappeared in the presence of FEC in the DEC-containing electrolyte.

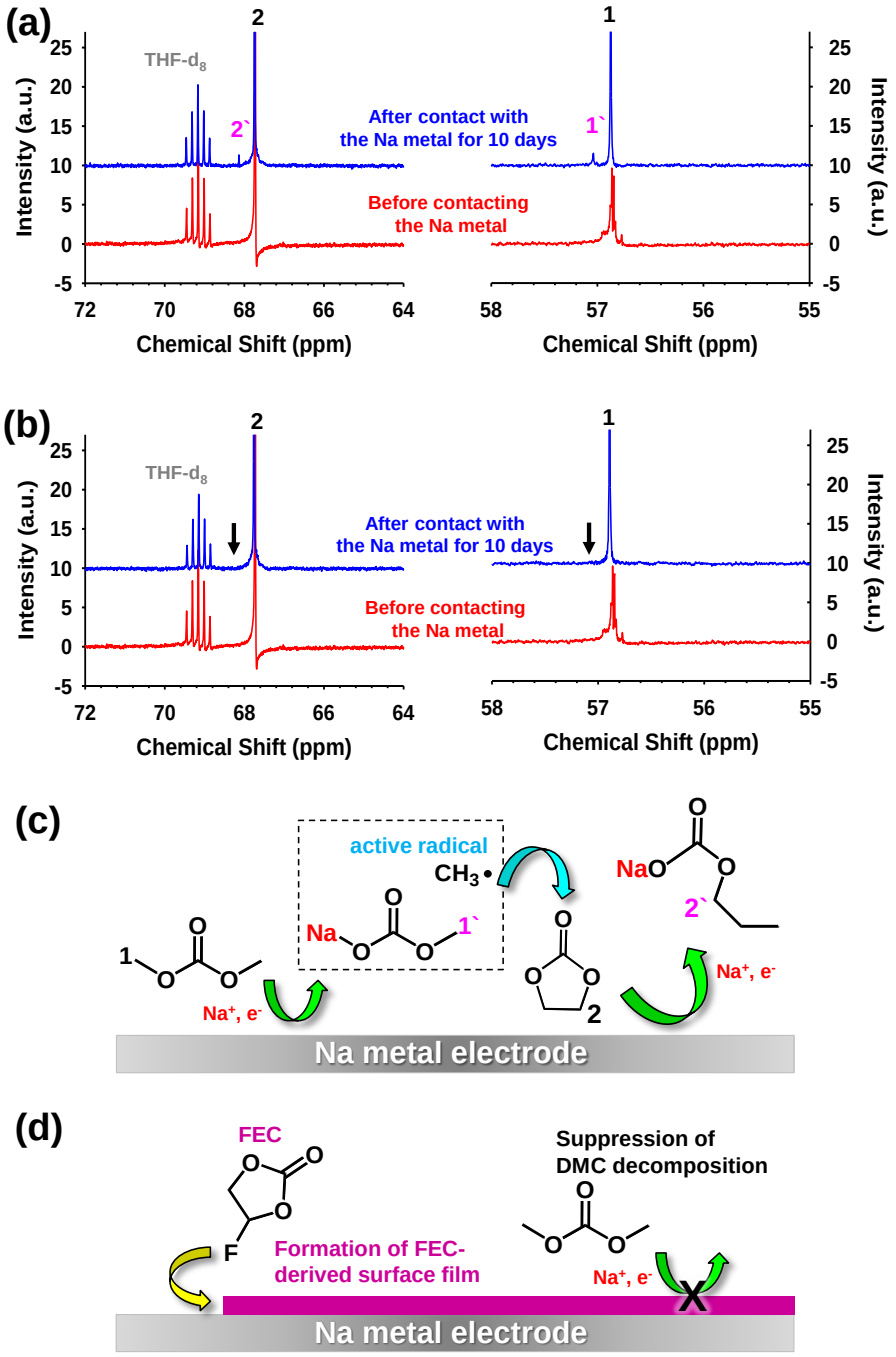

Fig. 2.5 ^{13}C NMR spectra of (a) DMC-added electrolyte, (b) DMC+FEC-added electrolyte before and after contact with Na metal for 10 days without applied potentials. Schematic of (c) the formation of decomposed products by the reaction between DMC and Na metal and (d) the suppression of the decomposition of DMC by addition of FEC, which can make a protective surface film on Na metal.

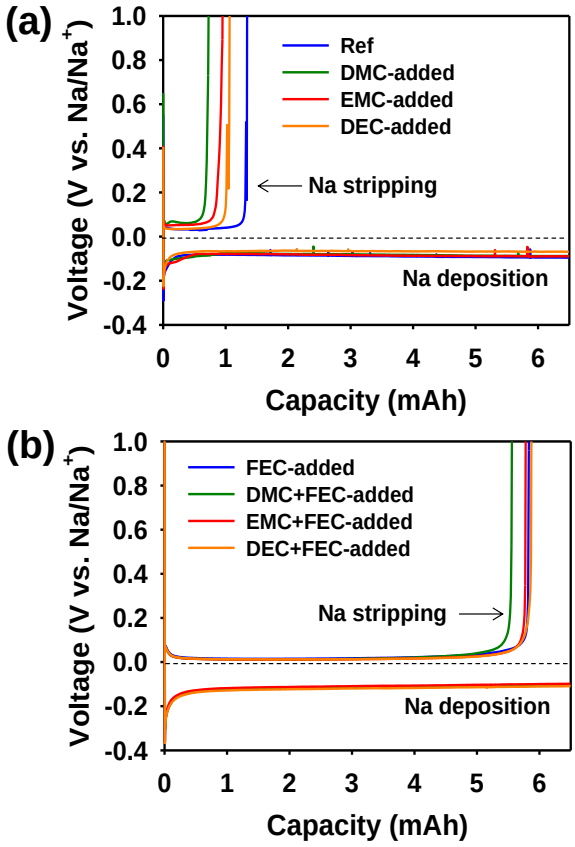

Fig. 2.6 Voltage profiles of Na/SS cells showing Na deposition on a SS electrode and Na stripping from the Na deposits on a SS electrode for a current rate of C/10. Utilized capacity from the Na metal electrode = 6.5 mAh.

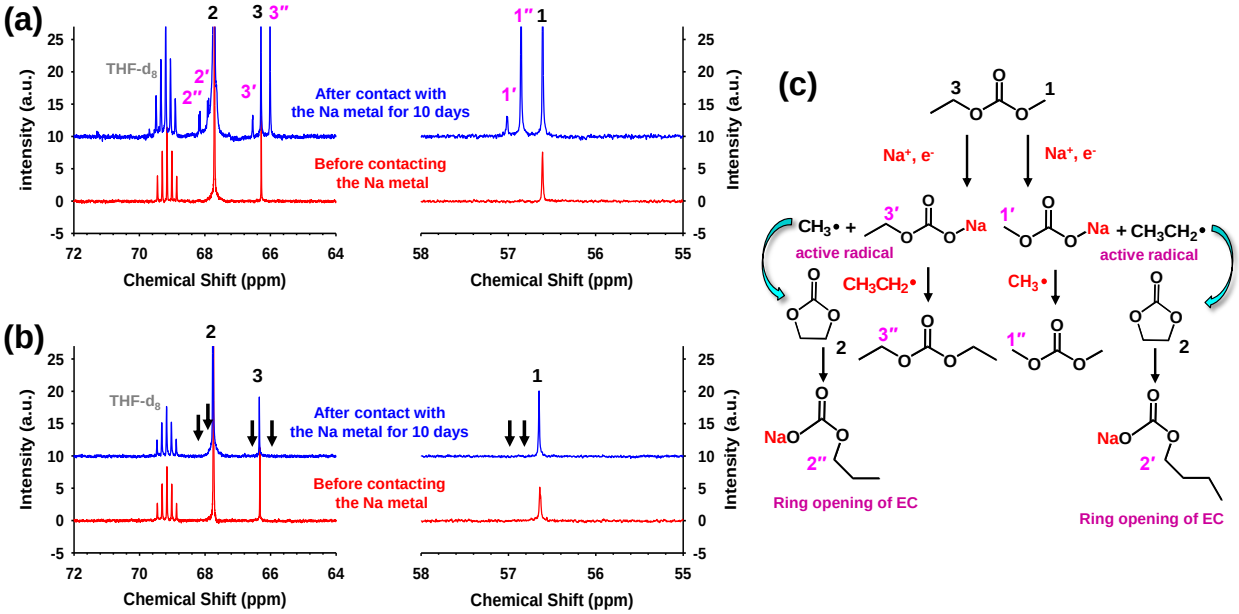

Fig. 2.7 ^{13}C NMR spectra of (a) EMC-added electrolyte, (b) EMC+FEC-added electrolyte before and after contacting the Na metal for 10 days. (c) Schematic of the formation of decomposed products by the reaction between EMC and Na metal.

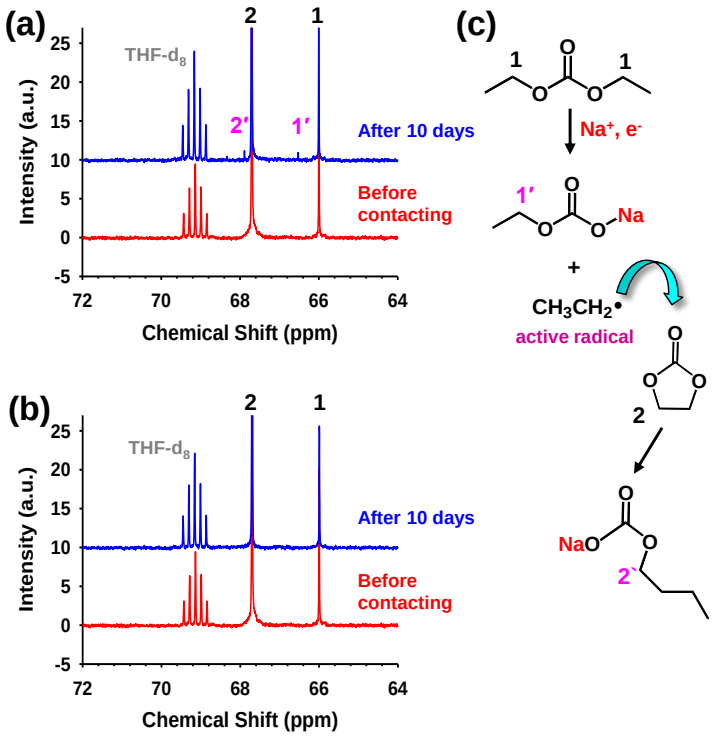

Fig. 2.8 ^{13}C NMR spectra of (a) DEC-added electrolyte, (b) DEC+FEC-added electrolyte before and after contacting the Na metal for 10 days. (c) Schematic of the formation of decomposed products by the reaction between DEC and Na metal.

Fig. 2.9 shows the charge and discharge profiles of the Na/$Na_4Fe_3(PO_4)_2(P_2O_7)$ half cells during precycling. The Ref electrolyte delivered a charge capacity of 94.4 mAh g^{-1} with two voltage plateaus at 2.9 V and 3.2 V. However, the DMC-added electrolyte exhibited an excessive charge capacity of 191.8 mAh g^{-1}, as can be seen in Fig. 2.9a. The increased length of the voltage plateaus at 3.2 V and 4.1 V might have originated from the electrochemical decomposition, at the cathode, of the decomposition products that were diffused away from the Na metal electrode. This significant overcharge behavior at 3.2 V and 4.1 V is consistent with the reduced anodic limit observed for the DMC-added electrolyte, as is shown in Fig. 2.3a. There was no overcharge behavior in the DMC added electrolyte with FEC protecting the Na metal electrode (Fig. 2.9d). This indicates that FEC builds up the FEC-derived SEI on the Na metal electrode and effectively prevents DMC decomposition at the Na metal electrode. Unlike the DMC-added electrolyte, the EMC-added and DEC-added electrolytes showed no overcharge behavior, as can be seen in Fig. 2.9b and c. This is because EMC and DEC linear carbonates did not undergo any considerable decomposition at the Na metal electrode, and thus there were no electrochemical decomposition reactions of electrolytes at the cathode causing undesirable overcharging during precycling. Fig. 2.10 provides evidence that DMC, EMC, and DEC in electrolytes have different levels of reactivity toward the Na metal electrode in the half cells during precycling. Photographs of the Na metal electrodes and glass fiber filter (GFF) separators retrieved from the Na/$Na_4Fe_3(PO_4)_2(P_2O_7)$ half cells after precycling clearly show that no significant color change was observed in the Ref electrolyte without FEC. On the contrary, the Na metal electrodes and GFF separators that were precycled in the DMC-added electrolyte without FEC were covered by colored compounds (Fig. 2.10a). This result indicates that the DMC-added electrolyte without FEC undergoes significant decomposition at the Na metal electrode; the resulting decomposition products lead to electrolyte decomposition at the $Na_4Fe_3(PO_4)_2(P_2O_7)$ cathode during precycling. There was no significant color change of the Na metal electrodes and GFF separators precycled in the DMC + FEC-added electrolyte (Fig. 2.10b). It is thought that the explicit presence of FEC drastically inhibits the DMC decomposition at the Na metal electrode, which is consistent with the NMR results for the DMC + FEC-added electrolytes. Unlike the DMC-added electrolyte, the EMC-added and DEC-added electrolytes with and without FEC showed color changes of Na metal electrodes and GFF separators that were not severe (Fig. 2.10(a) and (b)), which shows that there was no overcharge behavior during precycling. This discrepancy among linear carbonate-containing electrolytes may be ascribed to the different reactivity levels of the linear carbonates toward Na metal. A comparison of the cycling stabilities and Coulombic efficiencies of $Na_4Fe_3(PO_4)_2(P_2O_7)$ cathodes with linear carbonate containing electrolytes at a rate of C/2 (corresponding to 50 mA g^{-1}) is shown in Fig. 2.11. The Ref electrolyte exhibited a discharge capacity of 90.6 mAh g^{-1} and a Coulombic efficiency of 99.2% at 100th cycle

(Fig. 2.11a and b). However, the $Na_4Fe_3(PO_4)_2(P_2O_7)$ cathode cycled in the DMC-added electrolyte exhibited significant overcharge behavior and very low Coulombic efficiency of 91–98% during 40 cycles, as shown in Fig. 2.11a and b. The discharge capacity of the $Na_4Fe_3(PO_4)_2(P_2O_7)$ cathode with the DMC + FEC-added electrolyte, slightly decreased to 87.7 mAh g^{-1}, leading to a high Coulombic efficiency of 99.3%. Once the Na metal electrode is covered with the FEC-derived surface film, the DMC solvent hardly reacts with the Na metal and there are no detrimental effects of by-products of DMC decomposition on the cycling performance of the cathodes. Although the DMC + FEC-added electrolyte shows a relatively high ionic conductivity in Fig. 2.1a, it is thought that the DMC + FEC-added electrolyte builds up a resistive surface film on the $Na_4Fe_3(PO_4)_2(P_2O_7)$ cathode; in contrast to other electrolytes, DMC + FEC-added electrolyte impedes the movement of charge carriers at the cathode-electrolyte interface, and as a result the capacity utilization of the cathodes is limited (Fig. 2.11a).

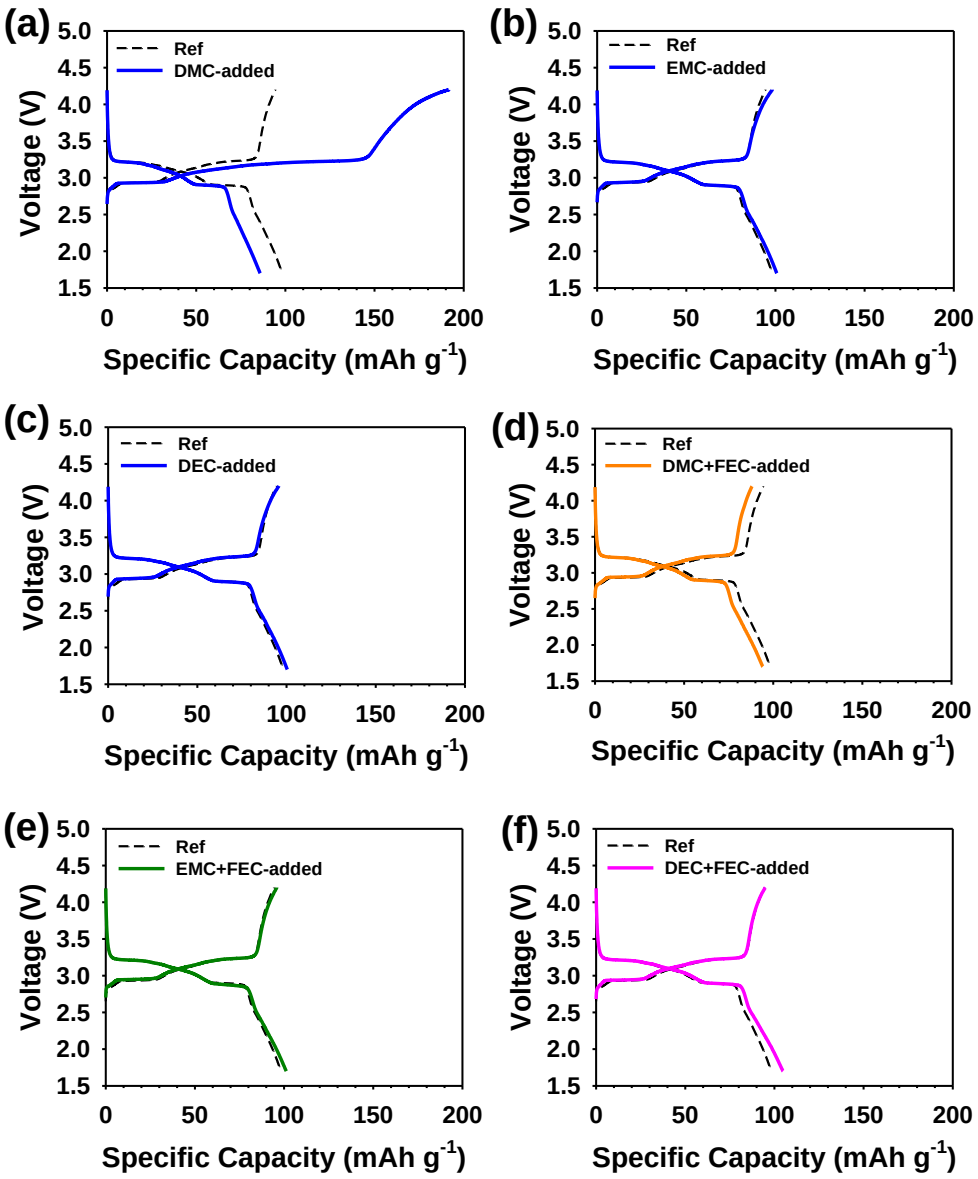

Fig. 2.9 (a) DMC-added, (b) EMC-added, (c) DEC-added, (d) DMC+FEC-added, (e) EMC+FEC-added, and (f) DEC+FEC-added electrolytes during precycling at a current rate of C/20 and 30 °C. For comparison, voltage profiles of the $Na_4Fe_3(PO_4)_2(P_2O_7)$ cathode in the Ref electrolyte are represented by black dashed lines.

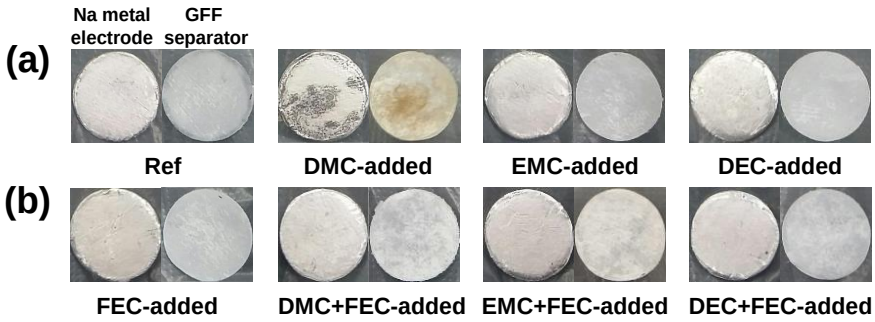

Fig. 2.10 Photographs of Na metal electrodes and GFF separators (a) without FEC and (b) with FEC after precycling at a rate of C/20.

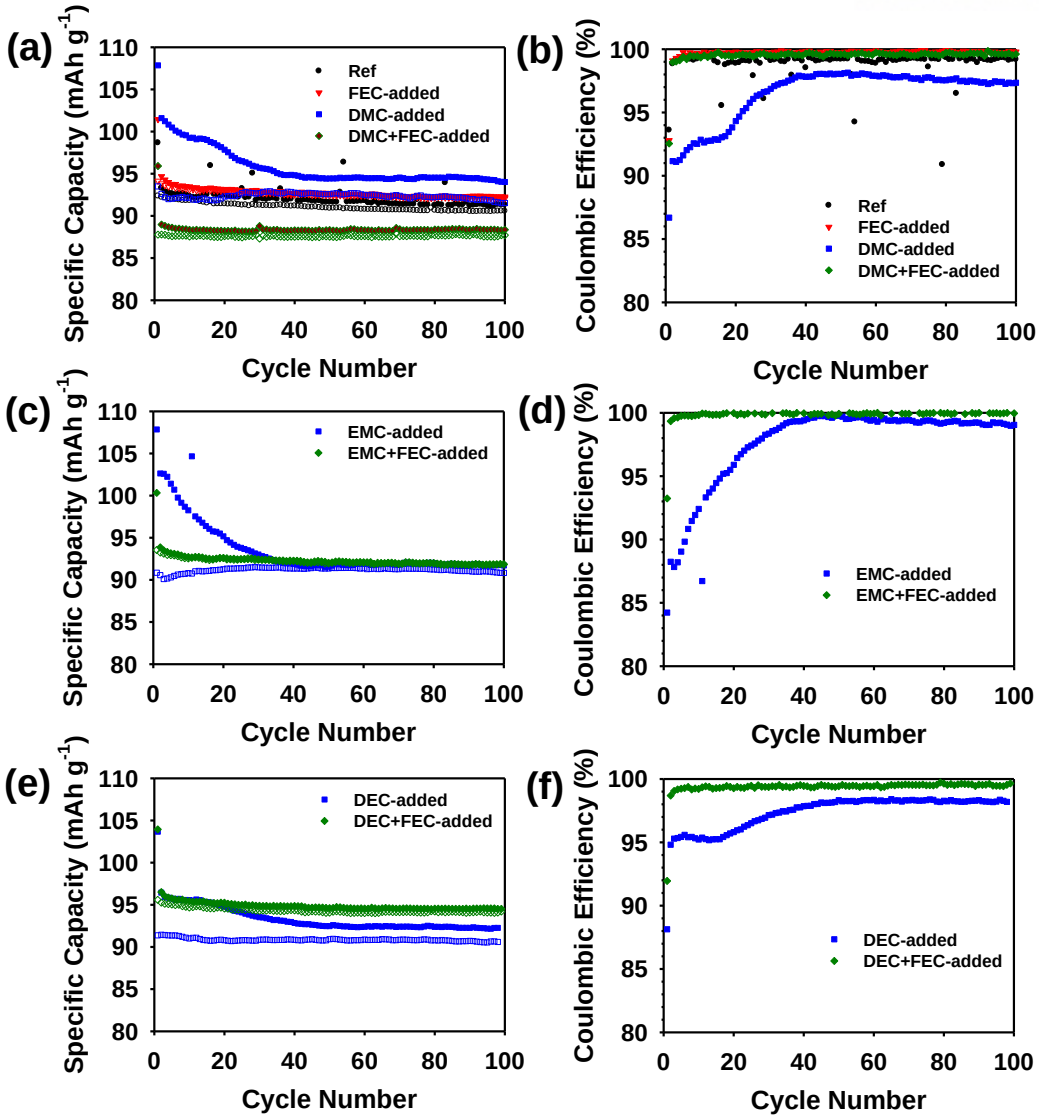

Fig. 2.11 Cycling performance and Coulombic efficiency of $Na_4Fe_3(PO_4)_2(P_2O_7)$ cathodes with (a,b) DMC-added electrolyte or DMC+FEC-added electrolyte, (c,d) EMC-added electrolyte or EMC+FEC-added electrolyte, and (e,f) DEC-added electrolyte or DEC+FEC-added electrolyte at a current rate of C/2 and 30 °C. Filled and empty symbols represent charge and discharge capacities, respectively.

To understand the reason why a reduced discharge capacity was obtained in the DMC + FEC-added electrolyte, ex situ X-ray photoelectron spectroscopy (XPS) measurements for cathodes precycled in all of the electrolytes with FEC were performed. The F 1s XPS spectra for the surface chemistry of the cathodes precycled in Ref, DMC-added, EMC-added, and DEC-added electrolytes with FEC are presented in Fig. 2.12a-d. The peak assigned to NaF at 684.5 eV, produced by the FEC decomposition, was clearly observed in the F 1s spectra of all the cathodes precycled in the electrolytes with FEC. This result demonstrates that charged up to 4.2 V (*vs.* Na/Na^+). A noticeable feature is that the $Na_4Fe_3(PO_4)_2(P_2O_7)$ cathodes precycled in Ref and DMC-added electrolytes with FEC exhibit relatively strong peak attributed to NaF (fraction: 35.9%), compared to EMC-added and DEC-added electrolytes with FEC (Fig. 2.12a-d). Moreover, the peak intensity assigned to the PO_4^{3-} and $P_2O_7^{4-}$ anions of cathode precycled in the DMC + FEC-added electrolyte was apparently reduced unlike the Ref electrolyte with FEC, which showed comparable peak intensity with that of the pristine (non-cycled) cathode (Fig. 2.13). This is probably because a thick surface film formed from the decomposition of DMC + FEC-added electrolyte blocks the P signal from the cathode. Since NaF and a thick surface film can act as a resistive layer, impeding the migration of Na ions into the cathode, it is thought that the capacity utilization of the $Na_4Fe_3(PO_4)_2(P_2O_7)$ cathode decreases in the DMC + FEC-added electrolyte at a given C rate. The EMC-added electrolyte showed similar overcharge behavior with the DMC-added electrolyte, while the DEC-added electrolyte exhibited observably reduced overcharge at the beginning of cycling in the absence of FEC (Fig. 2.11c and e). Surprisingly, the use of FEC in the EMC-added and DEC-added electrolytes could lead to the excellent cycling stability of the $Na_4Fe_3(PO_4)_2(P_2O_7)$ cathode and a very high Coulombic efficiency of ca. 99.5%, which is vital for practical applications, during 100 cycles at 50 mA g^{-1}. More importantly, the cathode cycled in the DEC + FEC-added electrolyte delivered the highest discharge capacity of 94.2 mAh g^{-1} (Fig. 2.11e). This superior reversible capacity may be thanks to relatively low fraction of NaF (14.7%), which can act as physical barrier for the conduction of Na^+ ions, as shown in Fig. 2.12d. This result suggests that the FEC additive makes a desirable interfacial architecture on the Na metal electrode in the $Na/Na_4Fe_3(PO_4)_2(P_2O_7)$ half cells and preserves the reversibility of the electrochemical reactions of the cathodes without significant capacity loss. Fig. 2.14 provides photographs of the Na metal electrodes and GFF separators retrieved from the $Na/Na_4Fe_3(PO_4)_2(P_2O_7)$ half cells after 100 cycles. The Na metal electrodes and GFF separators cycled in the Ref electrolyte with and without FEC showed no significant color changes. In contrast to the other electrolytes, a noticeable feature is the significant color change of the Na metal electrode and GFF separator cycled in the DMC-added electrolyte without FEC. This is clear evidence that severe electrochemical decomposition of the DMC-added electrolyte without FEC occurs during cycling. This severe decomposition was effectively inhibited by the addition of FEC, as shown in Fig. 2.14b. From

this result, it can be thought that the FEC additive builds up a protective surface film preventing unwanted electrolyte decomposition at the Na metal electrode and $Na_4Fe_3(PO_4)_2(P_2O_7)$ cathode. EMC-added and DEC-added electrolytes without FEC, which exhibited little color change at precycling (Fig. 2.10a), showed severe color change after 100 cycles (Fig. 2.14a). This result is in agreement with the NMR results shown in Figs. 2.7 and 2.8, which show that EMC and DEC solvents in FEC-free electrolytes are also reactive toward the Na metal electrode. The considerable color change of the Na metal electrodes and GFF separators cycled in EMC-added and DEC-added electrolytes could be avoided by using FEC additive, as shown in Fig. 2.14b. In addition, color change of the Na metal electrode and GFF separator observed for the DEC + FEC-added electrolyte after 100 cycles was less significant and was similar to that of the Ref containing FEC additive (Fig. 2.14b). Among the linear carbonates (DMC, EMC and DEC), DEC is believed to be the most appropriate cosolvent of the FEC-added electrolyte for the formation of a desirable interfacial structure to allow the reversible sodiation/desodiation of $Na_4Fe_3(PO_4)_2(P_2O_7)$ cathodes during cycling. On the basis of a comparison of cycling performance of $Na/Na_4Fe_3(PO_4)_2(P_2O_7)$ half cells with a PE or a GFF separator (Fig. 2.15), it is obvious that the DEC + FEC-added electrolyte is a promising electrolyte system that exhibits good wettability toward a PE separator and leads to good cycling performance of the cathode. $Na_4Fe_3(PO_4)_2(P_2O_7)$ cathodes with a PE separator delivered a comparable discharge capacity with that obtained in the cathode with a GFF separator and the discharge capacity of the cathode remained nearly constant during 50 cycles (Fig. 2.15a). It was also found that the $Na_4Fe_3(PO_4)_2(P_2O_7)$ cathode with a PE separator had a high Coulombic efficiency of greater than 99.5% within 20 cycles at 30 ^oC (Fig. 2.15b). To further confirm the positive impact of the DEC + FEC-added electrolyte on long-term cycling performance of the cathode with a PE separator, galvanostatic cycling of $Na/Na_4Fe_3(PO_4)_2(P_2O_7)$ cells was performed at a current rate of C/2 and 30 ^oC (Fig. 2.12e and f). Clearly, an excellent cycling stability of the cell with a PE separator was achieved in the DEC + FEC-added electrolyte, delivering a capacity of 90.5 mAh g^{-1} without noticeable capacity loss over 300 cycles (Fig. 2.12e). In addition, $Na/Na_4Fe_3(PO_4)_2(P_2O_7)$ cells with a PE separator exhibited a very high Coulombic efficiency of greater than 99.5% (Fig. 2.12f).

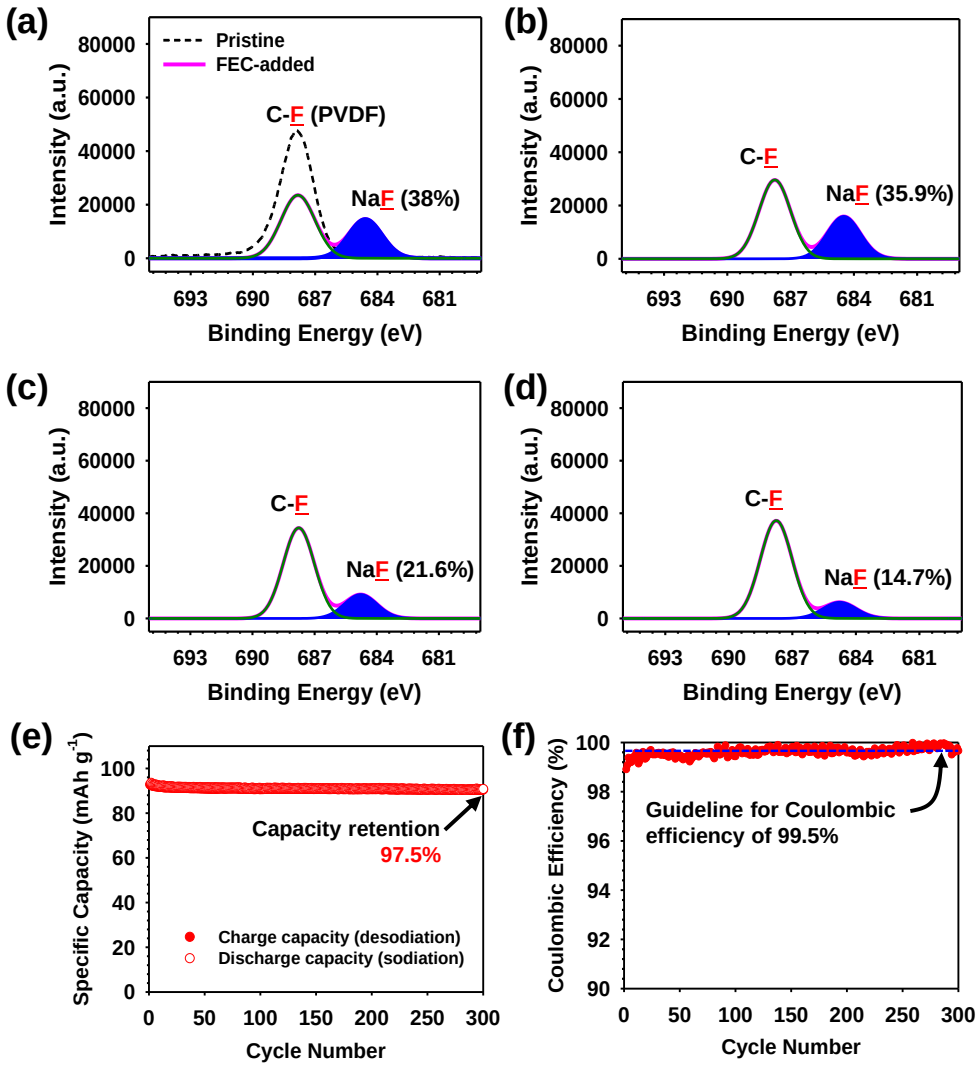

Fig. 2.12 F 1s XPS spectra of the $Na_4Fe_3(PO_4)_2(P_2O_7)$ cathodes precycled in (a) Ref electrolyte with FEC (FEC-added electrolyte), (b) DMC+FEC-added electrolyte, (c) EMC+FEC-added electrolyte, and (d) DEC+FEC-added electrolyte. Black dashed line represents the pristine (non-cycled) cathode. (e) Cycling performance and (f) Coulombic efficiency of $Na/Na_4Fe_3(PO_4)_2(P_2O_7)$ cells cycled in DEC+FEC-added electrolyte with a PE separator during 300 cycles at a current rate of C/2 and 30 °C.

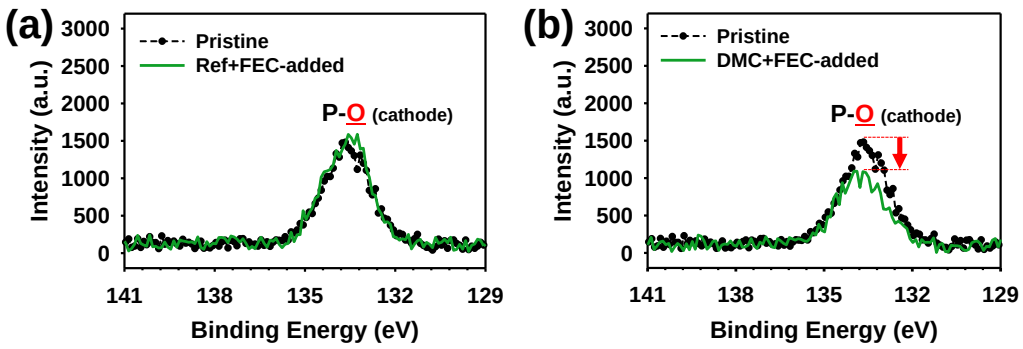

Fig. 2.13 P 2p XPS spectra of the $Na_4Fe_3(PO_4)_2(P_2O_7)$ cathodes precycled in (a) Ref electrolyte with FEC, (b) DMC+FEC-added electrolyte. Black dashed line represents the pristine (non-cycled) cathode.

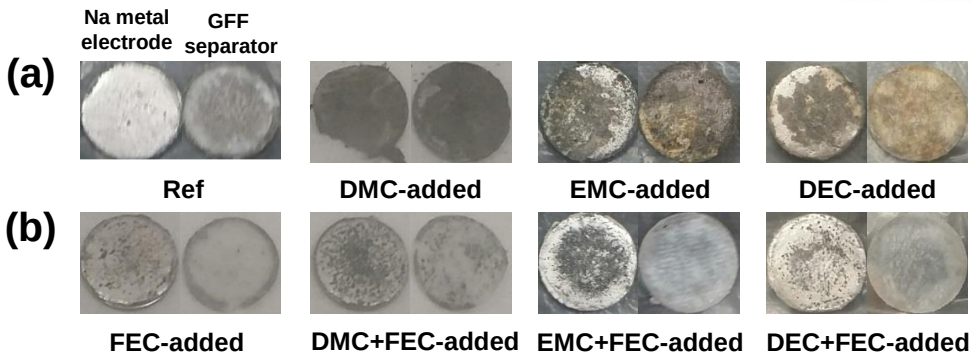

Fig. 2.14 Photographs of Na metal electrodes and GFF separators cycled in electrolytes (a) without FEC, (b) with FEC after 100 cycles at a rate of C/2.

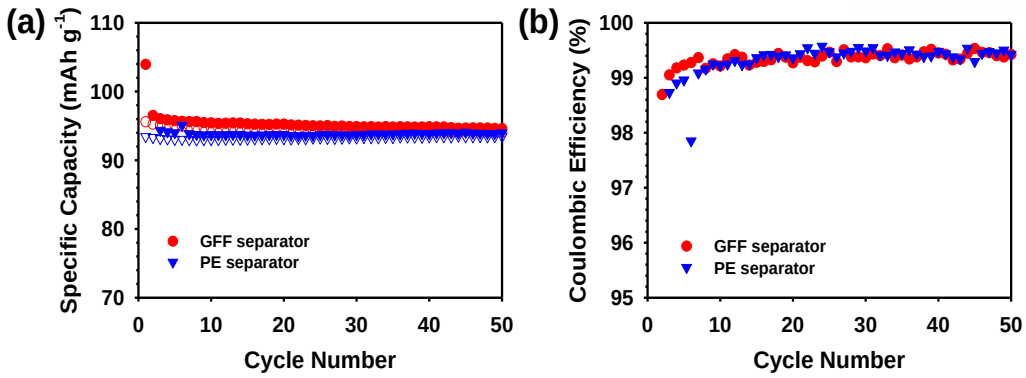

Fig. 2.15 (a) Cycling performance (filled symbols for charge capacity and empty symbols for discharge capacity) and (b) Coulombic efficiency of $Na_4Fe_3(PO_4)_2(P_2O_7)$/Na half cells with DEC+FEC-added electrolytes during 50 cycles at a rate of C/2. GFF (red) or PE (blue) was used as a separator.

2.4 Conclusion

We have demonstrated that linear carbonate-containing electrolytes with good wettability toward a conventional polyethylene separator undergo severe decomposition at Na metal electrodes and $Na_4Fe_3(PO_4)_2(P_2O_7)$ cathodes charged up to a high potential of 4.2 V (*vs.* Na/Na^+). ^{13}C NMR studies of electrolytes in contact with Na metal, and cycling tests of cathodes, confirmed that linear carbonate-containing electrolytes are not stable against highly reactive Na metal electrodes; the resulting decomposition products lead to cycling degradation of cathodes charged up to a high potential of 4.2 V. Furthermore, our investigation revealed that the FEC additive forms a protective surface film on the Na metal electrode and the cathode, and prevents undesirable decomposition of linear carbonates. Ex situ XPS analyses for the cycled cathodes manifested that the FEC additive forms an NaF resistive layer on the cathode surface and discernible reduction in the formation of NaF by the FEC decomposition is observed in the DEC + FEC-added electrolyte leading to the excellent cycling performance of cathodes. This finding may open up an effective means to develop optimized electrolyte systems for high-performance sodium-ion batteries.

III. Fluoroethylene carbonate-based electrolyte with 1 M sodium bis(fluorosulfonyl)imide enables high-performance sodium metal electrodes

3.1 Introduction

Since most Na deposition occurs at the interface between the anode (or the current collector) and the electrolyte, the discovery of a stable electrolyte is essential for utilizing Na metal anodes in practical applications of high-energy density Na-air and Na-S batteries.[41] Generally, carbonate-based electrolytes at conventional dilute concentrations inevitably lead to the formation of vulnerable interfacial layers from the accumulation of byproducts via decomposition of the electrolyte due to the strong reduction ability of Na metal electrodes. This undesirable interfacial layer gives the Na metal electrodes a limited cycle life, impedes dense Na deposition, and triggers the generation of dendritic Na metal, which does not ensure battery safety.[42] Simple dilute liquid electrolytes based on sodium hexafluorophosphate ($NaPF_6$) in DME were reported to prevent the dendritic growth of Na metal by the formation of a surface film composed of sodium oxide (Na_2O) and sodium fluoride (NaF).[43] This result offers the significant insight that the electrochemical properties of Na metal are closely associated with the interfacial characteristics. However, precycling during 10 cycles at a low current density of 50 μA cm^{-2} was performed to remove any surface contamination and develop NaF-based protective layer. Uncoordinated DME, which has a relatively strong Lewis basicity (high highest occupied molecular orbital (HOMO) energy level) in dilute electrolytes, is prone to undergo severe oxidative decomposition via donation of the oxygen lone pair electrons at voltages beyond approximately 4.0 V *vs.* Na/Na^+.[44] Therefore, control of the electrode-electrolyte interface and the development of electrolyte solvents with a high upper voltage limit are critical to achieve good Na battery performance. Previously, we found that the addition of 5 wt.% fluoroethylene carbonate (FEC) in 0.5 M sodium perchlorate ($NaClO_4$)-ethylene carbonate (EC)/propylene carbonate (PC)/diethyl carbonate (DEC) leads to the creation of an FEC-based interfacial layer that can prevent the undesirable corrosion of a Na metal anode coupled with a $Na_4Fe_3(PO_4)_2(P_2O_7)$ cathode.[45] Very recently, it was demonstrated that FEC builds up a stable surface film on the surface of the Li metal electrodes and leads to uniform Li metal deposition in Li metal batteries.[46,21] However, fundamental understanding of the reductive decomposition of FEC molecules at the Na metal anode was not fully developed.

In this work, we demonstrate a new combination of electrolytes based on solvent and salt possessing fluorine atom. FEC with 1 M NaFSI dramatically enhances the reversibility of Na plating and stripping reactions in Na/Cu cells, realizes dense Na deposition, and leads to improved cycling stability at high current densities, which would otherwise be impossible for electrolytes that use FEC as an additive.

The most postulated decomposition mechanisms of an FEC compound that adequately modifies the interfacial nature of Na deposits in 1 M sodium bis(fluorosulfonyl)imide (NaFSI)-based electrolytes are proposed through ex situ X-ray photoelectron spectroscopy (XPS) studies. Through direct observation using in situ techniques, such as differential electrochemical mass spectrometry (DEMS) and optical microscopy (OM) studies, during the electrochemical reaction, we suggest, for the first time, the underlying mechanisms of the FEC-NaFSI electrolyte that effectively prevents the formation of Na dendrites, which threaten Na metal battery safety and enable fast Na plating and stripping at high current densities.

3.2 Experimental method

Preparation of electrolytes

Electrolytes were prepared by dissolving 1 M Na salt (sodium perchlorate ($NaClO_4$, 98.0%, Aldrich), sodium hexafluorophosphate ($NaPF_6$, 99.0%, Alfa Aesar), sodium bis(trifluoromethanesulfonyl)imide (NaTFSI, 99.5%, Solvionic) or sodium bis(fluorosulfonyl) imide (NaFSI, 99.7%, Solvionic) in a solvent mixture of ethylene carbonate (EC)/propylene carbonate (PC) prepared in a 1/1 volume ratio or a pure fluoroethylene carbonate (FEC, Enchem) solvent. All solvents (Soulbrain Co., Ltd.) were used as received. 1, 5, or 10 wt.% FEC was added to EC/PC (1/1) with 1 M Na salt.

Electrochemical test

2032 coin-type cells with a Na metal electrode, a copper (Cu) substrate (1.77 cm^2) and a glass fiber filter (GFF, Whatman GF/C) separator were assembled in an argon-filled glovebox, which contained less than 1 ppm of both oxygen and moisture, to evaluate the Coulombic efficiency of Na plating and stripping. A three-electrode cell with Na metal as the counter and reference electrodes, the Cu substrate as a working electrode, and a GFF separator was assembled in an argon-filled glove box containing less than 1 ppm of both oxygen and moisture to monitor the potential variation of the Na metal counter electrode and Cu working electrode versus the Na metal reference electrode. Galvanostatic precycling of the Na/Cu cells was performed with a current density of 0.056 mA cm^{-2}. During the initial cathodic scan, electrodeposition of Na metal occurred on the Cu substrate up to a deposited areal capacity of 0.56 mAh cm^{-2} (0.7% capacity utilization of the Na metal electrode). Electrochemical stripping of the Na deposits on Cu substrate occurred during the initial anodic scan until the potential reached 1.0 V versus Na/Na^+. Cycling performances were evaluated at a current density of 0.056 mA cm^{-2} or 0.28 mA cm^{-2}. The rate capability of the Na/Cu cells was evaluated at various current densities of 0.056, 0.169, 0.282, 0.56, 1.12, 1.69 and 2.82 mA cm^{-2}. The reversibility of Na plating and stripping reactions were evaluated at the same current density. The areal capacity utilized from the counter Na metal electrode was 0.56 mAh cm^{-2}.

Characterization

The ionic conductivity of the electrolytes was measured using an Oakton CON 11 standard conductivity meter at 25 °C. The viscosity of the electrolytes was measured using a Brookfield viscometer (LVDV-11+P) at 25 °C. The morphology of Na deposits on a Cu substrate was observed by field-emission scanning electron microscopy (FE-SEM; JSM-6700F, JEOL) in a high-vacuum environment. The

electrodeposition of Na metal was performed using a galvanostatic method under a current density of 0.282 mA cm^{-2} and ceased after a total capacity of 2.82 mAh cm^{-2} was reached, as detected by a computer-controlled battery measurement system (WonATech SBCS 3000). After electroplating Na metal on the Cu substrate, the cells were carefully disassembled in a glove box and the Na metal deposits were rinsed with a PC solvent to remove excess surface-bound electrolyte. The retrieved sample was sealed in pouches for transport to the SEM to avoid any contamination of the sample. The resulting Na metal deposits on the Cu substrate were dried at room temperature for analysis. Ex situ X-ray photoelectron spectroscopy (XPS, Thermo Scientific K-Alpha System) measurements were carried out using Al-Kα (hv= 1486.6 eV) radiation under ultrahigh vacuum. XPS spectra were collected using a 0.10 eV step and an 80 eV pass energy. Na metal plated on a Cu substrate retrieved from cells was put on a XPS holder in a glove box and the prepared samples were sealed with an aluminum pouch film under a vacuum. The samples were rapidly transferred from an aluminum pouch bag into a vacuum chamber of XPS instrument to minimize any possible contamination. In situ observations of Na electrodeposition on Cu substrate were performed in a beaker-type Na/Cu cell and snapshots of Na deposits were obtained by recording at various states of Na plating (1, 2, and 30 min, and 2, 5, 7, 10 h) during the initial Na plating process at 0.282 mA cm^{-2} (corresponding to a capacity of 2.82 mAh cm^{-2}). In situ optical microscopy (OM) (Olympus, BX53M) was used to monitor the electrodeposition of Na metal on Cu substrates in a Na/Cu electrochemical test cell (EC-CELL, ECC-Opto-SBS). The Na counter and reference electrodes, Cu substrate (0.54 cm^2), and GFF separator were assembled in an argon-filled glovebox with less than 1 ppm of oxygen and moisture. The electrodeposition of Na metal was performed by a galvanostatic method at 0.463 mA cm^{-2} up to a deposited areal capacity of 1.389 mAh cm^{-2} using a computer-controlled battery measurement system (BioLogic SP-300). In situ differential electrochemical mass spectrometry (DEMS) analysis was used to monitor gas evolution in the Na/Cu cells during the initial Na plating at a current density of 0.282 mA cm^{-2}. A Cu mesh substrate (1.77 cm^2) and a GFF separator were assembled in an argon-filled glove box that contained less than 1 ppm of both oxygen and moisture. The gas evolution in the cells was probed in 10 minutes intervals.

3.3 Results and discussion

According to a schematic highest occupied molecular orbital (HOMO)-lowest unoccupied molecular orbital (LUMO) energy level diagram (Fig. 3.1), electrons accumulated in the vicinity of the sodium (Na) metal anode during the initial Na plating process are consumed by fluoroethylene carbonate (FEC), which has a relatively low LUMO energy level, reflecting high electron affinity. The interlayer formed by the reductive decomposition of FEC molecules blocks electron transfer to the electrolyte and alleviates further decomposition reactions. Moreover, the presence of F atoms, which have electron-withdrawing character, reduces the HOMO energy level of FEC, and therefore, FEC-based electrolyte is more electrochemically stable at the cathode during cycling. Conventional carbonates tend to form unstable and resistive interlayers, indicating a lack of ability to preserve the electrochemical reversibility of Na metal anodes with high reducing power.[45, 47] In dilute electrolytes, 1,2-dimethoxyethane (DME), which is considered a suitable electrolyte solvent for metal anodes, readily undergoes severe oxidation at 4V-class cathodes due to its high HOMO energy level.

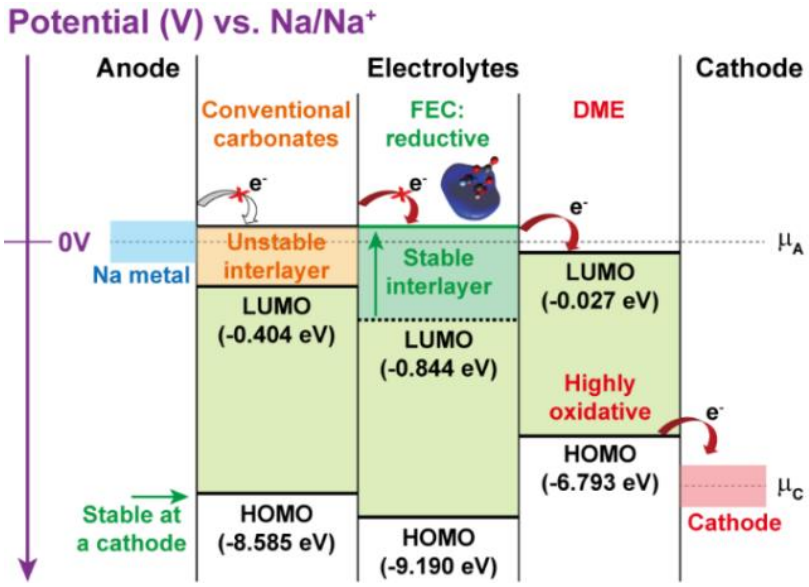

Fig. 3.1 HOMO-LUMO energy level diagram of conventional carbonates, FEC, and DME. μ_A and μ_C indicate the Fermi level of the Na metal anode and sodium-containing cathode, respectively. For the ab initio calculation, molecular optimization was carried out using density functional theory (DFT) at the B3LYP/6-311+G level of theory.

FEC is adopted to control Na plating on a copper (Cu) substrate because FEC readily accepts electrons from the negatively charged substrate. As the content of FEC, which forms a protective interlayer during the electrochemical Na plating, was increased, the Na/Cu cell showed a greatly enhanced Coulombic efficiency (CE) and stable cycling performance (Fig. 3.2a and Fig. 3.3b). The initial Coulombic efficiency (ICE) is a significant index, indicative of the initial reversibility during the electrochemical reactions, which helps to understand the mechanism of the initial reaction between Na metal and the electrolyte. The cell using 1 M NaFSI-FEC affords remarkable improvement of the ICE to 88.3%, while that using 1 M NaFSI-ethylene carbonate/propylene carbonate (EC/PC) exhibits the ICE of 29.9% (Fig. 3.3a). Moreover, the FEC-based cell shows superior cycling performance than the EC/PC-based cell, with retaining a high CE of approximately 94% over 100 cycles (Fig. 3.2a) and an astonishing display of voltage stability without further increase in overpotential (Fig. 3.4). This result suggests that FEC builds up an electrochemically stable interlayer that can serve as a shield mitigating severe electrolyte decomposition, which consumes Na^+ and e^-, avoiding a continuous filming process. In addition, FEC molecules coordinate Na^+ ions in the electrolyte, leading to transfer solvated charge carriers properly for reversible Na plating and stripping reactions (Fig. 3.5). Insufficient amounts of 1, 5, and 10 wt.% FEC additive in 1 M NaFSI-EC/PC undergoes rapid capacity fading after a few cycles (Fig. 3.3b) because small amount of FEC does not allow full coverage of the Na metal surface during cycling. Thereby, the electrolyte components directly contacting Na metal possessing a high reduction power are prone to decompose via accepting electrons. This continued electrolyte decomposition leads to the loss of reversible capacity of cells, creates a thick interfacial layer that hampers charge transfer in Na plating and stripping, and eventually the cell failure occurs. We have also tested the different electrolytes to confirm the effect of 1 wt.% FEC (Fig. 3.3c and d). All the data show short-term cycling performance of Na/Cu cells, indicating that the 1 wt.% FEC is rapidly consumed during repeated plating/stripping. Although one of the promising approaches is using an electrolyte additive to in situ create an artificial protective layer on anodes, highly reactive Na metal anodes require the use of sufficient functional compound maintaining full coverage of the Na metal. Thus, we suggest that the use of FEC as a main solvent enables the formation of a sustainable interfacial layer on the Na metal during prolonged cycling and can even mend a broken layer. The electrolyte design using FEC also affords remarkable rate capability, whereas other electrolyte systems exhibit undesirable rate capability. The cycling performance of the Na/Cu cell was investigated at high current densities to confirm high Na^+ ion transport in the 1 M NaFSI-FEC (Fig. 3.2b). Evaluation of the reversibility of Na plating and stripping at high areal capacities confirmed the unique property of 1 M NaFSI-FEC stabilizing Na metal (Fig. 3.6). Unlike the case of 1 M NaFSI-FEC, the use of 1 wt.% FEC as an additive caused drastic capacity fading at 0.056 mA cm^{-2}. The FEC-free electrolyte (1 M NaFSI-EC/PC) led to incomplete Na stripping

from the Na metal plated on the Cu substrate, showing a low CE of 15.6% even at a low current density of 0.056 mA cm^{-2}. A slightly increased CE was achieved at 0.169 mA cm^{-2} but continuous decay in CE was observed at higher current densities. This finding suggests that FEC plays a role in tuning the interface structure to kinetically manipulate the Na^+ ion transport at the Na metal electrode, and that the FEC content is the main factor governing the cycling performance of Na/Cu cells at high current densities. Therefore, the ability of FEC modifying the chemical structure of Na metal surface is a key factor governing electrochemical performances of Na metal electrodes (Fig. 3.2c).

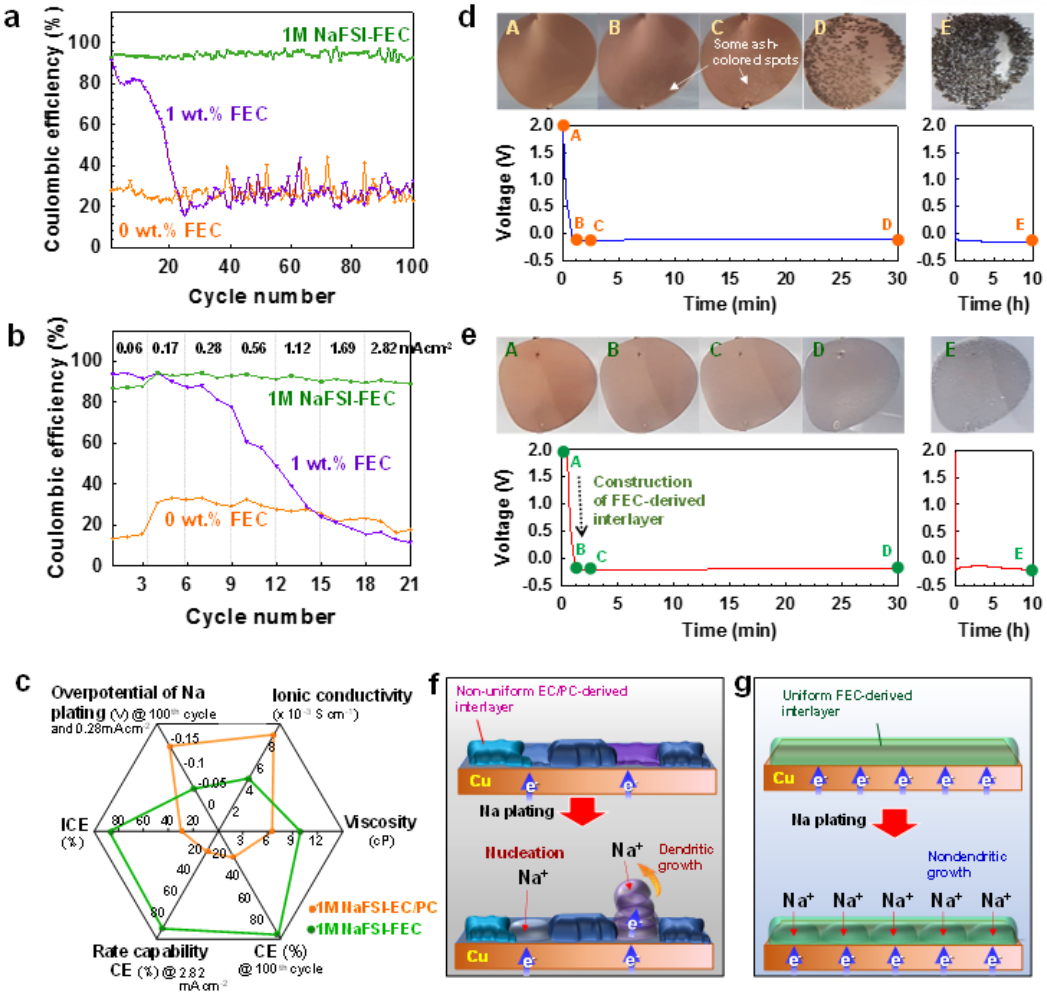

Fig. 3.2 (a) The Coulombic efficiency of Na/Cu coin-type cells in 1 M NaFSI-EC/PC (1/1), 1 M NaFSI-EC/PC (1/1) + 1 wt.% FEC and 1 M NaFSI-FEC at 0.28 mA cm^{-2}. (b) Rate capability of Na/Cu coin-type cells evaluated at the same current density for the Na plating and stripping process. (c) The electrochemical characteristics and physical properties of 1 M NaFSI in EC/PC (1/1) or FEC. Optical images showing in situ plated Na metal on a Cu substrate and voltage profiles during the initial Na plating process in (d) 1 M NaFSI-EC/PC (1/1) and (e) 1 M NaFSI-FEC at 0.28 mA cm^{-2} and 25 °C. Schematic drawing of Na deposition at the beginning of the Na plating process in (f) 1 M NaFSI-EC/PC (1/1) and (g) 1 M NaFSI-FEC.

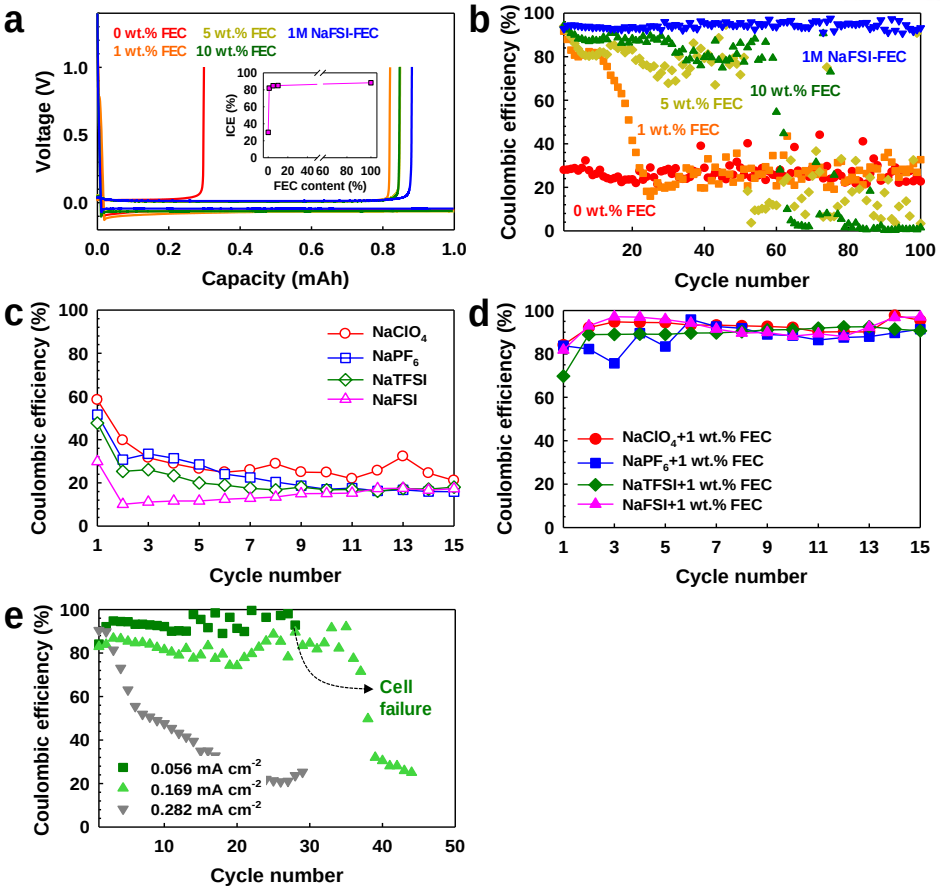

Fig. 3.3 (a) Voltage profiles for initial Na plating/stripping of Na/Cu cells in 1 M NaFSI-EC/PC (1/1) with 0, 1, 5, or 10 wt.% FEC and 1 M NaFSI-FEC at 0.056 mA cm^{-2} under 25 °C. The inset displays ICE as a function of FEC content. (b) Coulombic efficiency of Na/Cu cells at 0.282 mA cm^{-2} is shown. The areal capacity utilized from the counter Na metal electrode was 0.56 mAh cm^{-2}. Coulombic efficiency of Na/Cu cells in (c) FEC-free electrolytes and (d) FEC-containing electrolytes at 25 °C and 0.056 mA cm^{-2} over 15 cycles. (e) Coulombic efficiency of Na/Cu cells in 1 M $NaClO_4$-EC/PC (1/1)+1 wt.% FEC at 25 °C and current densities of 0.056, 0.169 and 0.282 mA cm^{-2}. Cell failure indicates that the cell voltage does not reach the cut-off condition of 1 V versus Na/Na^+ because of a short circuit by the formation and severe growth of Na dendrites on Na metal.

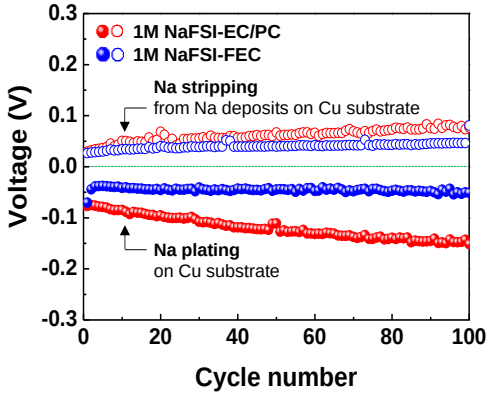

Fig. 3.4 Voltage variation for Na plating and stripping reactions at 0.28 mA cm^{-2} during 100 cycles. Voltages for Na plating and stripping are gradually decreased in 1M NaFSI-EC/PC (1/1). 1M NaFSI-FEC exhibits very stable voltage values. The areal capacity utilized from the counter Na metal electrode was 0.56 mAh cm^{-2}. Average voltage in plateau of Na plating and stripping is calculated.

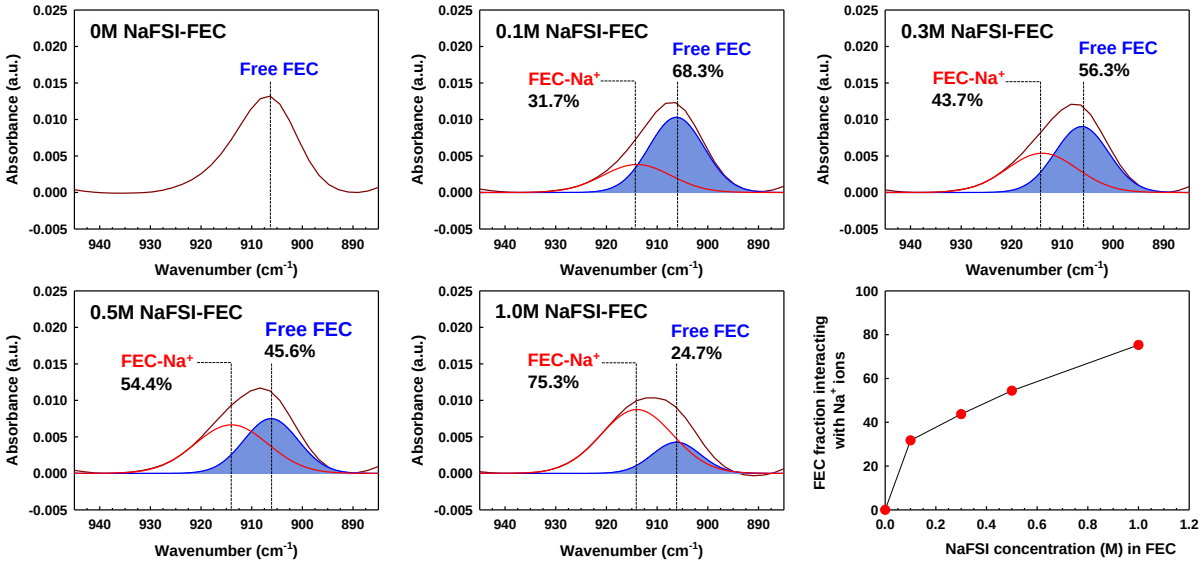

Fig. 3.5 FT-IR spectra in the FEC ring breathing mode with an increase of NaFSI concentration and the fraction of solvated FEC coordinating with Na^+ ions.

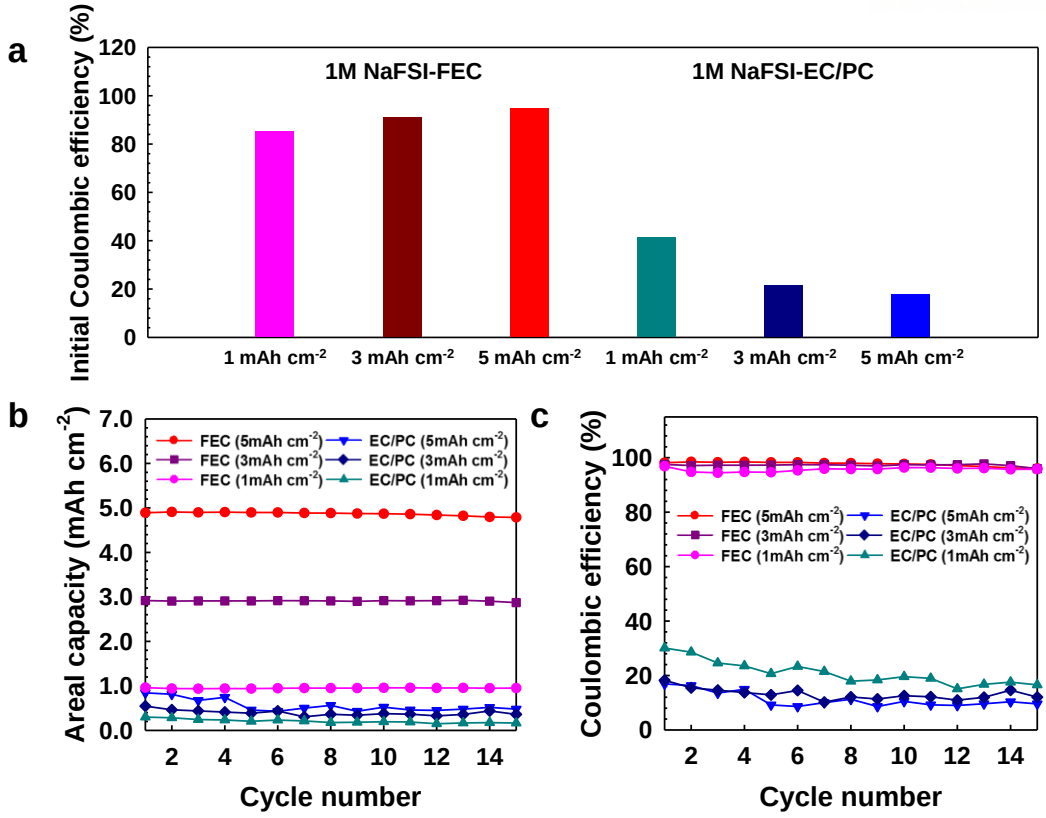

Fig. 3.6 (a) The initial Coulombic efficiency of Na/Cu coin-type cells with 1 M NaFSI-FEC and 1M NaFSI-EC/PC (1/1) at a current density of 0.5 mA cm^{-2}. (b) Capacity retention and (c) Coulombic efficiency of Na/Cu cells at various areal capacities of 1, 3 and 5 mAh cm^{-2}. The cells were cycled at 1 mA cm^{-2}.

In situ observations of the side- and top-view of Na metal deposition was performed at different stages of the initial Na plating process (Fig. 3.2d and e) to investigate the morphological difference between EC/PC- and FEC-based electrolytes. Photographs of the Cu substrate with 1 M NaFSI-EC/PC show that light ash-colored spots are partly formed during the initial steep voltage decrease from point A to B, and these spots become more distinct at point C (Fig. 3.2d). Upon increasing the Na plating time, the Na nucleation sites formed at points B and C led to the random growth of Na metal, as shown at point D. Unlike the numerous ash-colored spots at point C, the color of the Na deposits was dark brown. The origin of the darkened deposit color seems to be the byproducts produced by electrochemical decomposition of 1 M NaFSI-EC/PC. This unevenly deposited Na metal grew continuously, and finally Na dendrites became widespread the final stage of the Na plating process (point E). The side-view photograph at E point clearly shows the development of non-uniform and thick whisker-like Na metal. This dendritic Na formation can be explained by the structure of the interlayer formed on the Cu substrate. Thus, uncontrollable growth of dendritic Na metal occurs coincidentally with the non-uniform Na metal nucleation, as depicted in Fig. 3.2f. Eventually, randomly plated Na metal appeared for 1 M NaFSI-EC/PC. Dendritic-like Na metal formation via uncontrollable growth of Na metal can cause severe electrolyte decomposition and thereby a resistive interlayer obstructing Na stripping can be produced. The inferior reversibility of Na plating and stripping in 1 M NaFSI-EC/PC shown in Fig. 3.3c is ascribed to these problematic behaviors. The morphological changes in electrochemically plated Na in 1 M NaFSI-FEC were investigated by monitoring the side and top view of a Cu substrate during the initial Na plating process (Fig. 3.2e). The Cu substrate underwent a discernible color transition with 1 M NaFSI-FEC, as shown by comparing points A and B in Fig. 3.2e. This color change is closely linked to the interlayer created by electrochemical reduction of FEC, which readily accepts electrons. After point B, Na deposition is thought to proceed underneath the FEC-derived interlayer physically anchored on the Cu substrate. Relatively uniform, nondendritic, and thin Na deposition with a silver-gray color was achieved over the whole area of the Cu substrate at point D, and continued through the final stage of the Na plating process (point E). Based on in situ observation of Na deposition on Cu, we suggest that FEC creates an interlayer covering the Cu substrate at the beginning of Na plating process and this layer seems to modulate the pathway for uniform Na deposition (Fig. 3.2g). Namely, the deposition of Na^+ ions occurs underneath the FEC-derived interlayer and prevents the electron transfer out of the interlayer. Accordingly, the charge transfer reaction of Na^+ ions gaining an electron occurred underneath the FEC-derived interlayer on the Cu substrate, and this layer suppressed the uncontrollable growth of Na metal. This mechanism provides a more compact Na metal structure that is strongly bound to the Cu substrate without the dendritic growth of Na metal. This result is in good accordance with the previous reports that the dendritic Li formation was effectively suppressed by the FEC-containing

electrolytes.[21, 46, 48] Images of Na plating with increased magnification were taken after 2, 5, and 7 h, and show that significantly different Na deposition occurred in each electrolyte (Fig. 3.7). As the Na plating in 1 M NaFSI-EC/PC proceeded from 30 min (point D at Fig. 3.2d) to 2 h (Fig. 3.7c), additional Na filled the empty space on the Cu substrate along with severe growth of Na dendrites. On the other hand, no change was apparent in the side and top view images of Na deposition in 1 M NaFSI-FEC after 30 min, 2 h, 5 h, and 7 h (Fig. 3.7d). The importance of the interfacial structure for Na deposition mechanism appears to be a very rational explanation. Importantly, a highly stable voltage profile and low overpotential for Na metal plating/stripping in Na/Na symmetric cells were observed with 1M NaFSI-FEC (Fig. 3.8a). The differences in the overpotentials for Na metal plating/stripping on the Na metal electrode are more clearly shown in Fig. 3.8b. This finding indicates that the interfacial structure formed in 1M NaFSI-FEC effectively assists Na migration to the Na metal electrode and allows reversible Na metal stripping/plating in the Na/Na symmetric cell.

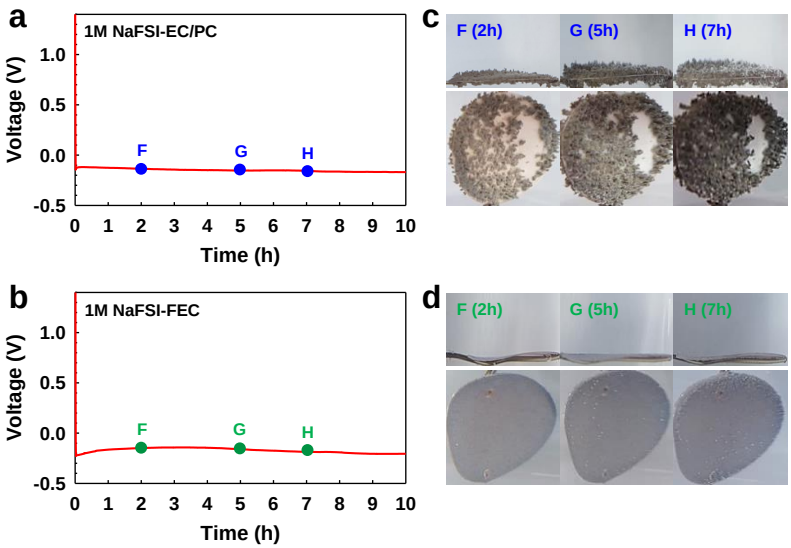

Fig. 3.7 Voltage profiles of initial Na plating on a Cu substrate in Na/Cu beaker cells and snapshot of Na metal plated on Cu substrates at specific points. Na plating was performed at 0.282 mA cm^{-2} under 25 °C. Voltage profile of a Na/Cu cell with (a) 1 M NaFSI-EC/PC (1/1) or (b) 1 M NaFSI-FEC is shown. (c) Non-uniform and thick Na metal deposition appears for 1 M NaFSI-EC/PC (1/1). (d) Uniform Na metal plating occurs in 1 M NaFSI-FEC. The areal capacity utilized from the counter Na metal electrode was 2.82 mAh cm^{-2}.

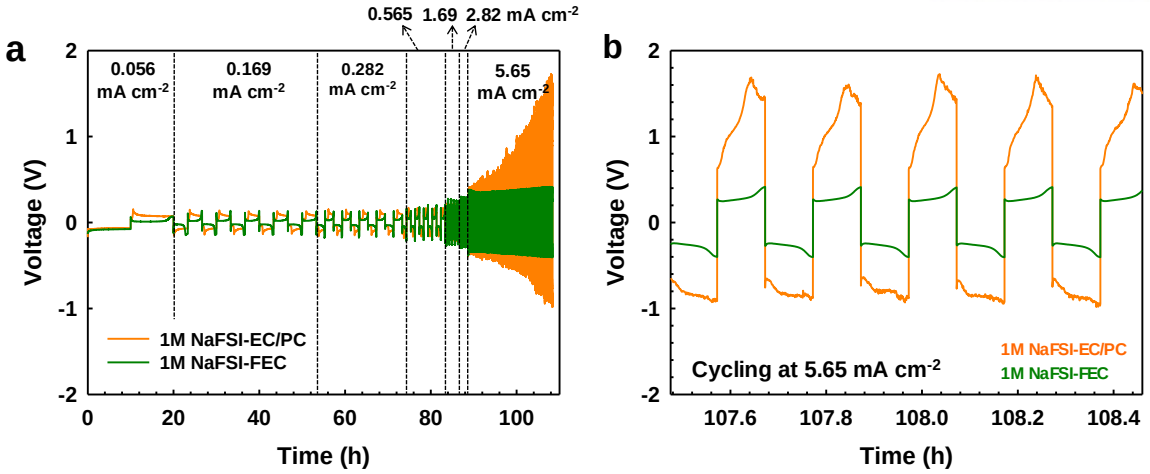

Fig. 3.8 (a) Galvanostatic cycling of Na/Na symmetric cells at various current densities of 0.056, 0.169, 0.282, 0.565, 1.69, 2.82 and 5.65 mA cm^{-2}. (b) Enlarged region showing the voltage profiles for the 96th to 100th cycle at 5.65 mA cm^{-2}.

To directly investigate the effect of the FEC-based electrolyte, we performed in situ optical microscopy to monitor electrochemical Na plating on the Cu substrate, as shown in Fig. 3.9a. It was reported that in situ optical microscopy is a powerful tool in optical recording for Na plating.[42] Both cells using 1 M NaFSI-EC/PC and NaFSI-FEC obtained a current density of 0.463 mA cm^{-2}, corresponding to an areal capacity of 1.389 mAh cm^{-2}. Before Galvanostatic cycling, electrochemical impedance spectroscopy (EIS) was carried out to compare the intrinsic resistance and the charge transfer impedance of the two cells. In Fig. 3.9b and c, the Nyquist plots of the two cells indicate that the two cells contain the same intrinsic resistance of 40 ohm and comparable charge-transfer impedance, which means that the initial state of the two cells is identical. Snapshots from the videos of the Na plating process of the two cells are shown in Fig. 3.9e and f. The gas evolution by the electrolyte decomposition was observed during Na plating and the possible mechanisms could be demonstrated in in situ differential electrochemical mass spectrometry (DEMS) analysis. Randomly grown Na deposits on the Cu substrate appeared at 36 min of Na plating in 1 M NaFSI-EC/PC, and the gray color indicates the accumulation of byproducts via an undesirable side-reaction of the electrolyte with the Na deposits. At 144 min, the Na metal was deposited in a more porous and dendritic structure, and finally, the Na deposits pierced the GFF separator at 180 min, reaching the Na metal counter electrode as a result of the uncontrolled and extensive growth of Na dendrites. In contrast, non-dendritic, compact, and silvery Na metal was electrochemically plated on a Cu substrate in the presence of 1 M NaFSI-FEC. The in situ optical microscopy result for Na deposition with 1 M NaFSI-FEC confirms that Na nucleation is even across the Cu substrate and the final structure of the Na metal deposits is fairly smooth, without the formation of dendritic Na. This result provides valuable insight for understanding the morphological evolution of Na metal. The voltage profiles (Fig. 3.10) corresponding to Fig. 3.9e and f were recorded simultaneously. Both cells show typical metal deposition shapes with peaks corresponding to the nucleation and deposition of Na metal. Although the initial impedance value of the 1 M NaFSI-EC/PC was comparable or slightly smaller than that of the FEC-based sample in the measurement of the charge-transfer impedance, the nucleation peak of the 1 M NaFSI-FEC sample appears at -0.36 V vs. Na/Na^+, while that of the 1 M NaFSI-EC/PC sample appears at -0.45 V vs. Na/Na^+. The deposition potential of the FEC-based sample is also lower than that of the EC/PC-based sample and shows a smooth shape. For 1 M NaFSI-EC/PC, the potential fluctuates from approximately 140 min to 165 min, indicative of the separator being pierced by Na dendrites. A quantitative comparison of the morphological evolution by plotting the height of the deposit at different times is shown in Fig. 3.9d. The FEC-based sample forms a clearly uniform deposition over long period of time. Na deposits with severely bumpy and more porous structures appear for 1 M NaFSI-EC/PC, as shown in the top-view image in Fig. 3.11a, and the cross-sectional SEM image (Fig. 3.12a) shows some cavities in the Na deposit layer that indicate

incomplete adhesion to the Cu substrate. This uneven and weakly bound Na metal cannot assure the reversible electrochemical oxidation of Na metal donating electrons during the stripping process and may produce electrically isolated Na metal, namely, a "dead Na phase", that can reduce CE upon further cycling. A comparison of cross-sectional and surface morphology of Na metal electrochemically plated on a Cu substrate in 1 M NaFSI-EC/PC and 1 M NaFSI-FEC shows the outstanding characteristics of FEC as a solvent, which leads to more compact Na metal plating (Fig. 3.12a-d). In addition, a spectral study demonstrated that the structural stability of the FEC-derived interlayer is superior compared to the interlayer formed by the decomposition of 1M NaFSI-EC/PC (Fig. 3.12e and f). As shown in Fig. 3.11b, 1 M NaFSI-FEC created a non-dendritic and bean-like Na deposition with a flat and comparatively seamless structure. The cross-sectional SEM image in Fig. 3.12b clearly shows that the Na metal is uniformly bound to the Cu substrate in 1 M NaFSI-FEC. Surface morphology and side-view images of Na deposits on a Cu substrate at high current densities and high areal capacities are given in Fig. 3.13, 3.14 and 3.15. During initial Na plating in 1 M NaFSI-EC/PC at high current density of 10 mA cm^{-2}, uncontrollable growth of dendritic Na metal at specific zones occurs coincidentally with the non-uniform Na metal nucleation and many voids are generated (Fig. 3.14). On contrary, uniform and dense Na plating without voids was achieved in 1 M NaFSI-FEC that constructs the interlayer providing the pathway for uniform Na deposition.

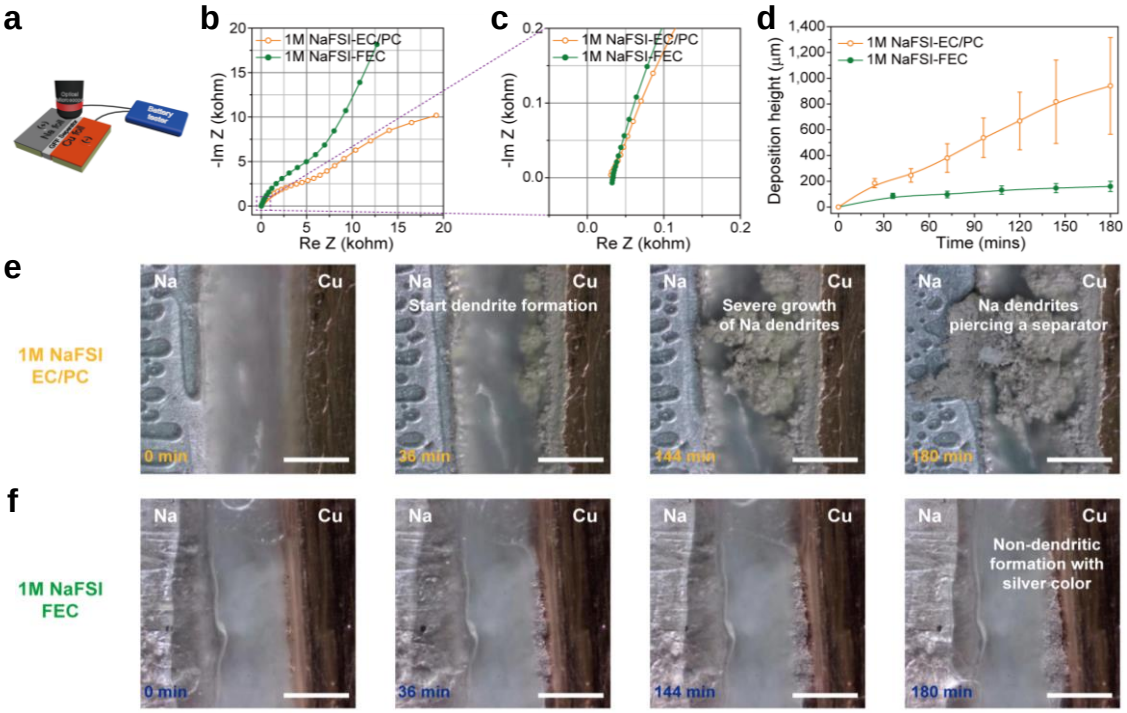

Fig. 3.9 (a) Schematic of the in situ optical microscopy setup for monitoring Na metal deposition. (b) Electrochemical impedance spectra of the two cells using 1 M NaFSI-EC/PC (1/1) and 1 M NaFSI-FEC electrolytes. (c) Magnification of the electrochemical impedance spectra in (b) to compare the intrinsic resistance of the two cells. (d) The average height and standard deviation of the Na deposition as a function of time for the two cells during the initial Na plating at 0.463 mA cm^{-2}. Cross-sectional optical images of Na plated on Cu substrates with (e) 1 M NaFSI-EC/PC (1/1) and (f) 1 M NaFSI-FEC obtained using in situ optical microscopy. All white scale bars represent 500 μm.

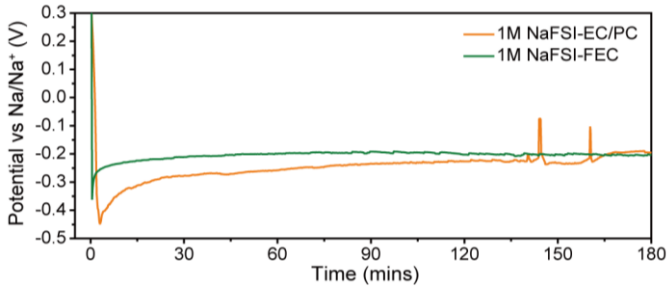

Fig. 3.10 Voltage profiles of Na deposition on the two cells, corresponding to the snapshots in Fig 3.9e and f.

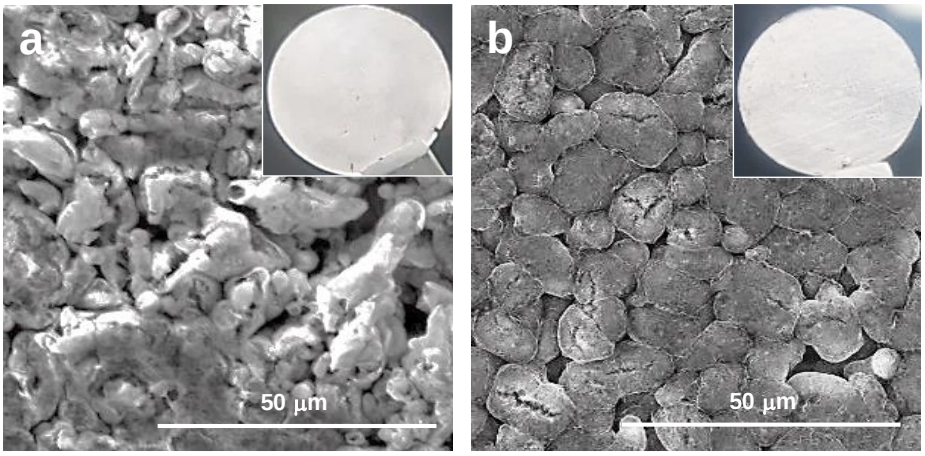

Fig. 3.11 Surface morphology of Na metal electrochemically plated on a Cu substrate in (a) 1 M NaFSI-EC/PC (1/1) and (b) 1 M NaFSI-FEC at 0.28 mA cm^{-2} during the initial Na plating process. The insets of (a) and (b) show optical images of Na metal plated on a Cu substrate.

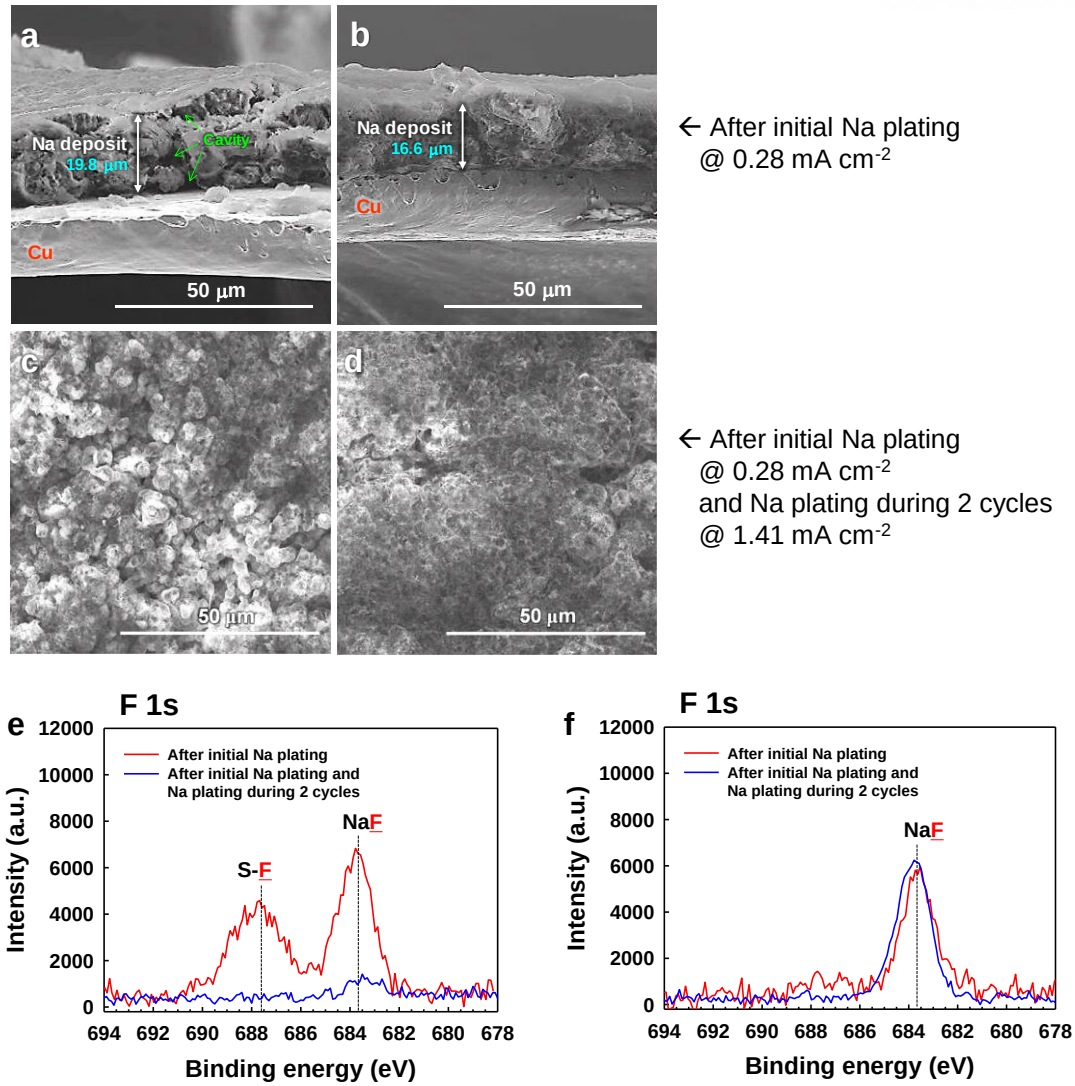

Fig. 3.12 Cross-sectional SEM images of Na deposits on a Cu substrate in a coin-type Na/Cu cell with (a) 1 M NaFSI-EC/PC (1/1) or (b) 1 M NaFSI-FEC after initial Na plating at 0.28 mA cm^{-2}. Surface morphology of Na deposits with (c) 1 M NaFSI-EC/PC or (d) 1 M NaFSI-FEC after initial Na plating at 0.28 mA cm^{-2} and Na plating during 2 cycles at 1.41 mA cm^{-2}. The areal capacity utilized from the counter Na metal electrode was 2.82 mAh cm^{-2}. F 1s XPS spectra of Na metal surface electrochemically plated on a Cu substrate with (e) 1M NaFSI-EC/PC or (f) 1M NaFSI-FEC during the initial Na plating at 0.28 mA cm^{-2} and Na plating during 2 cycles at 1.41 mA cm^{-2}.

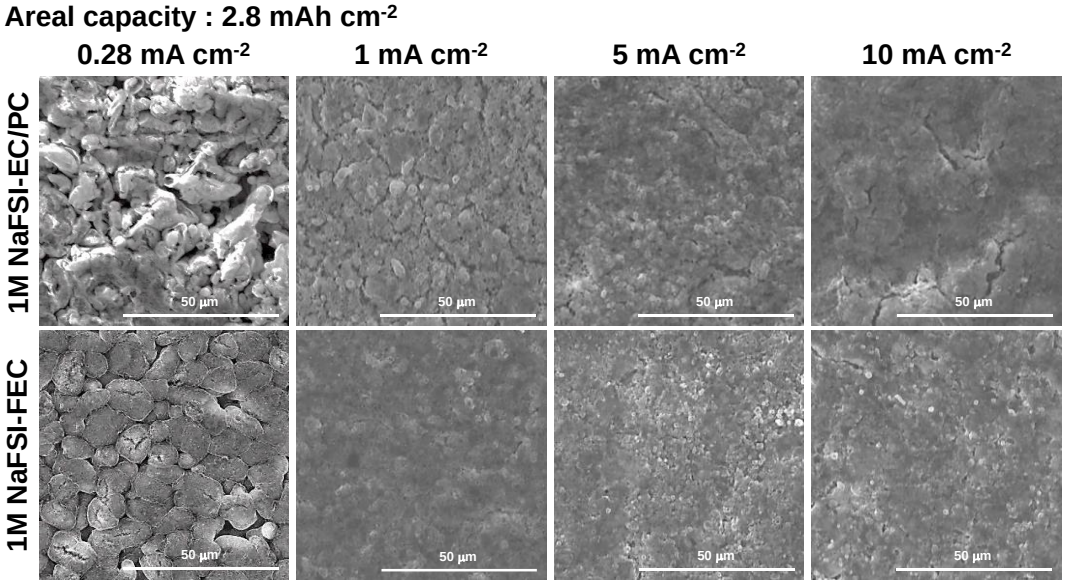

Fig. 3.13 Surface morphology of Na metal electrochemically plated on a Cu substrate in 1 M NaFSI-EC/PC (1/1) and 1 M NaFSI-FEC at current densities of 0.28, 1, 5 and 10 mA cm^{-2} during the initial Na plating process. The areal capacity utilized from the counter Na metal electrode was 2.8 mAh cm^{-2}.

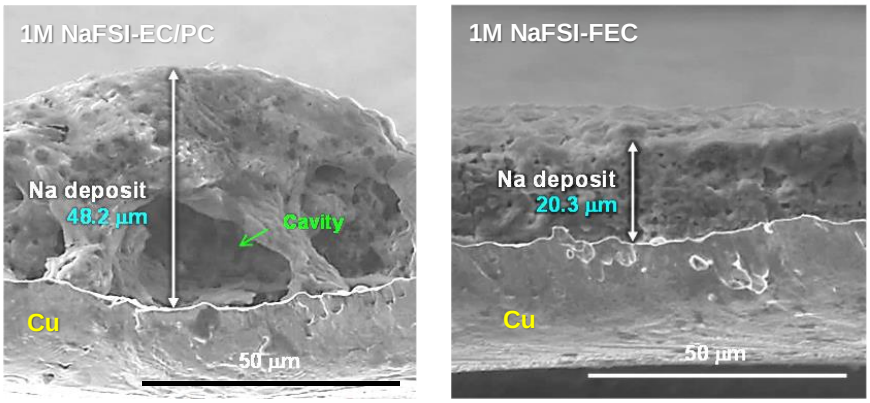

Fig. 3.14 Side-view images of Na metal electrochemically plated on a Cu substrate in 1 M NaFSI-EC/PC (1/1) and 1 M NaFSI-FEC at a high current density of 10 mA cm^{-2} during the initial Na plating process. The areal capacity utilized from the counter Na metal electrode was 2.8 mAh cm^{-2}.

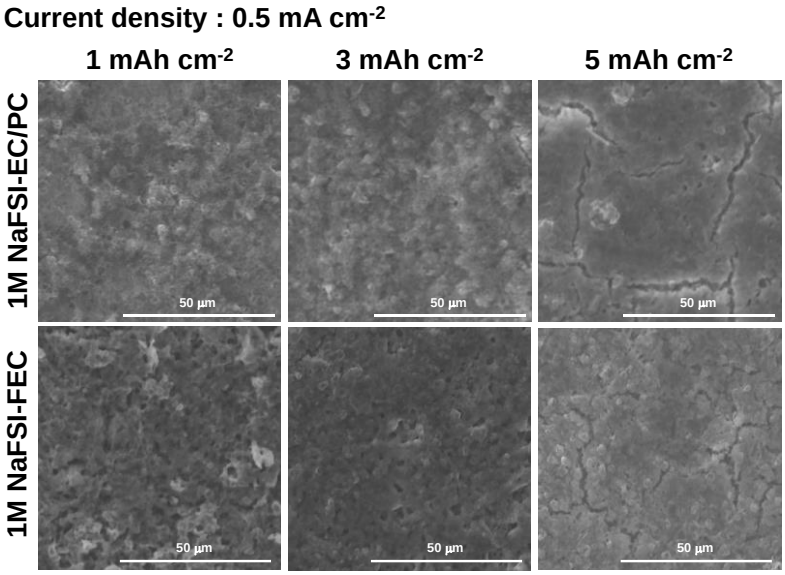

Fig. 3.15 Surface morphology of Na metal electrochemically plated on a Cu substrate in 1 M NaFSI-EC/PC (1/1) and 1 M NaFSI-FEC at a current density of 0.5 mA cm^{-2} during the initial Na plating process. The areal capacities utilized from the counter Na metal electrode were 1, 3 and 5 mAh cm^{-2}.

Ex situ X-ray photoelectron spectroscopy (XPS) measurements of Na deposits on a Cu substrate were performed to determine the origin of the outstanding reversibility of the Na plating and stripping processes and dendrite-free Na metal deposition in 1 M NaFSI-FEC. The F 1s spectra in Fig. 3.16 reveal that with 1 M NaFSI-EC/PC the interfacial layer covering Na metal deposits contains an S-F intermediate and NaF, which are known to be generated by the reductive decomposition of the FSI anion.[49-50] The S-F peak at around 688 eV, which was not observed in the spectrum of FEC-containing electrolytes (1 M NaFSI-EC/PC with 1 wt.% FEC and 1 M NaFSI-FEC), is distinct to FEC-free electrolytes systems involving FSI (-N(SO_2-F)$_2$) anion decomposition. As depicted in pathway 1-E, 2, 4-B, and 5-A of Fig. 3.17,[51-54] NaF is one of the main products of FEC decomposition. According to the recent study by the Tateyama group,[55] it can be supposed that the F ions of NaF attractively interact with Na^+ ions of sodium alkylcarbonates (NaO_2CO-R-) in the interfacial layer, and it is possible that this intermolecular interaction promotes the mechanical integrity of the interfacial layer such that it can withstand the volume changes inevitably induced by the surface reaction (Na plating process: $Na^+ + e^- \rightarrow$ Na). The Cui group's demonstration of the unique nature of NaF in the interfacial layer indicates that the high shear modulus of 31.4 GPa of the interfacial layer can inhibit the formation of dendritic Na metal, which has a low shear modulus of 3.3 Gpa.[43] The atomic force microscope (AFM) indentation tests clearly showed that the applied force for the FEC-derived interlayer including NaF is relatively higher compared to the interlayer formed by 1M NaFSI-EC/PC decomposition (Fig. 3.18). The NaF derived from the FEC decomposition is believed to enable dendrite-free, uniform, and dense Na plating (Fig. 3.2e and 3.11b) via a surface reaction. The disappearance of the S-F peak likely occurs because FEC mostly prevents NaFSI decomposition during Na plating on the Cu substrate. It is worth noting that the reductive decomposition of FEC progresses readily in contact with Li and Na metal electrodes, and the resulting FEC-derived interfacial layer effectively inhibits the decomposition of other components in the electrolyte. [19, 22, 45, 56] Further evidence for the existence of FSI anion decomposition byproducts in 1 M NaFSI-EC/PC is shown in the N 1s spectra of Na metal deposits in Fig. 3.16. No peak corresponding to N-SO_2 intermediate appeared for FEC-containing electrolytes. The creation of an outstanding interfacial layer via FEC decomposition is evident in the C 1s XPS spectra obtained from Na metal deposits in FEC-containing electrolytes. The introduction of 1 wt.% FEC to the 1 M NaFSI-EC/PC electrolyte alleviated the formation of Na_2CO_3 at 289.8 eV through the ring-opening decomposition of EC and reaction with Na ions and electrons. Despite the absence of EC molecules, a Na_2CO_3 peak appeared for 1 M NaFSI-FEC. This occurrence is attributed to the creation of Na_2CO_3 by the reductive decomposition of FEC, as illustrated in pathway 1-B, 1-C, 4-B, and 5-B of Fig. 3.17.[52-54, 57-58] Interestingly, the peak intensity at 289.2 eV was profoundly increased, even with a small amount of 1 wt.% FEC in the electrolyte. A greater increase in peak intensity was observed in 1 M NaFSI-FEC.

This peak can be attributed to R_1-OCO_2Na (pathway 1-D) and/or R_2-OCO_2Na (pathway 4-A), as proposed in the possible mechanisms for FEC decomposition in Fig. 3.17. It was expected that the R_1 and R_2 groups chemically bonded to carbonate (-OCO_2) structures in the interlayer fulfill an elastic function, mitigating the mechanical stress induced by the Na metal deposition occurring underneath it. Moreover, the ether peak at 286.5 eV, which is one of the constituents of the interlayer via ring opening polymerization of EC molecule, was discernibly reduced. According to previous reports, ring opening polymerization of EC can occur in the presence of basic catalysts such as KOH, CH_3OK, NaI, and NaCl, forming polymer species with carbonate and ether linkages.[59] In the case of 1 M NaFSI-EC/PC, the NaFSI salt is prone to decomposition, electrochemically generating NaF during Na metal plating. The formed NaF may act as a basic catalyst for the ring opening polymerization of EC, leading to the creation of ether-containing compounds. Fig. 3.16 shows a clear peak attributed to C–O bonds for 1 M NaFSI-FEC without EC. This peak is mostly attributed to environments containing a single oxygen atom (e.g., R-ONa) chemically bonded to an anhydride moiety produced by the one-electron decomposition of FEC, as shown in pathway 3 of Fig. 3.17. A noticeable feature is that a pronounced peak corresponding to carbon doubly bonded to oxygen (C=O) appears at 288.3 eV relative to 1 M NaFSI-EC/PC and its peak position is slightly different with the C=O peak at 288.0 eV generated in 1 M NaFSI-EC/PC. The structure of decomposition products chemically bonded to a C=O group induced by the FEC decomposition is thought to differ from the C=O-containing compounds arising from EC/PC decomposition. Compounds with the anhydride motif, including R-ONa, can be formed through the combination of an active radical (•CHF-CH_2-OCO_2-) with FEC molecules.[60] Based on the XPS results and previous literature reports of the various routes of FEC decomposition,[19, 52-54, 58, 60-63] the possible mechanisms of electrochemical decomposition of FEC on the Na metal are represented in Fig. 3.17. The characteristic poly(vinylidene carbonate) (poly(VC)) formed by polymerization of VC did not appear for 1 M NaFSI-FEC, as shown in Fig. 3.16. These results suggest that the formation of poly(VC) by pathway 1-A of Fig. 3.17 is not a feasible mechanism for FEC decomposition during the Na plating process. We suggest that the defluorination of FEC occurs by the catalytic effects of the Na metal formed during the Na plating process, and leads to the formation of VC and HF. VC may undergo further reductive decomposition to generate Na_2CO_3 and R_1-OCO_2Na by accepting Na^+ and an electron, as shown in pathway 1-B, 1-C, and 1-D of Fig. 3.17. The feasible reactions were identified by gas analysis using in situ DEMS (Fig. 3.19). The formed HF directly reacts with Na metal, forming NaF and H_2 (pathway 1-E of Fig. 3.17). The appearance of peaks corresponding to NaF and Na_2CO_3 in the F 1s and C 1s spectra in Fig. 3.16 shows that pathway 1-B, 1-E, 4-B, 5-A, and 5-B are valid for FEC decomposition (Fig. 3.17). Notably, the peak attributed to carbon-carbon double bond (C=C) at 284.0 eV is observed for FEC-containing electrolytes (1 M NaFSI-EC/PC with 1 wt.% FEC and 1 M NaFSI-

FEC) (Fig. 3.16). The appearance of the C=C double bond can be explained by olefin motif formed via pathway 5-A of Fig. 3.17. Additionally, the peaks attributed to the anhydride-like species (288.3 eV) and R-OCO_2Na (289.2 eV) support the FEC decomposition mechanism following pathway 1-B, 1-D, 3, and 4-A of Fig. 3.17. As shown in the C 1s XPS spectra of Fig. 3.20, the peak intensity at 288.3 and 289.2 eV was weak for 1 M NaFSI-VC compared with that for 1 M NaFSI-FEC, providing convincing evidence that the creation of R-OCO_2Na and anhydride (CO_2-CO)-containing compounds predominately occurs in 1 M NaFSI-FEC during Na metal plating on a Cu substrate. In addition, the reductive decomposition reactions of VC molecules do not include the formation of carbon singly bonded to oxygen located at 286.3 eV. Because VC contains no F, we confirmed that the Na-F signal on Na deposits formed in 1 M NaFSI-VC comes from NaFSI salt decomposition (see F 1s core levels of Fig. 3.20). A comparison of the F 1s core levels of 1 M NaFSI-VC and 1 M NaFSI-FEC shows that NaFSI salt decomposes to a greater degree because a more pronounced Na-F signal appeared for 1 M NaFSI-VC. Further evidence of NaFSI salt decomposition in 1 M NaFSI-VC is shown by the N 1s spectra of Fig. 3.20.

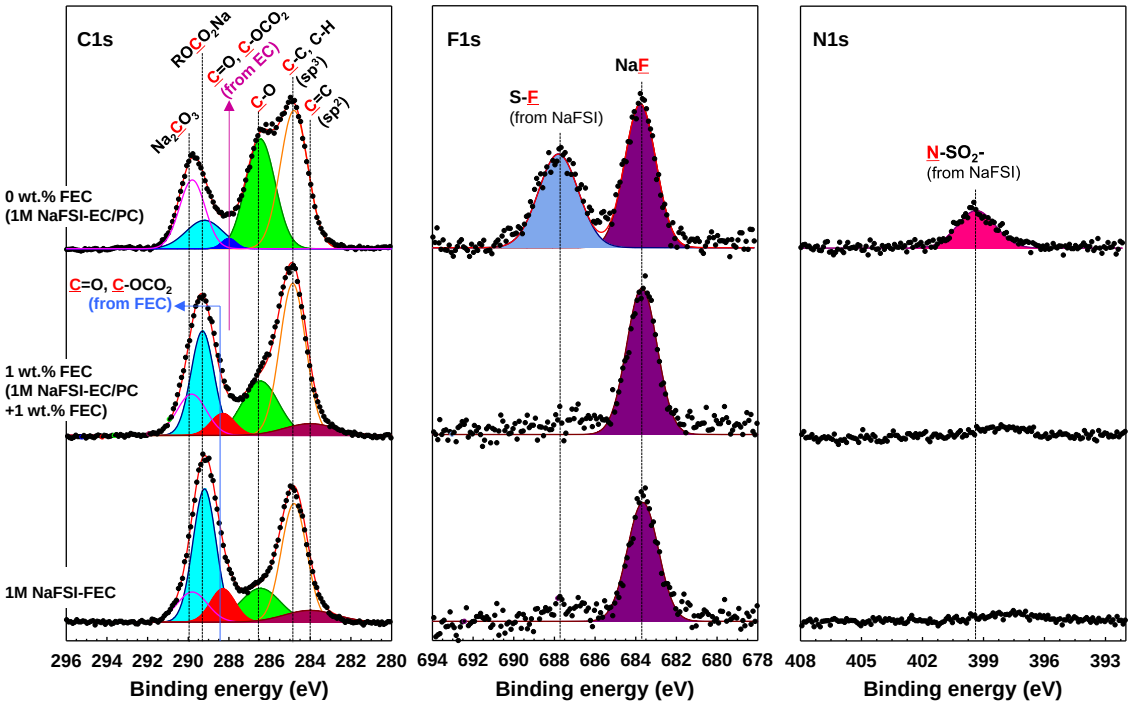

Fig. 3.16 The C 1s, F 1s and N 1s core level spectra of Na metal surface electrochemically plated on a Cu substrate during the initial Na plating at a current density of 0.28 mA cm^{-2}.

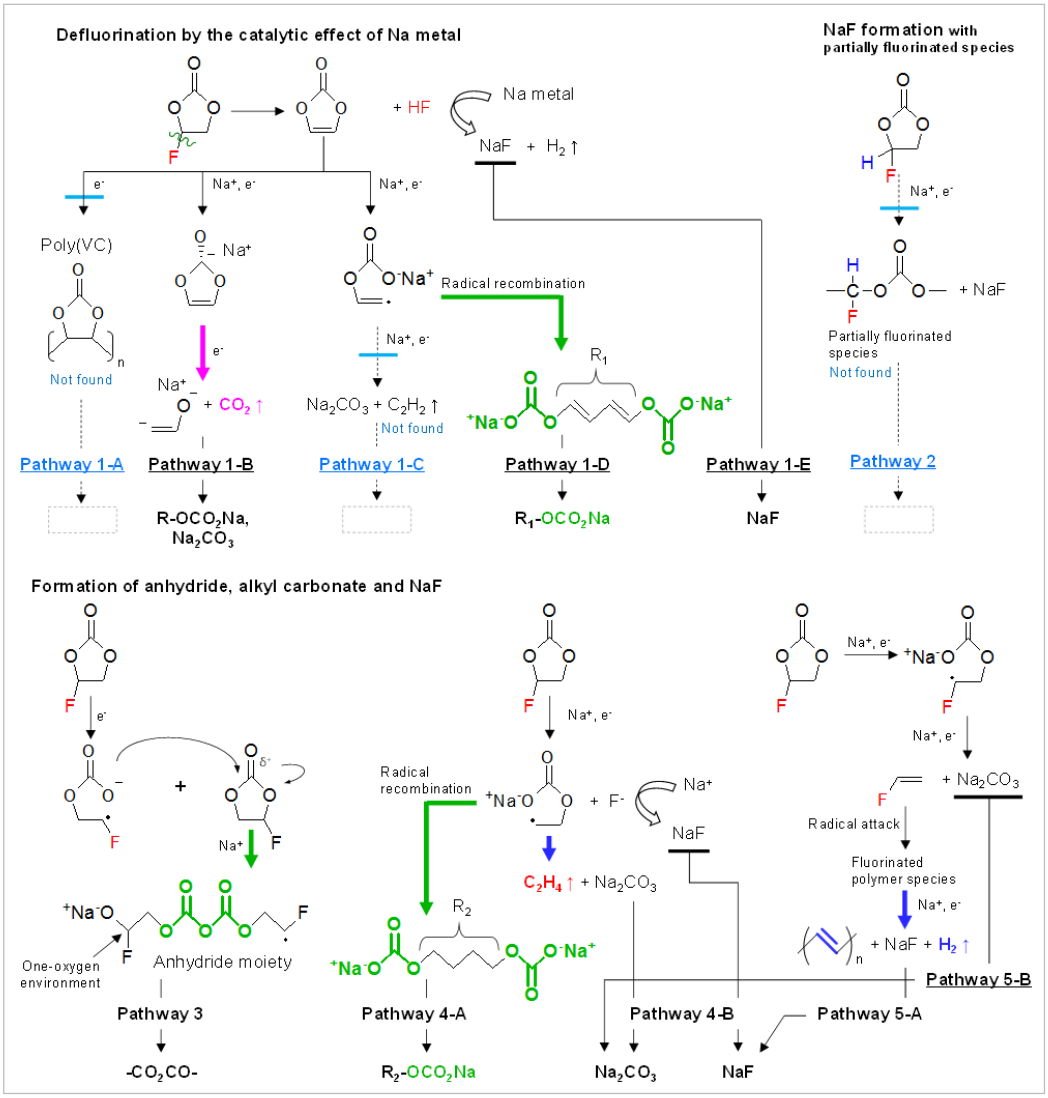

Fig. 3.17 Possible mechanisms for the construction of the FEC-derived interlayer. The reductive decomposition reactions of FEC molecules for the formation of ionic compounds possessing carbonyl-functionalized moieties, such as -OCO_2CO_2- and -OCO_2-, highlighted in green, and NaF as main interlayer components.

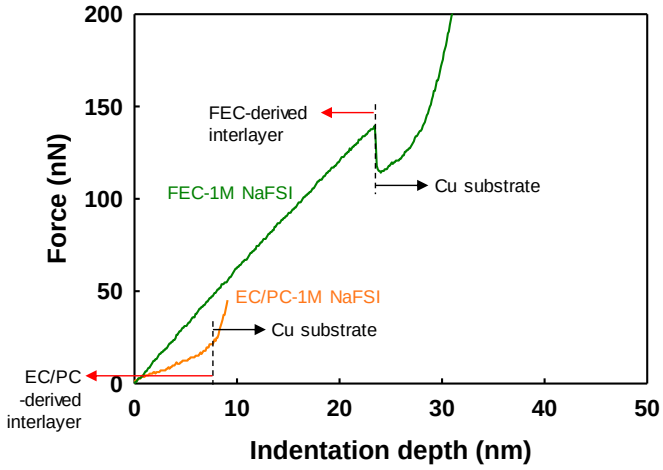

Fig. 3.18 Typical force–distance loading curves corresponding to indent locations on the EC/PC- or FEC-derived interlayer formed on the Cu substrate during initial Na plating process at 0.28 mA cm^{-2}. A cathodic current (0.28 mA cm^{-2}) was applied during 70 s for EC/PC-1M NaFSI and 60 s for FEC-1M NaFSI with negligible Na plating.

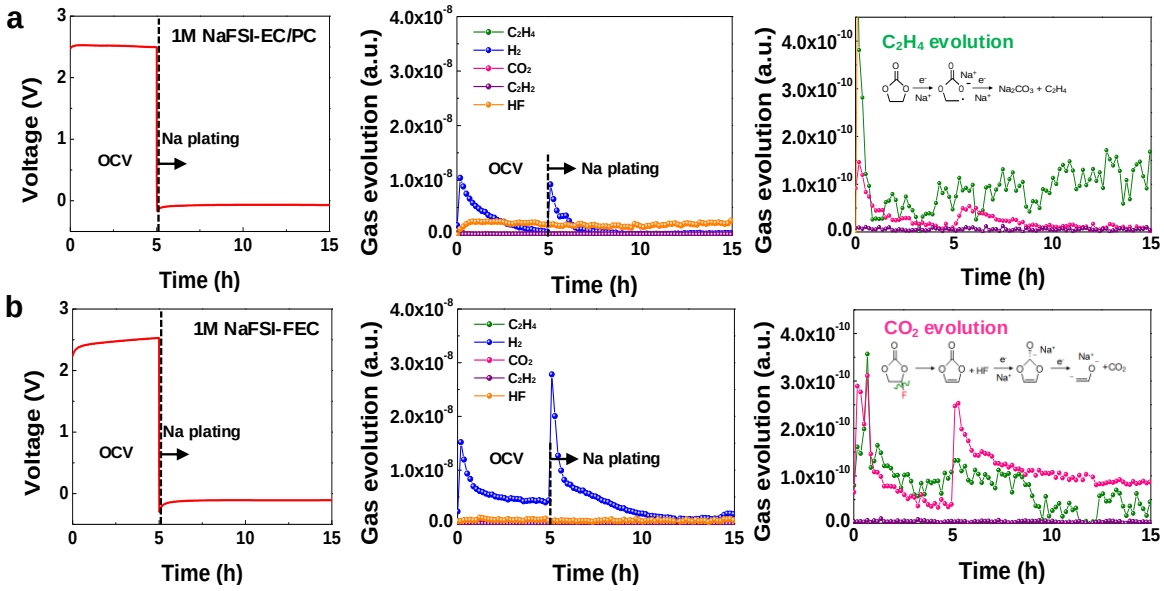

Fig. 3.19 In situ DEMS analysis of gas evolution in the Na|electrolyte|Cu cell configuration. Voltage profiles and in situ DEMS data for C_2H_4, H_2, CO_2, C_2H_2, and HF gases in the Na/Cu cells during the initial Na plating in (a) 1 M NaFSI-EC/PC (1/1) and (b) 1 M NaFSI-FEC at 0.282 mA cm^{-2} under 25 °C. The insets show the possible decomposition mechanisms of EC and FEC, which are subject to gas evolution. The OCV represents the open circuit voltage.

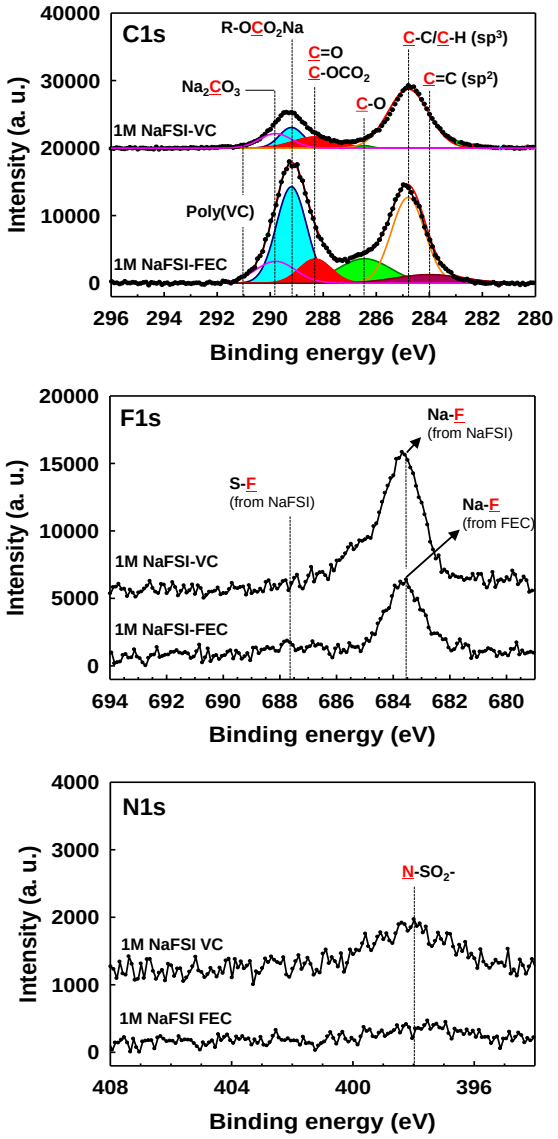

Fig. 3.20 Surface structure characterization of Na deposits by XPS. C 1s core level of Na metal plated on a Cu substrate with 1 M NaFSI-FEC and 1 M NaFSI-VC. The initial Na plating was carried out at 0.28 mA cm^{-2} and the areal capacity utilized from the Na metal electrode was 2.82 mAh cm^{-2}.

We suggest that VC does not develop an interfacial layer capable of suppressing NaFSI salt decomposition during Na plating and leads to inferior Na plating and stripping reversibility compared with 1 M NaFSI-FEC (Fig. 3.21). C 1s core levels of Na deposits on both a Cu substrate and a fully sodiated hard carbon electrode at a current density of 0.045 mA cm^{-2} show that no Na_2CO_3 signal appears for hard carbon electrodes with 1 M NaFSI-FEC or 1 M NaFSI-EC/PC (Fig. 3.22). FEC decomposition on a hard carbon electrode occurs less severely during initial sodiation process and leads to an interfacial layer with a relatively low fraction of R-OCO_2Na compared with 1 M NaFSI-EC/PC. This result contrasts with the C 1s spectra obtained from the Na metal deposits on the Cu substrate with 1 M NaFSI-FEC or 1 M NaFSI-EC/PC, revealing that the decomposition pathway of FEC alters significantly depending on the electrode species. Furthermore, the preferential Na^+ ion and electron donation from Na metal act as catalysts to accelerate FEC reduction. More importantly, polar carbonyl (C=O) moieties in the interlayer, which have fairly good adhesion nature to the electrode may assist the desolvation of Na^+ ions solvated by solvent molecules in the electrolyte and improve the kinetics of Na^+ ion transport to the Cu substrate. The good rate capability of Na metal with 1 M NaFSI-FEC in Fig. 3.2b can be explained by the existence of polar motifs that provide a decent pathway for fast Na^+ ion transport in the interfacial layer. Additionally, the use of sufficient FEC in the electrolyte can repair the damaged interlayer on the Na metal and possibly avoid irreversible side reactions. It is obvious that controlling the surface chemistry of the Na metal is a crucial strategy to achieve outstanding reversibility of Na plating and stripping and avoid the formation of the Na metal dendrites that cause internal short circuits of cells.

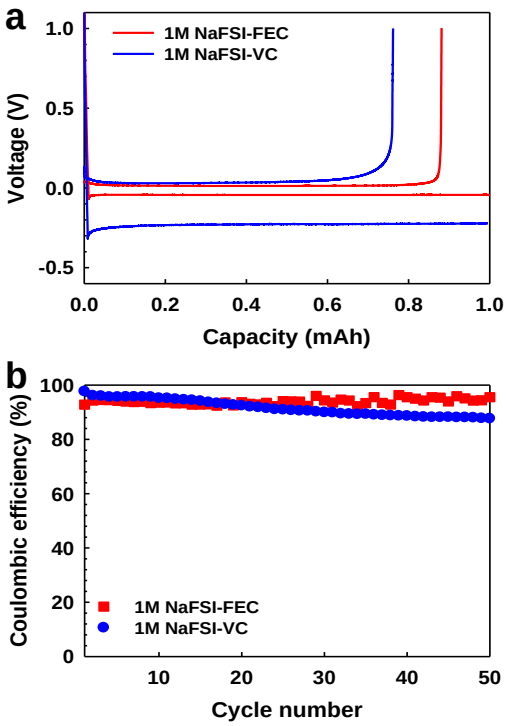

Fig. 3.21 (a) Voltage profiles for initial Na plating and stripping process in Na/Cu cells at 0.056 mA cm^{-2}. (b) Coulombic efficiency of Na/Cu cells at 0.28 mA cm^{-2}. The areal capacity utilized from the counter Na metal electrode was 0.56 mAh cm^{-2}. The electrochemical performance of Na/Cu cells with 1 M NaFSI-vinylene carbonate (VC) was evaluated at 25 °C to verify that the use of reducible compounds as the main solvent assures good cycling performances of Na metal electrodes without cell failure.

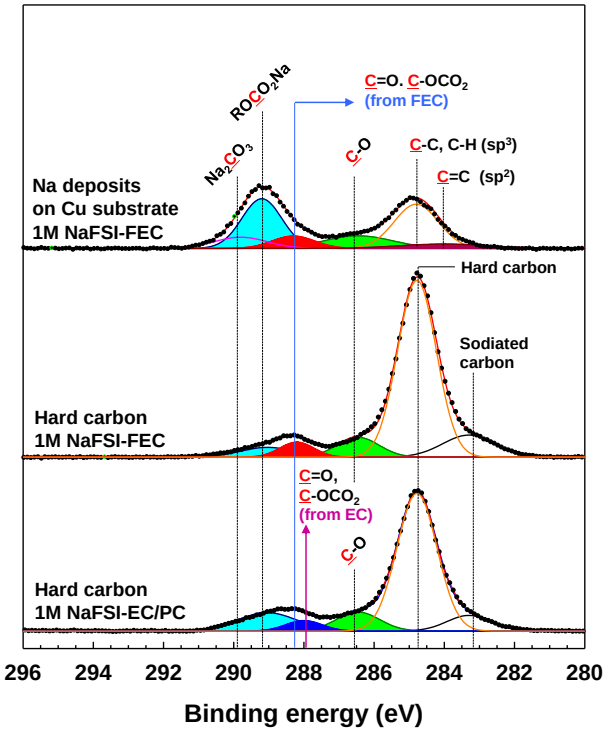

Fig. 3.22 Surface structure characterization of fully sodiated hard carbon anodes by XPS. C 1s core level of the surface of hard carbon electrode with 1 M NaFSI-FEC or 1 M NaFSI-EC/PC (1/1) is compared after full sodiation at 0.045 mA cm^{-2}. The Na plating on Cu substrate was carried out at 0.28 mA cm^{-2}. The areal capacity utilized from the Na metal electrode was 2.82 mAh cm^{-2}.

To deduce the most probable decomposition pathways of FEC molecule, in situ DEMS was employed during the Na plating process at a current density of 0.28 mA cm^{-2} (Fig. 3.19). An areal capacity of 2.82 mAh cm^{-2} was used for the Na plating process in DEMS measurements. A C_2H_4 signal was continuously detected during the initial Na plating process in 1 M NaFSI-EC/PC, whereas 1 M NaFSI-FEC evolved C_2H_4 only at the beginning of the Na plating process. The continuous evolution of C_2H_4 via pathway 4-B of Fig. 3.17 did not occur for 1 M NaFSI-FEC (Fig. 3.19b). This finding suggests that FEC makes an interlayer preventing further decomposition of FEC into C_2H_4. Trace amounts of water in the cell possibly lead to the evolution of a small quantity of H_2 for both electrolytes at the very beginning of the Na plating process. The relatively strong H_2 signal seen for 1 M NaFSI-FEC at the very beginning of the Na plating process may be ascribed to H_2 generation via pathway 1-E (HF (from FEC defluorination) + Na → NaF + H_2↑) and pathway 5-A of Fig. 3.17. While a negligible CO_2 signal was observed for 1 M NaFSI-EC/PC, a CO_2 signal was continuously detected for 1 M NaFSI-FEC, indicating that the decomposition reaction seen in pathway 1-B of FEC molecules is responsible for CO_2 formation. CO_2 may be converted into R-OCO_2Na and Na_2CO_3 by reacting with Na metal upon repeated Na plating and stripping. Among various efforts made to prevent the interfacial instability of the metal by the non-favorable interaction with organic electrolytes, CO_2 has been used to develop carbonate-oriented films to serve as an effective interlayer.[64-66] Thus, the CO_2 evolved by the decomposition of FEC molecules is expected to contribute to the formation of carbonate-based interlayer compounds such as R-OCO_2Na and Na_2CO_3 upon cycling (pathway 1-B of Fig. 3.17). The lack of C_2H_2 signal for both electrolytes indicates that pathway 1-C of Fig. 3.17 is not favored in 1 M NaFSI-FEC during Na plating, and that the reaction leading to the formation of C_2H_2 is excluded in 1 M NaFSI-EC/PC. Interestingly, the in situ DEMS result acquired from a Na/Cu cell with 1 M NaFSI-EC/PC shows an HF signal that was not observed in 1 M NaFSI-FEC. F^- ions derived from FSI anion decomposition seem to combine with H^+ generated by the decomposition of EC/PC in direct contact with the Na metal. In contrast to the case for 1 M NaFSI-FEC, which leads to HF consumption by NaF formation during the Na plating process, the formed HF in 1 M NaFSI-EC/PC was not consumed and could be detected in the in situ DEMS analysis. It is possible that EC/PC-derived interlayer minimized the direct contact between the electrolyte and Na metal. Accordingly, some of the HF generated from FSI anion decomposition was observed in the DEMS result and may be involved in the NaF formation shown in F 1s spectra of Fig. 3.16. The appearance of CO_2, C_2H_4, and H_2 signals detected by in situ DEMS analysis during initial Na plating could confirm the reductive decomposition pathways of FEC to form R-OCO_2Na (pathway 1-B), Na_2CO_3 (pathway 1-B and 4-B) and NaF (pathway 1-E and 5-A), as depicted in Fig. 3.17.

3.4 Conclusion

We have demonstrated FEC-based electrolyte to effectively suppress the dendrites of Na metal due to an interlayer decorated by FEC decomposition products, resulting in enhanced the electrochemical reversibility. Impressive cycling stability could be achieved in the new combination of FEC and NaFSI, and FEC enabled the construction of the ionic interlayer possessing superior electrochemical and structural stability upon repeated cycling. A spectral study led us to conclude that the reductive decomposition of FEC molecules occurred more readily at the highly reducing Na metal than at sodiated hard carbon electrodes and that the FEC-derived ionic interlayer including R-OCO_2Na, anhydride (CO_2-CO)-containing compounds, Na_2CO_3, and NaF was developed on the Na metal. Among the postulated mechanisms for the decomposition of FEC molecules, the most feasible pathways were confirmed by identifying the gas evolution associated with the formation of the FEC-derived interlayer through in situ DEMS analysis. In situ optical observation of the Na plating reaction confirmed that EC/PC with NaFSI was not effective in suppressing the formation and severe growth of Na dendrites, whereas FEC with NaFSI achieved homogeneous Na plating without the significant electrolyte decomposition. This study presents suitable interfacial architecture to prevent the formation of Na dendrites and improve battery safety while allowing good electrochemical reversibility of Na metal electrodes.

IV. Fluorine-enriched interfaces enhance cycling stability of 4 V class Li metal batteries in ether-based electrolytes

4.1 Introduction

The occurrence of dendritic Li growth and low Coulombic efficiency (CE) of Li plating and stripping reactions pose safety risks and result in low battery lifetime.[14-15] To resolve these critical issues, a considerable exertion has been made to develop advanced electrolyte systems through use of high salt concentration,[23, 25, 27, 67-71] sacrificial additives[21-22, 72-76] protecting reactive Li metal and less reactive solvents.[77-79] Organic carbonate-based electrolytes, which have been commonly employed for commercial Li-ion batteries, incur the generation of uncontrolled and vulnerable interfacial layers because carbonate solvents possess high electrochemical and chemical reactivity toward Li metal with highly reducing ability. On the other hand, ethers such as 1,2-dimethoxyethane (DME) are more often used as more suitable solvents for Li metal anodes allowing one to achieve improved electrochemical reversibility of Li metal and suppression of dendritic Li growth.[23] However, ether-based electrolytes cannot be used in Li batteries with 4V class cathodes, mainly because of the low upper voltage limits (<4 V *vs.* Li/Li^+) and high flammability of ethers.[24] Bis(2,2,2-trifluoroethyl) ether-added electrolytes displayed good compatibility toward 4 V-class $LiNi_{1/3}Mn_{1/3}Co_{1/3}O_2$ cathode and achieved improved cycle performance of $Li/LiNi_{1/3}Mn_{1/3}Co_{1/3}O_2$ cells with high CE of ca. 99.5% and capacity retention of >80% after 700 cycles.[25] Recently, it was demonstrated that strong Lewis basicity of ethers, which readily lose their oxygen lone pair electrons at high voltages, can be modulated by the coordination with high concentration of Li ions lowering highest occupied molecular orbital (HOMO) energy levels of ethers. This decreased HOMO energy indicates that the oxidation durability of ethers at high voltages is enhanced.[26] Although highly concentrated electrolytes inhibited growth of dendritic Li and enhanced cycling performance of Li metal anodes,[23, 27] their unsatisfactory adoptability with 4 V-class cathodes hampers practical viability of Li metal batteries. Furthermore, the introduction of electrolyte additives constructing protective layer on the surface directly above cathode can prevent the direct contact of ethers with the cathode resulting in the alleviation of unwanted oxidative decomposition of ethers.[28-29] Because severe and inhomogeneous volume changes of Li metal anodes induced by repeated Li plating and stripping reactions inflict volumetric stress on the interface, highly stress-tolerant interlayer with good ion permeability is strictly required to circumvent critical issues such as dendritic Li growth and significant CE decay of Li metal electrodes. It is noteworthy that achievement of high CE is indispensable the conservation of limited amount of Li metal anodes and long cycle life of Li metal batteries coupled with 4 V-class cathodes. However, to date, finding electrolytes with good compatibility toward the 4 V-class cathodes as well as the protection the bare Li metal anode without

Li dendrite growth has remained elusive.

Herein, we show that the use of concentrated electrolytes containing 1,1,2,2-tetrafluoroethyl-2,2,3,3-tetrafluoropropyl ether (TTE) as co-solvent and fluoroethylene carbonate (FEC) as additive allows for homogeneous and reversible reactions at Li metal anodes and results in improved anodic stability at high-capacity Ni-rich cathodes with charging cut-off voltages of >4 V *vs.* Li/Li^+. Notably, TTE promotes the formation of a stable interlayer that helps to protect the reactive Li metal, while FEC manipulates the structure of the cathode-electrolyte interface to mitigate the mechanical cracking of Ni-rich secondary particles. Furthermore, we suggest a mechanistic explanation of how TTE-promoted solid electrolyte interphase formation preserves the electrochemical reversibility of Li metal and use cross-sectional imaging to rationalize the ability of FEC to maintain the mechanical integrity of the Ni-rich cathode.

4.2 Experimental method

Electrolyte and electrodes

Electrolytes were prepared by dissolving 3.0 M lithium bis(fluorosulfonyl)imide (LiFSI, ≥99.7%, Chunbo Fine Chem Co., Ltd.) in 1,2-dimethoxyethane (DME, ≥99.9%, Aldrich) or a mixture of DME/1,1,2,2-tetrafluoroethyl-2,2,3,3-tetrafluoropropyl ether (TTE, >98.0%, TCI) prepared in 8/2 volume ratio. 1 wt.% of fluoroethylene carbonate (FEC) was added to DME and DME/TTE with 3M LiFSI. Another electrolyte was prepared by dissolving 1.15 M lithium hexafluorophosphate ($LiPF_6$, Soulbrain Co. Ltd.) in a mixture of ethylene carbonate (EC), ethylmethyl carbonate (EMC), and diethyl carbonate (DEC) in a 2/5/3 volume ratio. 1 wt.% FEC was added to EC/EMC/DEC (2/5/3) with 1.15 M $LiPF_6$. For the electrochemical tests, the electrode was prepared by spreading a slurry mixture of 95 wt.% $LiNi_{0.8}Co_{0.1}Mn_{0.1}O_2$ (NCM) as an active material, 2.5 wt.% super P as a conducting agent, and 2.5 wt.% poly(vinylidene fluoride) (PVDF) as a binder dissolved in anhydrous *N*-methyl-2-pyrrolidone (NMP, 99.5%, Aldrich) onto an aluminum (Al) foil. After drying, the electrode was pressed and then dried under vacuum at 120 °C for 12 h prior to their assembly into cells. The thickness, specific capacity, and loading density of the NCM cathode were 30 μm, 1.8 mAh cm^{-2}, and 9.8 mg cm^{-2}.

Computational details

In this study, we performed the density functional theory (DFT) calculation for three cases of calculation; highest occupied molecular orbital (HOMO) and lowest unoccupied molecular orbital (LUMO) energy levels of sovlents, decomposition mechanism of solvents. Firstly, for the calculations of orbital energy levels and decomposition mechanism of electrolyte, Beck three-parameter hybrid functional combined with Lee-Yang-Parr correlation (B3LYP) functional was used for the exchange correlation energy[80-81]. The spin-polarized calculation was adopted. The van der Waals correction was also considered by implementing a Tkatchenko-Scheffler (TS) method[82]. All electron relativistic core treatment and double numerical plus polarization (DNP) 4.4 version basis set were used to describe the core electrons and the atomic orbital basis set, respectively. The convergence criteria for geometry optimization were 1.0×10^{-5} Ha for energy, 0.002 Ha/Å for force, and 0.005 Å for displacement. The self-consistent field convergence was less than 1.0×10^{-6} Ha. To calculate the transition state in the decomposition mechanism of solvents, the complete single linear synchronous transit (LST) and quadratic synchronous transit (QST) methods were performed[83-84]. The root mean square (RMS) convergence force on the atoms was set to be 0.011 Ha/Å. All DFT calculations were performed by $DMol^3$ program[85] and an implicit environment was applied by using the conductor-like screening model

(COSMO) method[86] with the dielectric constants of four solvents (*i.e.*, TTE (6.4)[87], DME (7.2)[88], EC (95.3)[88], and FEC (78.4)[89].

Electrochemical measurements

The anodic limits of the electrolytes were determined by linear sweep voltammetry (LSV) using an Iviumstat (Ivium Technologies) at a scan rate of 1 mV s^{-1}. Al was used as the working electrode, with Li metal (100 μm thickness) as the counter and reference electrodes. 2016 coin-type cell with a Li metal electrode, a copper (Cu) substrate (1.77 cm^{-2}), and a polyethylene separator was assembled in an argon filled glove box, which contained less than 1 ppm of both oxygen and moisture, to evaluate the Coulombic efficiency (CE) of Li plating and stripping reaction. Galvanostatic pre-cycling of Li/Cu cells was performed at a current density of 0.2 mA cm^{-2} (corresponding to a 0.1C rate) using a computer-controlled battery measurement system (WonATech WBCS 3000) at 25 °C. During the initial cathodic scan, electrochemical plating of Li metal occured on the Cu substrate up to a deposited areal capacity of 2.0 mAh cm^{-2} . During the initial anodic scan, electrochemical stripping of the Li deposits on Cu substrate occured until the potential reached 1.0 V *vs.* Li/Li^+. Cycling performances were evaluated at a current density of 1 mA cm^{-2}. 2032 coin-type full cell with a Li metal electrode, a NCM cathode, and a polyethylene separator was assembled in an argon filled glove box with less than 1 ppm of both oxygen and moisture. The Li/NCM cells were precycled in the potential window between 3.0 V and 4.2 V at a rate of 0.1C. After pre-cycling, the Li/NCM cells were cycled at a rate of 0.5C. The Cu|NCM811 cells (2032 coin-type) were charge to 4.2 V at a 0.05 mA cm^{-2} to explore the reductive decomposition of FEC and TTE in 3M LiFSI in DME during Li plating on Cu.

Characterization

Contact angle measurements of the electrolytes on NCM cathode were carried out using a SEO Phoenix 300 within 2 s. Photographs of the separators after soaking for 2 min in the electrolytes were obtained. Time of flight secondary ion mass spectrometry (TOF-SIMS) measurements were performed using a spectrometer (ION TOF, Germany) at a dose density of 3.44 x 10^{13} ions cm^{-2} and an analysis area of 100 x 100 μm^2. The pressure in the chamber was maintained below 4.0 x 10^{-9} mbar. The ion maps were recorded by using a 25 keV Bi^+ ion source. The morphology of Li deposits on a Cu substrate was observed by field-emission scanning electron microscope (FE-SEM; JSM-6700F, JEOL) in a high-vacuum environment. After electroplating Li metal on the Cu substrate, the cells were disassembled in a glove box and the Li metal deposits was rinsed with a DME or DMC solvent to remove the residual

electrolyte on the electrode and then the resulting was dried in the glove box at room temperature for analysis. Ex situ X-ray photoelectron spectroscopy (XPS, Thermo Fisher Scientific Escalab 250Xi System) measurements were carried out using Al-Kα (hv = 1486.6 eV) radiation under ultrahigh vacuum. Cross-sectional images of NCM cathode particles were obtained by using an ion-milling system (IM4000Plus, Hitachi) and scanning electron microscopy (SEM, Verios 460, FEI). Combustion tests are performed by measurement of the burning time. The glass fiber filter (2 cm in width and 6 cm in length) absorbs with the electrolytes in the amount of 0.5 g and then ignited to evaluate the flammability of the electrolyte. To ensure good repeatability, every electrolyte is tested for 4 times and the average value is uesd as data. To understand the dissolution behavior of transition metal ions such as manganese (Mn), nickel (Ni), and cobalt (Co) from NCM cathodes, fully charged (de-lithiated) cathodes with various electrolytes were soaked in its cycled electrolytes under argon in a polyethylene bottle. After sealing with an aluminum pouch film, the polyethylene vial was stored in a convection oven at 60 °C for 24 h. The amount of Mn, Ni, and Co ions in the electrolyte that had come into contact with the fully charged NCM at 60 °C was measured by means of inductively coupled plasma-optical emmision spectrometers (ICP-OES, 700-ES).

4.3 Results and discussion

Compared with ethylene carbonate (EC), a commonly used key solvent in lithium (Li)-ion batteries, 1,2-dimethoxyethane (DME) has a higher-lying lowest unoccupied molecular orbital (LUMO) and is therefore less likely to be reduced at the Li metal anode (Fig. 4.1). It is expected that relatively low electron acceptance character of DME allows its applications to Li metal anodes without severe anode interface degradation. However, it cannot be employed in batteries containing 4 V-class cathodes because it has a higher highest occupied molecular orbital (HOMO) energy than EC. The poor oxidation stability of DME at the cathode can be improved by the use of oxidative additives that promote the formation of suitable cathode-electrolyte interphase (CEI) and high salt concentrations in electrolytes to reduce the fraction of free DME with high probability of decomposition at cathodes. Interestingly, fluorinated ether-based solvent, 1,1,2,2-tetrafluoroethyl-2,2,3,3-tetrafluoropropyl ether (TTE) largely replacing H with F atoms, which have electron-withdrawing character, has a very low HOMO energy level and thus, the oxidative decomposition probability by losing electrons at the cathode may lessen. Planar fluoroethylene carbonate (FEC) is more likely to accept an electron from Li metal to transform into non-planar conformation of +1e-FEC because FEC has a low LUMO energy level relative to other compounds (Fig. 4.1). Non-planar +1e-FEC may undergo the further reduction at Li metal and donate the electron to more reducible compound in the electrolyte. Because reduced TTE (+1e-TTE) has a lower LUMO energy level than +1e-FEC (Fig. 4.2), it predominantly contributes to the construction of solid electrolyte interphase (SEI) on the Li metal anode even in the presence of FEC, which has been previously employed to develop stable interface on Li metal.[19, 21] Reduced state of FEC, non-planar +1e-FEC, which has higher HOMO energy level than +1e-TTE, may lose one electron to the cathode to form planar FEC and thus the formation of a suitable CEI on the NCM811 cathode in concentrated DME-based electrolytes can be achieved (Fig. 4.2).

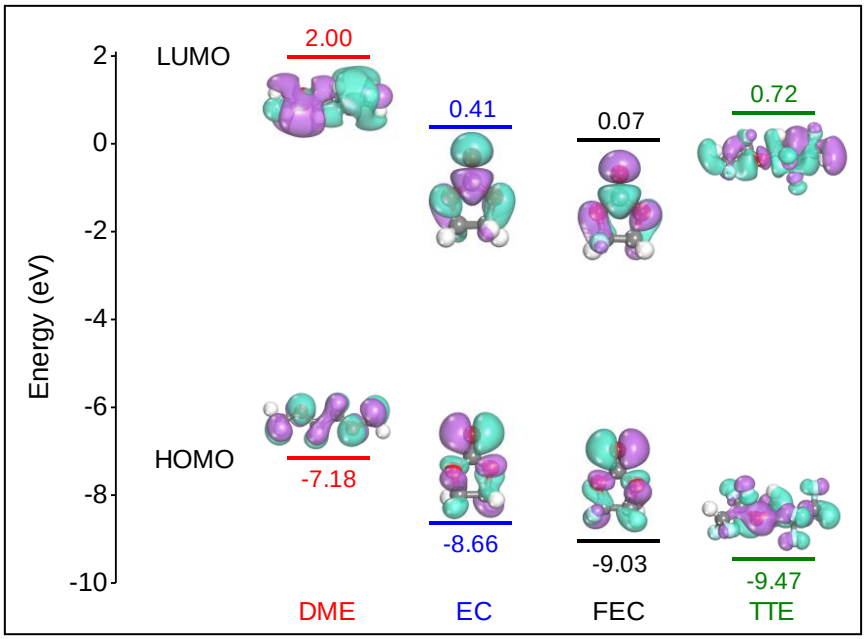

Fig. 4.1 HOMO-LUMO energy level of 1,2-dimethoxyethane (DME), ethylene carbonate (EC), fluoroethylene carbonate (FEC) and 1,1,2,2-tetrafluoroethyl-2,2,3,3-tetrafluoropropyl ether (TTE) in neutral charge of molecule through density functional theory (DFT) calculation.

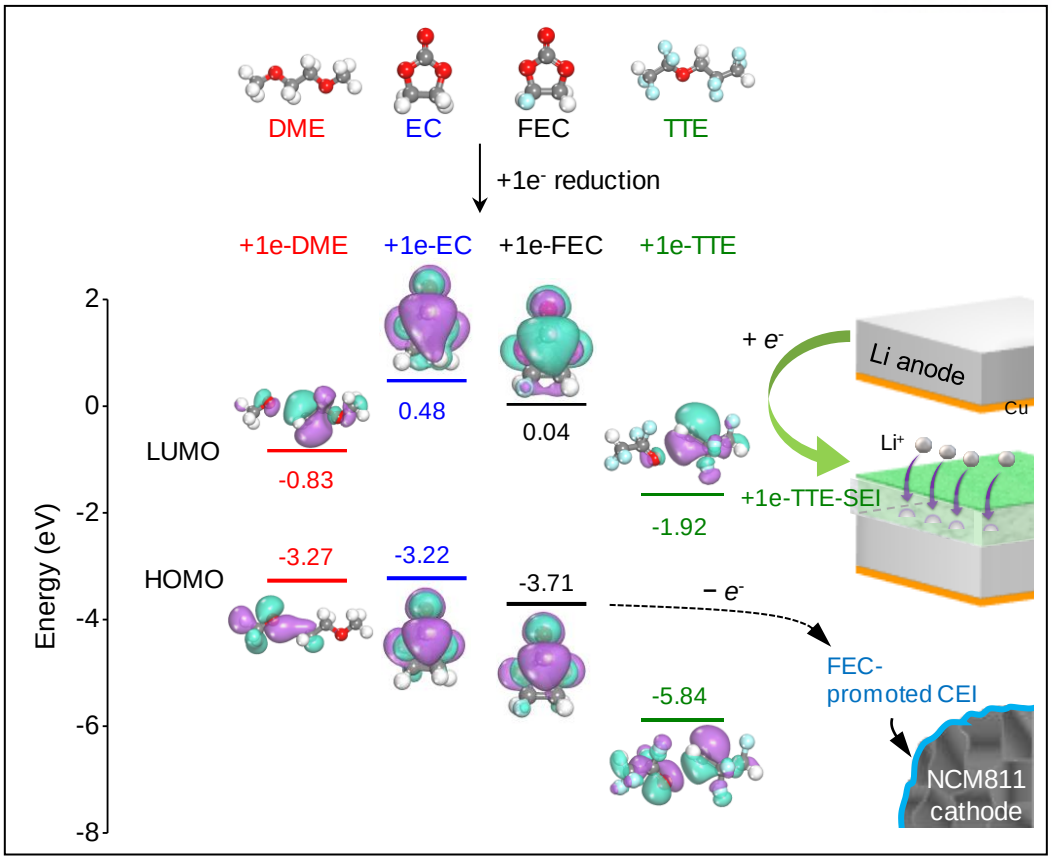

Fig. 4.2 HOMO-LUMO energy level of DME, EC, FEC and TTE in singly negatively charged states through DFT calculation. +1e and –1e represents that molecule accepts and loses one electron, respectively. Gray, white, red, and cyan spheres denote C, H, O, and F atoms, respectively.

The effects of adding TTE and FEC to concentrated DME-based electrolytes on the cycling performance of Li metal anodes were explored using Li|Cu cells (Fig. 4.3). As a control, 1.15M $LiPF_6$-EC/ethylmethyl carbonate (EMC)/diethyl carbonate (DEC) (2/5/3) with 1% FEC (Carbonate+FEC) electrolyte produced a large overpotential of -290 mV at initial stages of the first cathodic scan for the current density of 0.2 mA cm^{-2} (corresponding to areal capacity of 2 mAh cm^{-2}) (Fig. 4.3a). Carbonate+FEC electrolyte, which showed a high Coulombic efficiency (CE) value of 93.7% for initial Li plating and stripping reaction due to the capability of FEC developing stable interfacial layer on Li metal, did not allow the reversible Li plating and stripping in the Li|Cu cell upon repeated cycling and led to severe CE decay and cell failure at the 13^{th} cycle (Fig. 4.3a). This is because intrinsically high reactivity of carbonate-based electrolytes toward Li metal induces resistive compounds making the Li stripping from Li metal sluggish and the Li deposits on the Cu electrode are severely consumed by the irreversible decomposition of carbonate-based electrolytes. In contrast, concentrated electrolyte, 3M lithium bis(fluorosulfonyl)imide (LiFSI) in DME (denoted as DME) had drastically reduced initial overpotential of -49 mV thanks to its reduced fraction of free DME with high reactivity toward Li metal, whereas a very low initial CE (ICE) of 20.4% appeared (Fig. 4.3a) and exhibited very unstable CE values appeared after 100 cycles with a relatively large negative overpotential of -83 mV induced by high ohmic polarization for the Li plating on Cu (Figs. 4.3b and e). The positive role of FEC drastically enhancing the reversibility of initial Li plating and stripping reaction was not realized in cycling of Li|Cu cells (Fig. 4.3e). This implies that 1 wt% FEC may only be effective for a few hundred cycles, but is insufficient for maintaining the FEC-oriented surface film that can serve as a shield against continuous electrolyte decomposition on Li metal upon repeated cycling. We employed TTE, which possesses high probability of reductive decomposition to form interfacial layer on the Li metal, as a co-solvent in 3M LiFSI-DME with 1% FEC (DME+FEC) and the addition of TTE led to increased ICE of 89.1% compared with DME+FEC electrolyte. Additionally, unlike DME+FEC that exhibited the termination of cycling at 192^{nd}, 3M LiFSI-DME/TTE (8/2)+1% FEC (DME+TTE+FEC) electrolyte substantially enhanced the cycling stability of Li metal in Li|Cu cells while delivering high CE of ca. 99.3% over 500 cycles and having small overpotentials of ± 66 mV for Li plating and stripping (Figs. 4.3d and e).

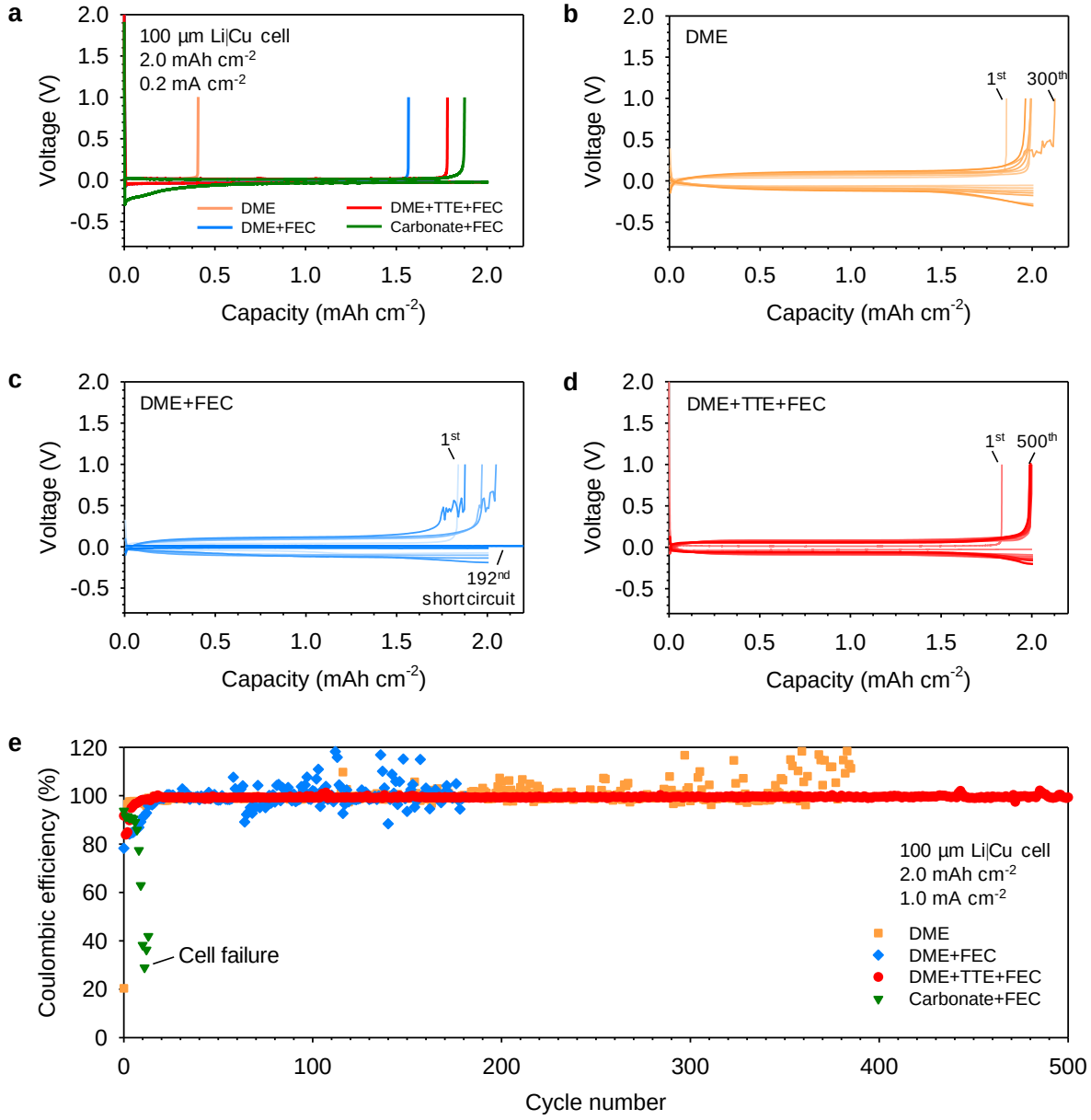

Fig. 4.3 (a) Voltage profiles for the initial Li plating and stripping reactions in Li/Cu cells with various electrolytes at a current density of 0.2 mA cm^{-2} and 25 °C. (b) Coulombic efficiency of Li/Cu cells at a current density of 1 mA cm^{-2} and 25 °C. Voltage profiles of Li/Cu cells in (c) DME (3M LiFSI-DME), (d) DME+FEC (3M LiFSI-DME+1% FEC), (e) DME+TTE+FEC (3M LiFSI-DME/TTE (8/2)+1% FEC) and (f) Carbonate+FEC (1.15M $LiPF_6$-EC/EMC/DEC (2/5/3)+1% FEC). The areal capacity utilized from the counter Li metal electrode was 2 mAh cm^{-2}.

It is plausible that TTE helps the formation of stable interfacial structures allowing reversible Li plating and stripping upon repeated cycling. Interestingly, DME+TTE electrolyte without FEC delievered very low ICE of 41.9% (Fig. 4.4). This shortage of capacity loss by severe reduction of TTE during initial Li plating can be explained by the important ability of FEC that tunes the TTE reduction on Li metal. During initial Li plating, FEC preferentially adsorbed on the Li(001) surface thanks to its relatively low adsorption energy and FEC with electrophilic nature undergoes the ring opening to form +1e-FEC (Figs. 4.5a and b). After the electrochemical reduction of FEC on Li metal, TTE gains electrons accumulated in the vicinity of the Li metal to produce +1e-TTE with higher electron affinity. A comparison of ICE values of DME+TTE electrolytes with and without FEC and adsorption energy of FEC and TTE suggests that +1e-FEC formed on Li metal may tune TTE reduction desirably without severe Li consumption.

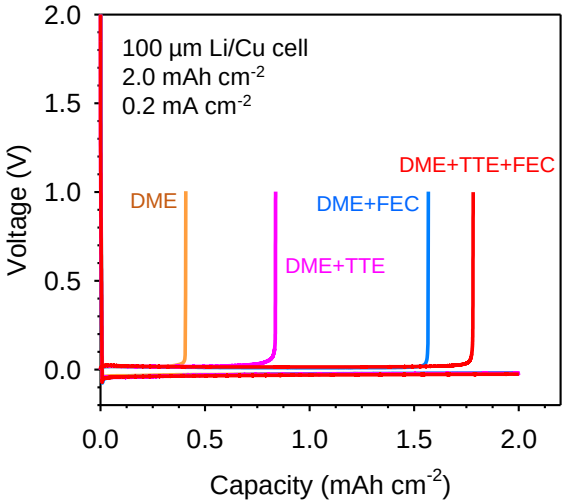

Fig. 4.4 Voltage profiles for the initial Li plating and stripping reactions in Li|Cu cells with various electrolytes at a current density of 0.2 mA cm^{-2} and 25 °C (DME+TTE: 3M LiFSI-DME/TTE (8/2)).

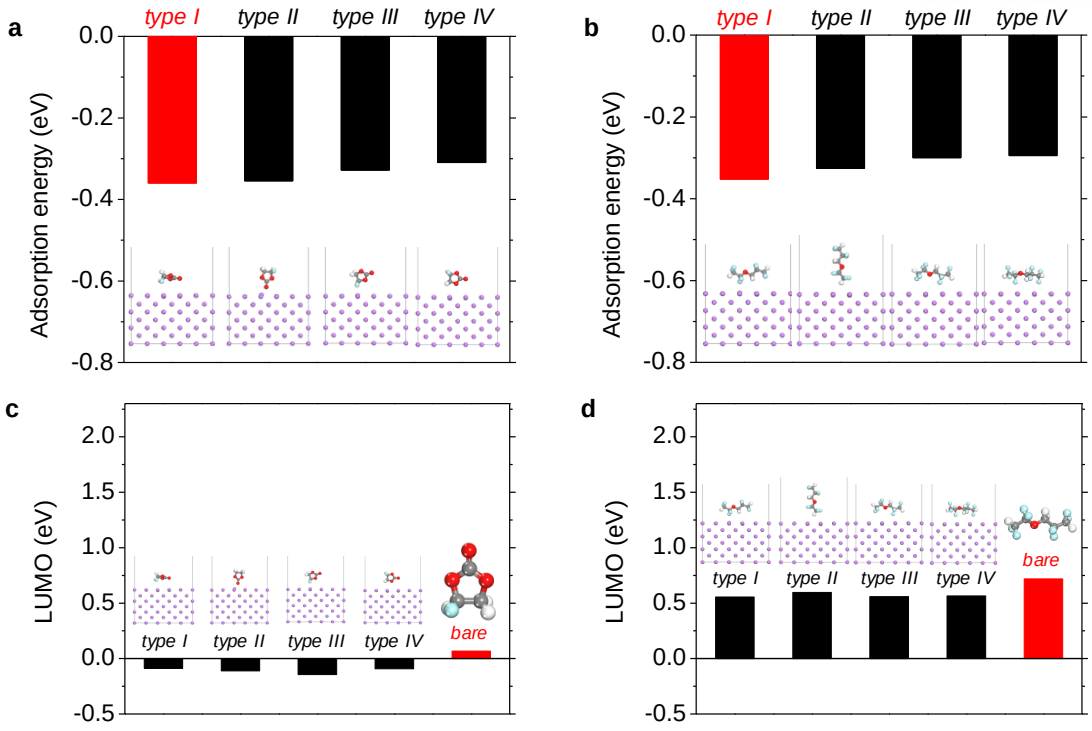

Fig. 4.5 Adsorption energy of (a) FEC and (b) TTE on Li(001) surface. LUMO energy level of (c) adsorbed FEC and (d) TTE on Li(001) surface.

To verify the role of FEC controlling the reduction of TTE during initial Li plating, the differential capacity (dQ/dV) plots were obtained in Cu|NCM811 cell configuration (Fig. 4.6). FEC in DME+TTE+FEC electrolyte preferentially underwent reductive decomposition and reduced the decomposition extent of TTE. FEC, with a relatively low adsorption energy and LUMO energy level, preferentially adsorbed on the Li metal and readily undergoes the reductive decomposition during initial Li plating. We surmised that the formed +1e-FEC anchored on the Li metal kinetically prevents the electron transfer from Li metal anode to TTE and thus the reduction of TTE occurs moderately. The complementary electrolyte design utilizing both TTE and FEC constructs a more favorable solid electrolyte interphase (SEI) for Li metal anodes.

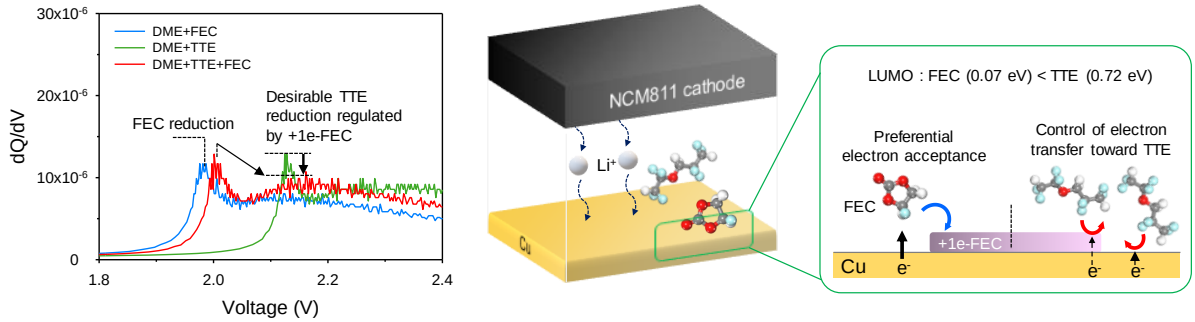

Fig. 4.6 dQ/dV curves of Cu|NCM811 cells in DME+FEC, DME+TTE and DME+TTE+FEC electrolyte at 0.05 mA cm^{-2}. Schematic showing the effect of FEC regulating the decomposition of TTE

Unique feature of TTE building the LiF-containing film on Li metal electrode was evidenced by a comparison of time of flight secondary ion mass spectrometry (TOF-SIMS) images of Li metal electrodes contacting TTE and FEC for 24 h at 25 °C (Figs. 4.7a and b). The maximum intensity of secondary ions is displayed in white in a color scale bar. The intensity associated with LiF was negligible for the Li electrode surface contacting FEC, as shown in TOF-SIMS LiF^- ion map of Fig. 4.7a. FEC hardly undergoes the defluorination of C–F bond when contacted the Li metal. The electron and Li^+ from Li metal triggers ring opening FEC and a soluble radical containing Li^+ ion and C–F bond seems to be produced with concomitant decrease in LiF formation (Fig. 4.7c). Clearly, FEC, which is considered the most effective additive to generate LiF as SEI constituent during electrochemical cycling, does not actively form LiF on Li metal without electric field. In constrast, a marked change in LiF^- ion map of Li metal surface contacting TTE appeared (Fig. 4.7b). Electropositive Li triggered the cleavage of C–F bonds in TTE and the released F^- combined with Li^+ to produce LiF progressively on Li metal electrode (Fig. 4.7d). It is thought that electrochemically stable LiF plays an critical role on manipulation of the Li metal-electrolyte interface to enhance the Li metal battery performance because F^- of LiF tends to attract Li ions in the SEI and thus mechanical integrity of the SEI may be preserved well under severe volumetric stress induced by Li plating and stripping.[90] Obviously, the reductive decomposition of FEC occurs through transition states of TS1 and TS2 with energy barriers that must be overcome, to form LiF via defluorination reaction (Fig. 4.7e). On contrary, density functional theory (DFT) calculations clearly showed that there is no energy barrier for the defluorination of TTE to produce LiF. Since TTE of type 1 with the lowest adsorption energy has lower LUMO than that of bare TTE (Fig. 4.5c and d), it is rational that TTE adsorbed on Li metal is prone to the reductive decomposition to form LiF and F-containing polymer species displayed in Fig. 4.7d.

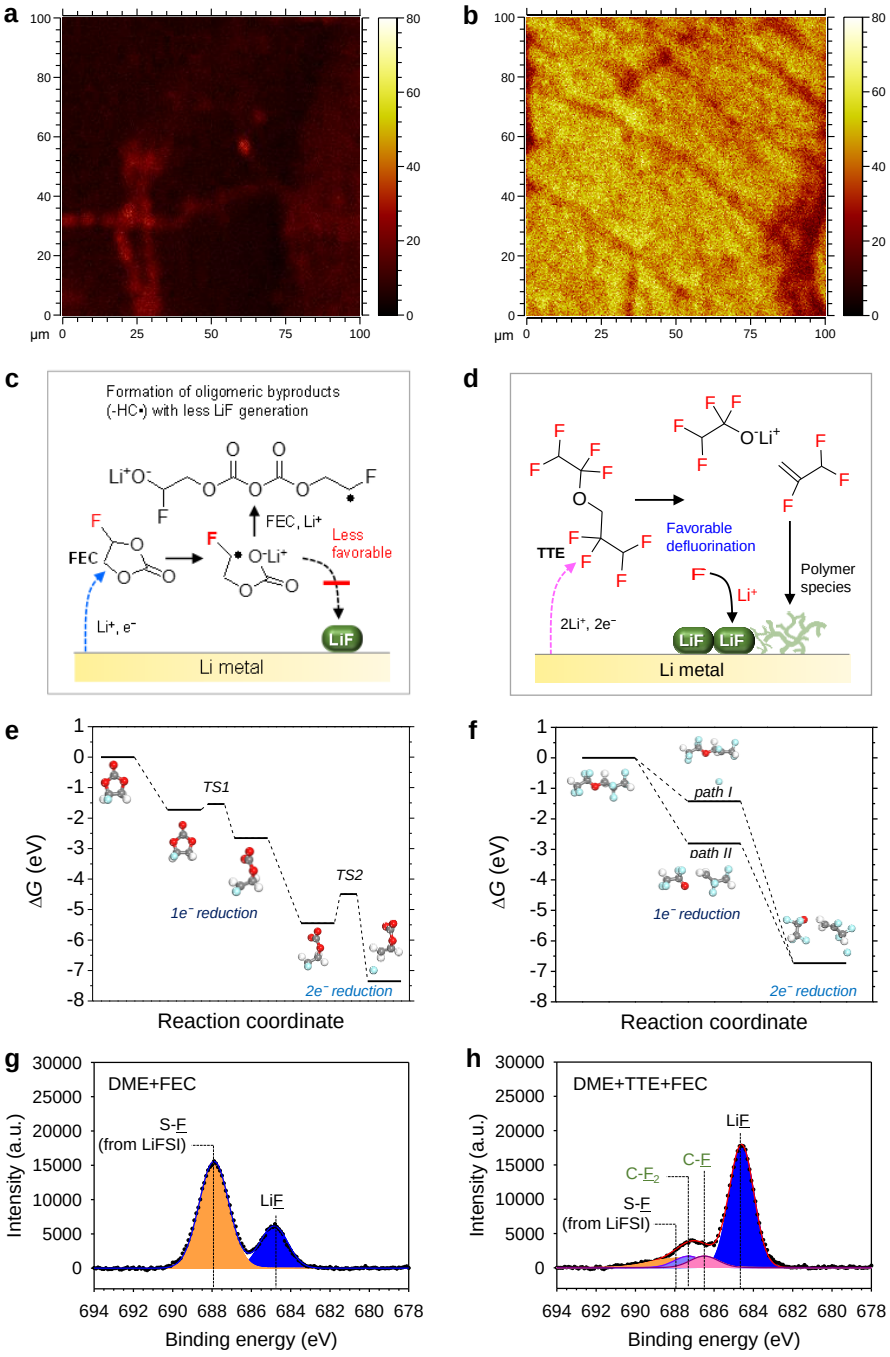

Fig. 4.7 TOF-SIMS LiF^- ion maps of Li metal contacting (a) neat FEC and (b) neat TTE at 25 °C for 1 day. Schematic illustration of decomposition of (c) FEC and (d) TTE on Li metal anode. Relative Gibbs free energy (ΔG) diagram for the reduction of (e) FEC and (f) TTE molecules. Gray, white, red and cyan spheres denote C, H, O and F atoms, respectively. F 1s XPS spectra of Li metal in Li/NCM cell with (g) DME+FEC electrolyte and (h) DME+TTE+FEC electrolyte after precycle at a rate of 0.1C.

Insight on the difference between surface chemistries electrochemically induced by TTE and FEC is given by ex situ X-ray photoelectron spectroscopy (XPS) measurements of the Li metal anodes retrieved from the Li|NCM811 cells after pre-cycling. The F 1s spectra of Li metal precycled in DME+FEC electrolyte reveals that relative fraction of S–F containing intermediates, which are formed by LiFSI salt decomposition, is higher than that of LiF (Fig. 4.7g). This implies that 1% FEC is insufficient to prevent salt decomposition at the Li metal. Unlike DME+FEC electrolyte exhibiting only two peaks at 684.7 and 687.8 eV, four types of fluorine appeared for the SEI on the Li metal precycled in DME+TTE+FEC electrolyte: fluorine bonded to sulfur (S–F) at 687.9 eV, fluorine of CF_2 at 687.3 eV, fluorine of CF at 686.5 eV, and LiF at 684.7 eV (Fig. 4.7h). Two additional peaks corresponding to CF and CF_2 that were not observed for DME+FEC electrolyte are attributable to F-containing polymer species formed by the reductive decomposition of TTE at the Li metal. In particular, the addition of TTE significantly reduced the peak intensity assigned to S–F bond, which is generated by the LiFSI decomposition, and led to the increment of relative fraction of LiF in the SEI on the Li metal (Fig. 4.7h). These findings unveil that TTE is reduced fast enough to construct SEI covering the Li metal and alleviate salt reduction during pre-cycling and that the TTE-derived SEI mostly consists of LiF, and a small amount of F-containing polymer species. Cycling test of Li|Cu cells and spectral study of Li metal surface manifest that LiF is a key SEI component for the improvement of electrochemical reversibility of Li metal. On basis of the calculation of adsorption energy on Li(001) surface, it is obvious that FEC favorably adsorbs on Li metal, preferentially reduces during initial Li plating, and regulates the reduction of TTE desirably. The ability of TTE forming LiF under electric field is revealed by a comparison of normalized counts of LiF^- ions recorded by TOF-SIMS of Li metal anodes after precycling (Fig. 4.8). Compared with DME+FEC, DME+TTE electrolyte showed greatly increased counts of LiF^- ions indicating high ability of TTE forming LiF. Though LiFSI and FEC induce LiF as a SEI component, the generated LiF did not achieve a uniform full coverage of Li metal anode. Importantly, use of TTE that can aggressively construct LiF on Li metal led to the uniform distribution of LiF on the electrode, which was not attained. TTE possessing F elements that serves as a lithiophilic site leads to the buildup of LiF-based SEI on Li metal. Moreover, planar FEC accets electron from the Li metal to transform into non-planar FEC. Non-planar FEC could donate electron to +1e-TTE, resulting in +1e-TTE reduction or could accept electron from Li metal to form SEI layer on Li metal regulating the further decomposition of TTE. Damaged SEI induced by Li plating accompanying large volume expansion can be mended because F elements of TTE molecule attracts Li^+ from the Li metal to produce LiF upon repeated cycling (Fig. 4.9).

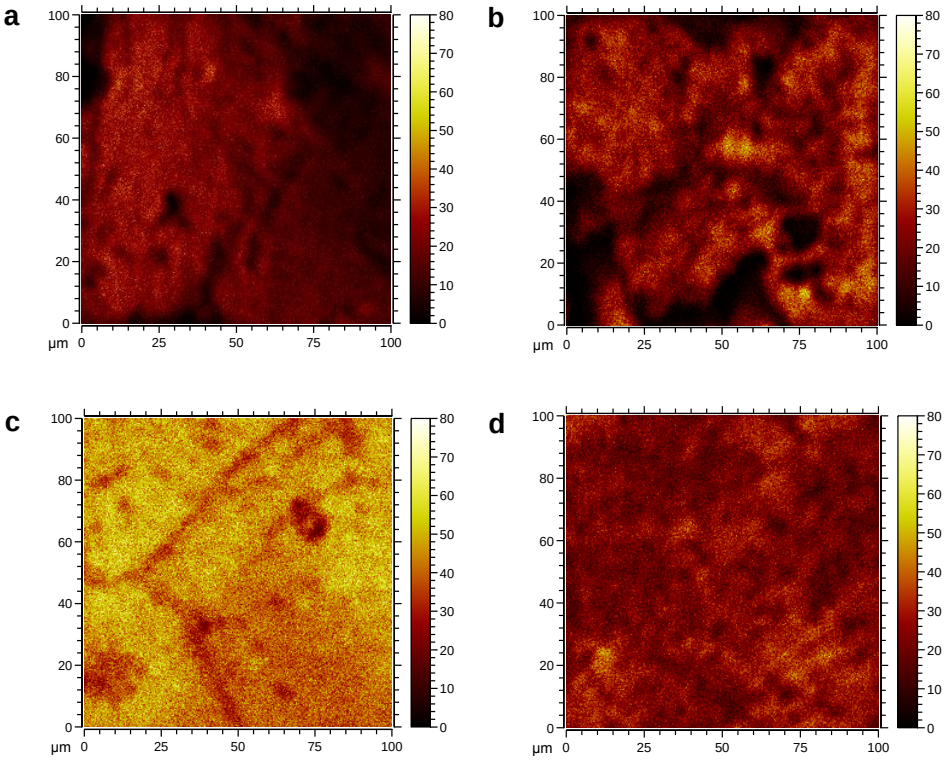

Fig. 4.8 TOF-SIMS LiF^- ion maps of Li metal anodes retrieved from Li|NCM811 full cells precycled in (a) DME, (b) DME+FEC, (c) DME+TTE, (d) DME+TTE+FEC using at a 0.1C rate and 25 °C.

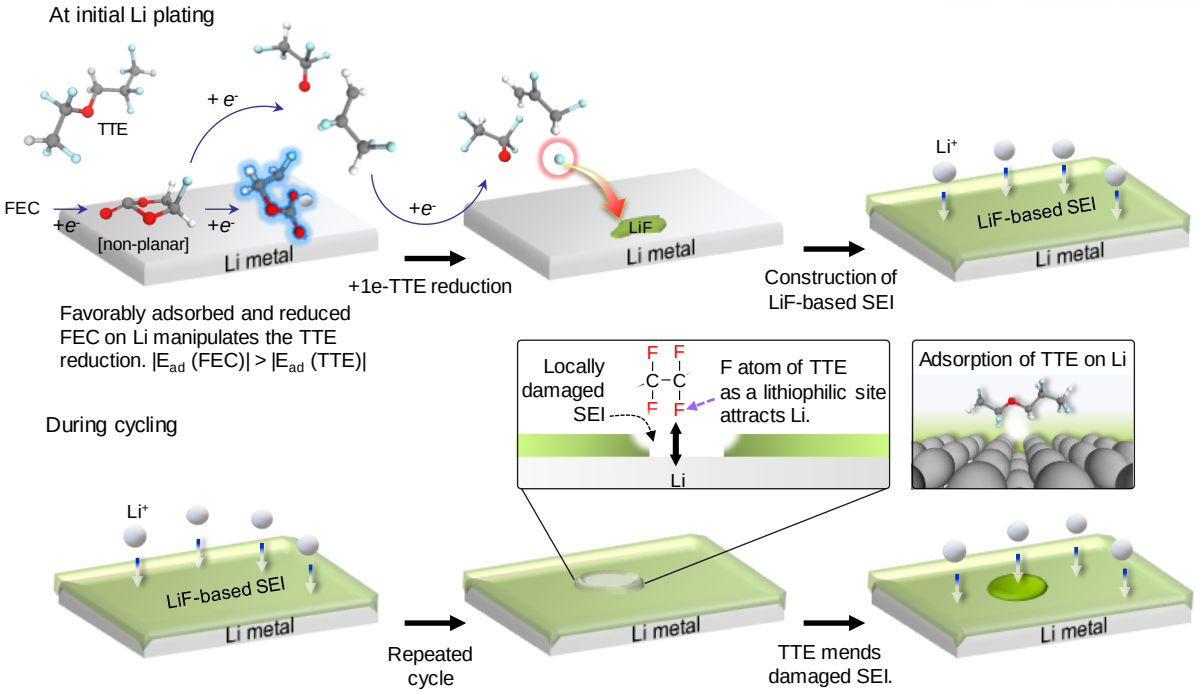

Fig. 4.9 Scheme showing the unique feature of TTE constructing SEI on Li metal at initial Li plating and repairing damaged SEI during cycling. FEC, which favorably adsorbed on the Li metal thanks to its low adsorption energy, tunes the reductive decomposition of TTE on the Li metal.

Fig. 4.10 shows the surface and cross-section scanning electron microscopy (SEM) images of Li metal electrochemically plated on a Cu substrate in a coin cell with confined space. Li deposits had non-uniform shape and various sizes on a Cu substrate with DME electrolyte, leaving much space between fibrous Li deposits. This less-densely grown Li layer displayed the thickness of 34 μm that is far thicker compared with theoretical thickness (10 μm) of Li metal producing with the areal capacity of 2 mAh cm^{-2} (Fig. 4.10e). Considering extremely low reversibility of 20.4% for initial Li plating and strpping reaction in DME electrolyte shown in Fig. 4.3a, this thick layer contains not only Li metal deposits of 6.9 μm but also large amount of byproducts of 27.1 μm induced by DME electrolyte decomposition during initial Li plating (Table 4.1). Contrary to the porous surface structure of deposited Li in DME electrolyte, surface morphological characteristics reveals that use of FEC led to the creation of more densely deposited Li on the Cu substrate (Fig. 4.10b). Further, chuncky fibrous Li deposits were tightly packed in DME+FEC electrolyte with a relatively thin layer of 18 μm (Fig. 4.10f). This result suggests the FEC effectively formed a dersirable SEI that act as an electron barrier between the electrolyte and Li deposits. Moreover, it restrains the irreversible electrolyte decomposition that would otherwise consume Li^+ and electrons during initial Li plating, substantially reducing the amount of byproducts embedded in the SEI layer. The initial CE of DME+FEC electrolyte is 78.3%, and the thicknesses of Li and SEI are 14.1 and 3.9 μm, respectively (Table 4.1). The SEI layer formed on the Li metal anode in DME+FEC electrolyte is thin relative to that with only DME. Similar sized chunky fibrous Li deposits are observed with DME+TTE+FEC electrolyte, as well as a denser structure of Li deposits packed in a thin layer of approximately 10 μm, which is close to the theoretical thickness (Fig. 4.10g). As evident from the drastically improved reversibility of 89.1% for Li plating and stripping (Fig. 4.3a and Table 4.1), the positive role of TTE on the alleviation of considerable reductive decomposition of DME+FEC led to the creation of thin and uniform Li deposits of 8.9 μm with 1.1 μm thick SEI. Very porous and dendritic Li deposits appear with the Carbonate+FEC electrolyte (Figs. 4.10d and h), which clearly show that 1 wt% FEC cannot render uniform Li plating in a conventional carbonate-based electrolyte.

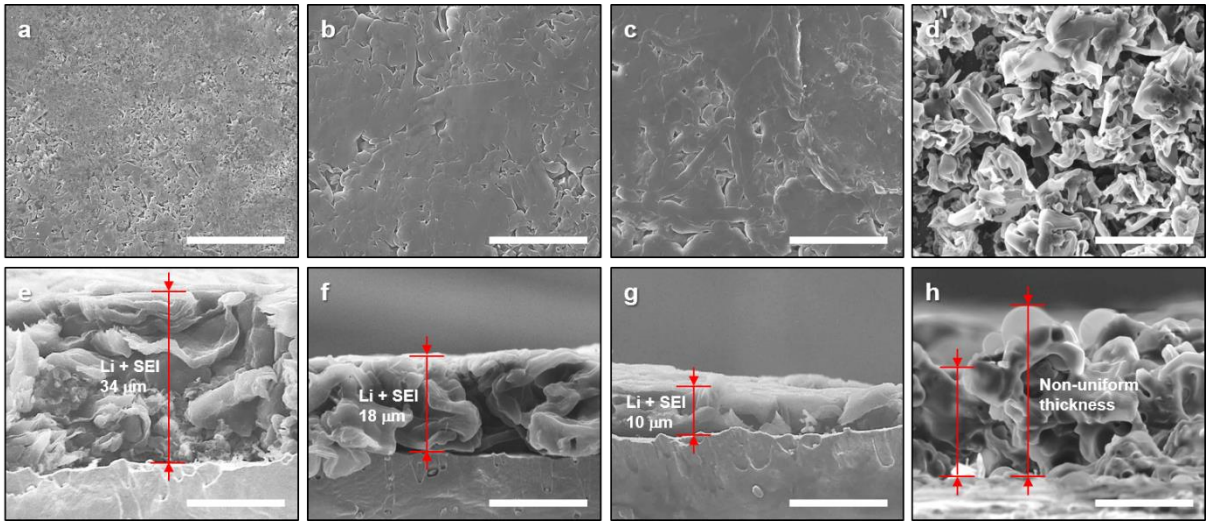

Fig. 4.10 SEM images of Li deposits on Cu substrate in (a, e) DME, (b, f) DME+FEC, (c, g) DME+TTE+FEC and (d, h) Carbonate+FEC electrolyte at a current density of 0.2 mA cm^{-2}. (a, b, c, d : top-view, e, f, g, h : side-view) The areal capacity utilized from the counter Li metal electrode was 2 mAh cm^{-2}. Scale bars in (a-d) and (e-h) are 50 μm and 20 μm, respectively.

Table 4.1 Theoretical thicknesses of Li and SEI (μm) on Cu substrate based on initial Coulombic efficiency (ICE) of Li plating and stripping in Li/Cu cell

Electrolyte	ICE	Li	SEI
DME	20.4%	6.9	27.1
DME+FEC	78.3%	14.1	3.9
DME+TTE+FEC	89.1%	8.9	1.1

The compatibility of the electrolytes toward the Li metal anode and NCM811 cathode was explored using Li|NCM811 coin cells. Comparing previous reports performing the evaluation of cycle performance of Li|NCM811 with thick Li metal anode more than 250 μm to compensate the loss of Li source during cycle in Li|NCM811 cells, use of quantitatively limited Li metal anode with thickness of 100 μm in cell tests is considered more rational approach to find practicable electrolytes for high-energy density Li metal batteries. Although ethers are the most suitable solvents toward Li metal anodes, ethers such as DME have been excluded from batteries with 4 V-class cathodes, due to their low upper voltage limit of <4 V *vs*. Li/Li^+. Surprisingly, Li/NCM811 cell with DME-based electrolytes formulated by the combination of TTE and FEC (DME+TTE+FEC electrolyte) delivered relatively higher discharge capacity of 197.4 mAh g^{-1} with improved ICE of 90% and exhibited significantly reduced overpotential during initial charge process at pre-cycling compared with Li|NCM811 cells containing other electrolytes (Figs. 4.11a and 4.12a). This surpasses the discharge capacity of 190.3 mAh g^{-1} and ICE of 89.6% achieved with Carbonate+FEC, which has been employed in most commercial Li-ion batteries. The reduced overpotential at the beginning of charge at the pre-cycling can be explained by the penetration of the electrolyte into the interior vacancies of the NCM811 cathode to allow facile Li deintercalation from the cathode and the nature of the interfacial layer formed on the Li metal anode affecting charge transport through it. The wettability of the concentrated DME electrolyte toward the NCM811 cathode and hydrophobic polyethylene separator is significantly enhanced by using TTE as co-solvent (Fig. 4.12b). This TTE-induced affinity is thought to improve the accessibility of the electrolyte to the NCM811 cathode particles, facilitate the electrochemical activation of the cathode, and assist the reduction of ohmic polarization of a Li|NCM811 cell. However, the addition of only FEC to DME causes a large overpotential at the beginning of charge at the pre-cycling, resulting in the lowest discharge capacity and ICE. The large overpotential is mostly associated with the activation of the passivated Li metal anode, as well as the kinetics of Li ion deintercalation from the NCM811 cathode. We surmised that FEC generates a resistive interfacial layer that impedes charge transport at the Li metal anode and NCM811 cathode and inhibits the activation of both electrodes. The synergistic effects of FEC and TTE on the electrochemical properties of a Li|NCM811 cell clearly emerge from the galvanostatic cycling of a full cell constructed with a Li metal anode and NCM811 cathode at 0.5C rate and 25 °C (Fig. 4.11b). The substantial reduction of voltage hysteresis during charge and discharge in a Li|NCM811 full cell at 90^{th} cycle is attributed to interfacial stabilization ability of the TTE-oriented SEI on the Li metal anode and the FEC-promoted CEI on the NCM811 cathode (Fig. 4.12c).

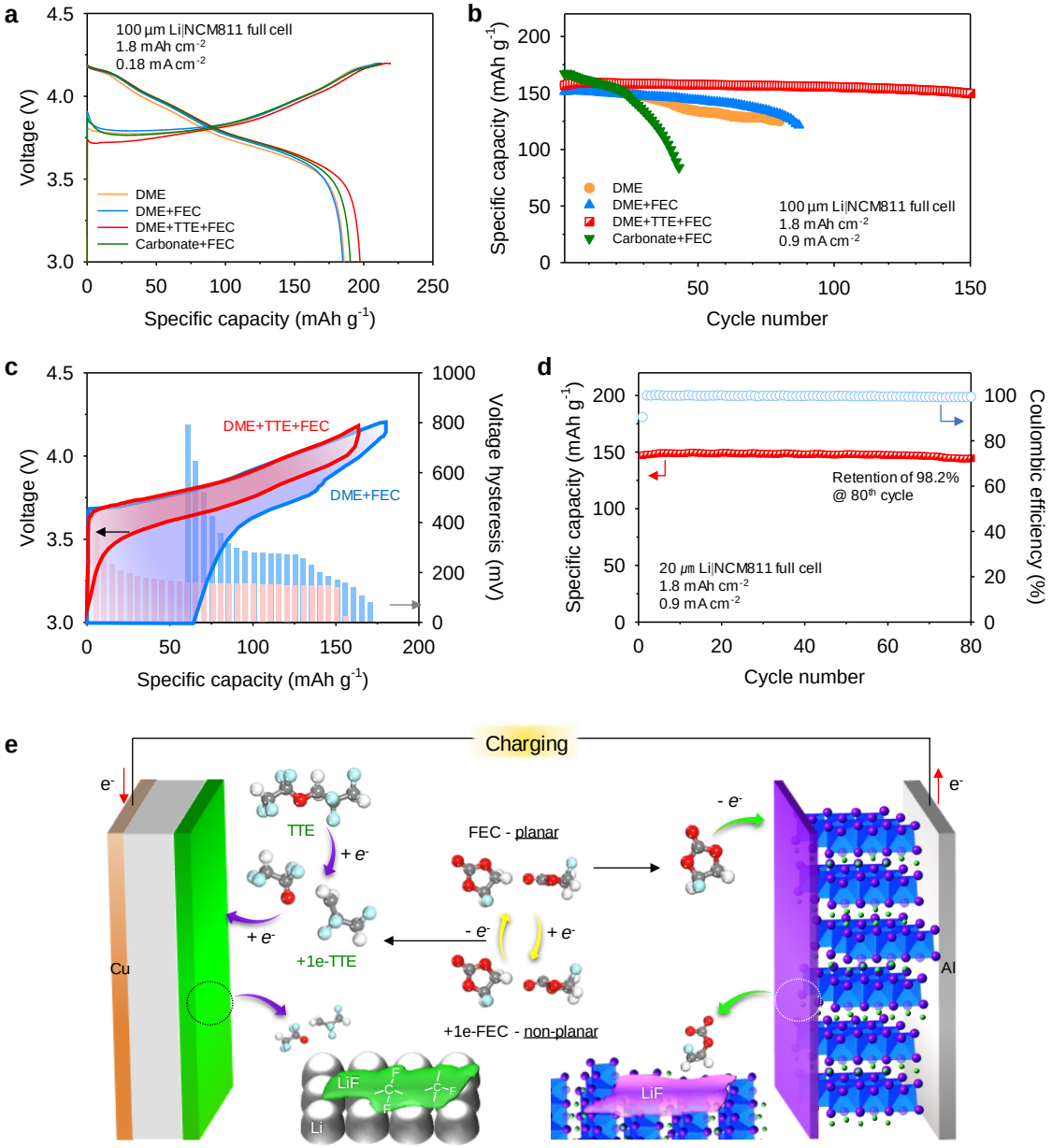

Fig. 4.11 Electrochemical performance of Li|NCM811 full cells. (a) Voltage profiles during pre-cycling at a 0.1C rate and 25 °C. (b) Specific discharge capacity of Li|NCM811 full cells at a 0.5C rate and 25 °C. Foil-type Li metal with thickness of 100 µm was employed as an anode. (c) Voltage profile and hysteresis of charge and discharge at 90th cycle. (d) Specific discharge capacity and Coulombic efficiency of Li|NCM811 full cells with 20 µm Li metal anode in DME+TTE+ FEC electrolyte at a 0.5C rate and 25 °C. (e) Interfacial engineering function of TTE and FEC protecting electrode interfaces in Li|NCM811 full cells.

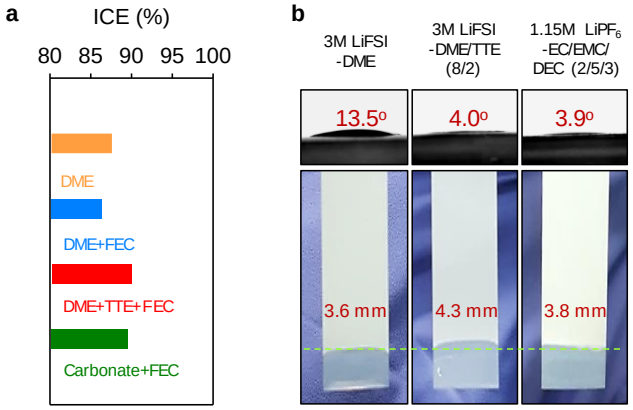

Fig. 4.12 Electrochemical performance of Li|NCM811 cell in precycle and wetting property of electrolytes toward the NCM811 cathodes and separators. (a) Initial Coulombic efficiency of Li|NCM811 full cells at a 0.1C rate and 25 °C. (b) Contact angle of the electrolyte on the NCM811 cathode and photographs of the separators after there one side were immersed in the electrolytes for 2 min.

Clearly, carbonate+FEC electrolyte, which has been commonly employed in most of commercial Li-ion batteries, caused rapid capacity fading of the cell delivering a low CE of below 95% (Fig. 4.13). Commercially available carbonate-based electrolytes cannot preserve electrochemical reversibility of Li metal batteries despite the use of FEC additive. On the other hand, the discharge capacity retention of the Li/NCM811 full cell with a high CE of over 99.8% was significantly enhanced with DME+TTE+FEC electrolyte over 150 cycles. Although concentrated DME electrolytes that are more compatible with Li metal anode showed more extended cycling stability within short cycles than carbonate-based electrolytes, continuous decay of CE occurred upon repeated cycling and cell operation suddenly stopped by abnormal charge-discharge cycling after 80^{th} cycle.

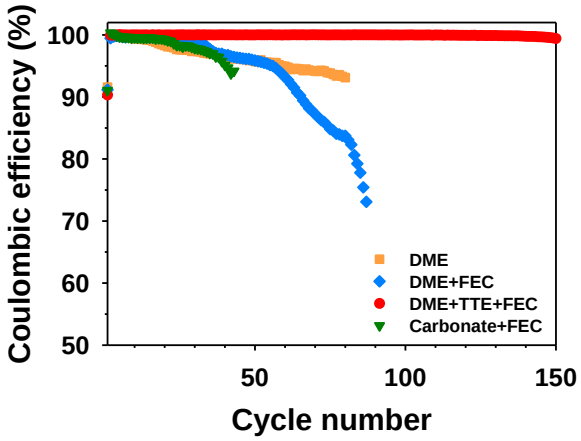

Fig. 4.13 Coulombic efficiency of Li/NCM cells at a rate of 0.5C and 25 °C.

More extended cycle life is attributable to high concentration of LiFSI that improves the interfacial stablilization of Li metal due to minimal free DME.[7] Indeed, unlike 3M LiFSI-DME+TTE+FEC, Li|NCM811 full cells with less concentrated electrolytes (1M or 2M LiFSI-DME+TTE+FEC) exhibited severe capacity decay delivering continuously decreased CE and the cell operation was terminated within 60 cycles (Fig. 4.14). Because free (uncoordinated) DME as a relatively strong Lewis base, readily loses its oxygen lone pair electrons, oxidation stability of the electrolyte at the NCM811 cathode is difficult to achieve in dilute electrolytes. Further evidence is presented in linear sweep voltammetry measuring the oxidation behavior of electrolytes on a stainless steel (SS) electrode. Compared with 1M and 2M LiFSI-containing electrolytes, DME+TTE+FEC with 3M LiFSI had better oxidation durability (Fig. 4.15). However, more concentrated DME+TTE+FEC electrolytes from 3M to 4M shortened the lifetime of Li/NCM811 cell (Fig. 4.16). This is probably because sluggish transport of Li ions in viscous electrolyte causes large ohmic resistance and badly affects the migration of Li ions into the SEI on Li metal and the CEI on the Ni-rich cathode. Indeed, much larger ohmic polarization appeared for 3.5M and 4M salt concentration unpon repeated cycling (Fig. 4.17).

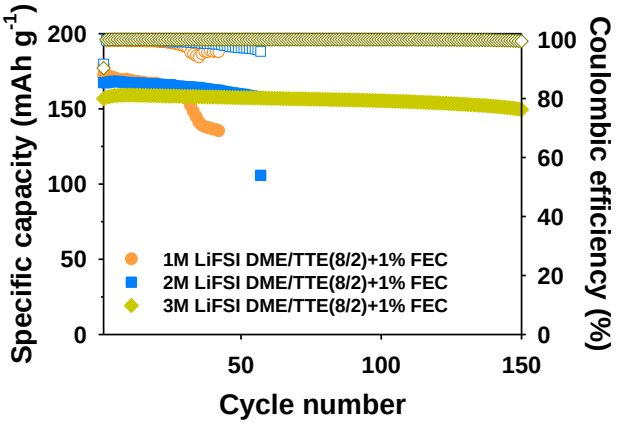

Fig. 4.14 Specific discharge capacity and Coulombic efficiency of Li/NCM cells at a rate of 0.5C and 25 °C.

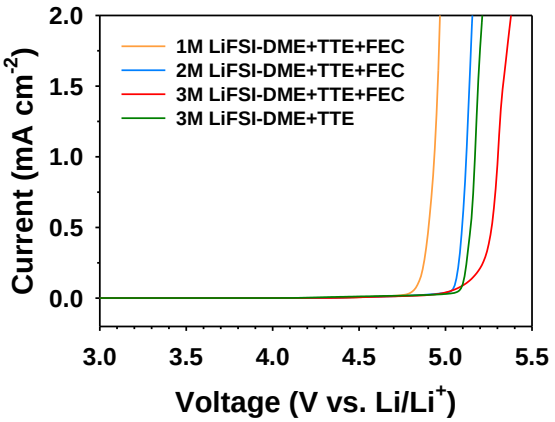

Fig. 4.15 Anodic stability of electrolytes on an SS working electrode at a scan rate of 1 mV s^{-1}.

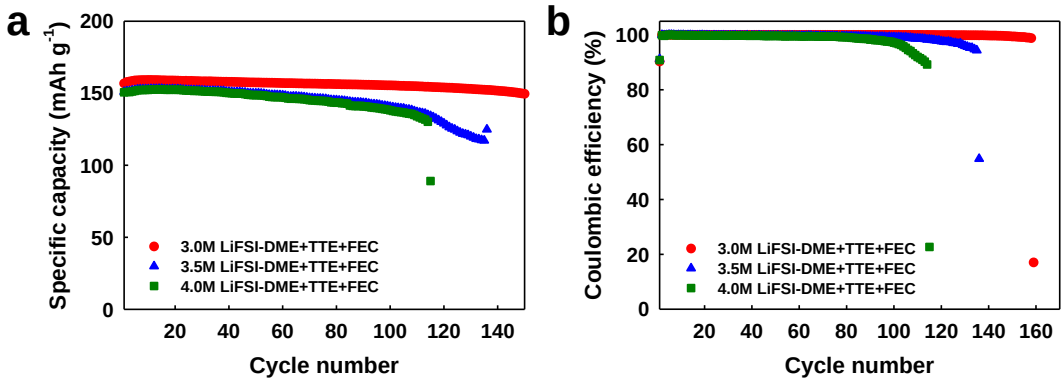

Fig. 4.16 (a) Specific discharge capacity and (b) Coulombic efficiency of Li/NCM cells at a rate of 0.1C and 25 °C.

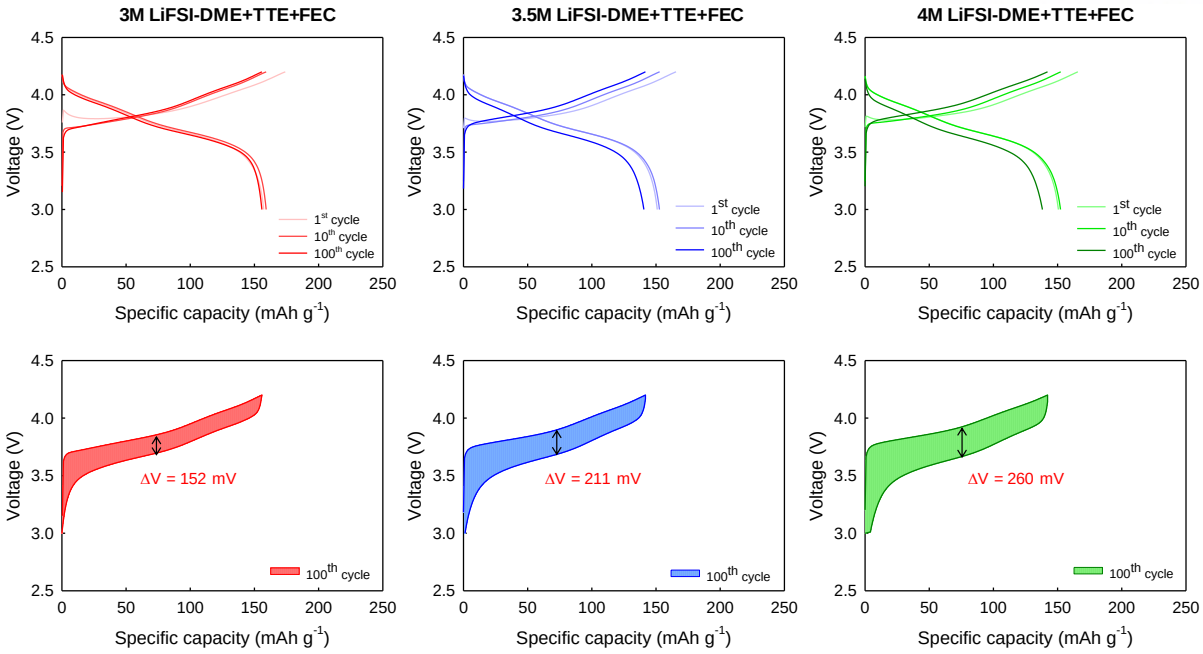

Fig. 4.17 Charge-discharge voltage profiles (top) and enlarged voltage profiles (bottom) of Li/NCM cells at 1st, 10th and 100th cycle.

Our investigation reveals that optimal salt concentration in DME+TTE+FEC for Li|NCM811 cells is 3M LiFSI. The incorporation of FEC in concentrated DME electrolytes did not inihibit unwanted electrolyte decomposition that increases cell resistance and more severe capacity fading appeared. Free DME molecules, which does not coordinate with Li^+ in the electrolyte, access the cathode surface to solvate Li^+ extracted from the NCM811 cathode during charge process and the decomposition probability of DME directly containing highly oxidized NCM811 cathode is expected to be high. Obviously, this unavoidable circumstance leads to continued DME decomposition with reactive species such as active radicals that may trigger undesirable salt decomposition, indicating depletion of the limited electrolyte in a cell. To verify the beneficial effect of FEC on the interfacial stability of NCM811 cathode, anodic stability of the FEC-added electrolyte, the leakage current of the Li|NCM811 cells was monitored at a constant charging voltage of 4.2 V during 11^{th} charge process after 10 cycles. The Li|NCM811 cell with DME electrolyte showed a relatively larger leakage current indicating increased oxidative decomposition of the electrolyte at the NCM811 cathode, while the addition of FEC led to the reduction in the leakage current (Fig. 4.18). This result confirms that FEC forms the interfacial layer that helps the DME-based electrolyte tolerate the high voltage of 4.2 V.

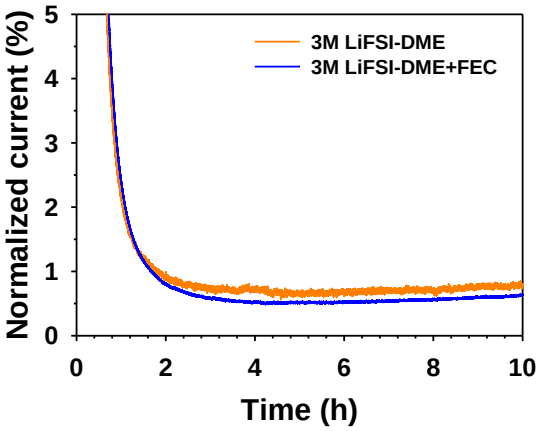

Fig. 4.18 Potentiostatic profiles of Li/NCM cells at a constant voltage of 4.2V during 11th charge process after 10 cycles at a rate of 0.5C.

The unique feature of FEC-derived CEI on NCM811 cathode is observed in the cross-sectional SEM images of the NCM811 cathodes retrieved from the Li|NCM811 cells (Fig. 4.19). Before cycling, secondary NCM811 particles composed of primary particles exhibited microcracks owing to roll pressing, providing an appropriate electronic conduction network of the NCM811 cathode (Fig. 4.19a). The NCM cathode retreived from the Li/NCM811 cell cycled in the DME electrolyte during 20 cycles showed a lot of integranular cracks and its thickness severely increased from 32 μm to ca. 43 μm compared with non-cycled cathode (Fig. 4.19c and d). The CEI induced by DME produces a heterogenous Li ion flux and lithiation/delithiation reactions from the NCM811 cathode. Anisotropic strain changes caused by heterogeneous lithiation/delithiation provoke the fragmentation of NCM811 secondary particles and augment the probability of further electrolyte decomposition and the resulting accumulation of resistive byproducts in the NCM811 secondary particles (Fig. 4.19i). On contrary, the NCM811 cathodes retrived from Li|NCM811 cell cycled in DME+FEC and DME+TTE+FEC electrolyte for 20 cycles exhibit relatively well-preserved morphology of NCM811 secondary particles without severe thickness change and intergranular cracking (Figs. 4.19e, f, g, and h). It is obvious that FEC plays an important role on preservation of mechanical integrity of the NCM811 cathode in DME-based electrolytes. The addition of FEC to DME+TTE constructs uniform and stable CEI on the NCM811 cathode in a Li|NCM811 cell, allowing homogenous reaction of lithiation/delithiation across the cathode and alleviating electrolyte decomposition at the cathode (Fig. 4.19j). Although DME+FEC has a positive impact on the inhibition of the degradation of the NCM811 cathode, it is not suitable for a Li|NCM811 cell because it does not form a stable SEI on the Li metal anode, which leads to the poor cycling performance of the Li|Cu cell (Fig. 4.3e).

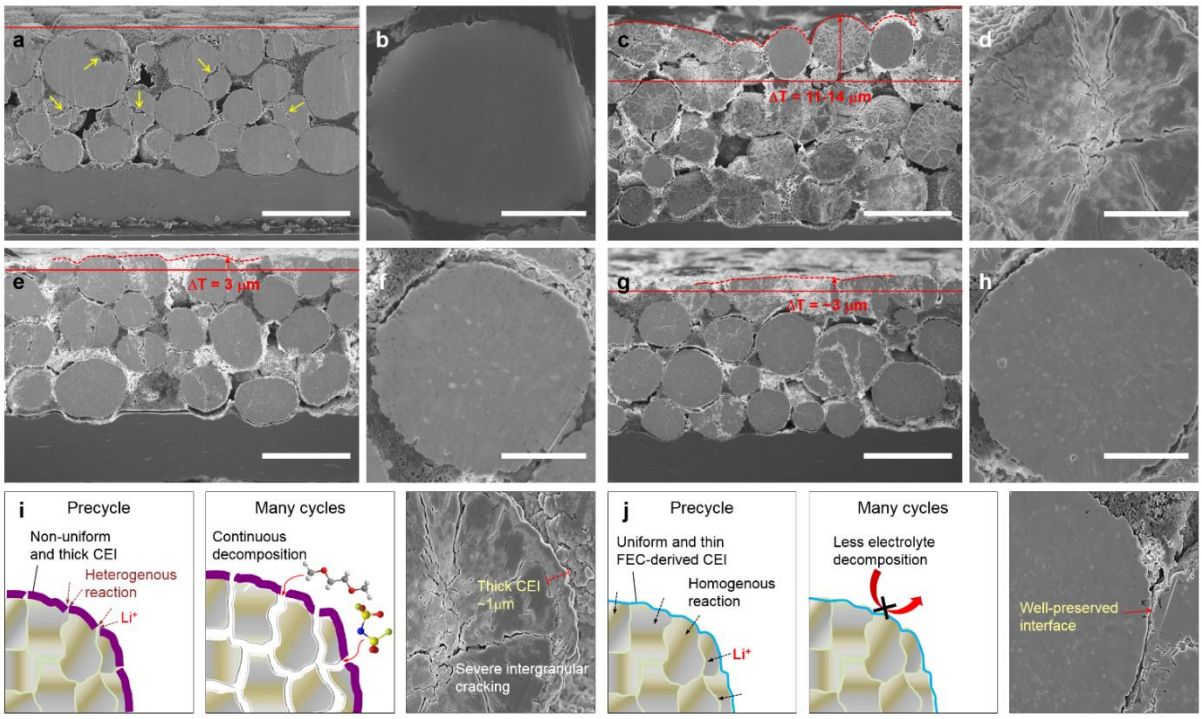

Fig. 4.19 Cross-sectional SEM images of NCM811 cathode. (a, b) pristine NCM811 cathode. Cycled NCM811 cathodes retrieved from Li|NCM811 cells with (c, d) DME, (e, f) DME+FEC, and (g, h) DME+TTE+FEC electrolyte after 20 cycles at a 0.5C rate and 25 °C. ΔT is the change in thickness of the NCM811 cathodes after cycling. Yellow arrows indicate microcracking of secondary NCM811 particles induced by roll pressing process. Schematic illustration of (i) the interfacial degradation of the NCM811 cathode in DME electrolyte and (j) robust and uniform CEI constructed by TTE+FEC.

To identify the composition of FEC-derived CEI on NCM cathode, XPS measurements of the cathodes in the Li|NCM811 cells after precycle were performed (Fig. 4.20). The F 1s spectra of the cathodes precycled in the DME electrolyte reveal that S–F peak at 687.9 eV and LiF peak at 684.7 eV, mainly attributed to the decomposition of LiFSI. However, the intensity of the S–F peak at 688.1 eV decreases upon addition of FEC, mostly because the FEC-derived CEI inhibits the oxidative decomposition of LiFSI at the NCM811 cathode. The relative fraction of LiF in the CEI on NCM811 cathode was slightly increased from 18.9% to around 20% by the addition of 1% FEC (Figs. 4.20b and c). The FEC-promoted CEI alleviated the decompositon of LiFSI at the NCM811 cathode and allowed the homogenous lithiation and delithiation reaction of Li ion across the NCM811 cathode, resulting in preserving the morphology of NCM811 secondary particles without severe intergranular cracking (Figs. 4.19f and h). As a result, the enhanced cycling stability of the Li/NCM811 cell was attributed to (a) the promotional effect of TTE on the construction of a robust SEI shield accommodating the destructive stress induced by Li plating and stripping on the Li metal anode and (b) the increased electrochemical robustness of the Ni-rich cathode interface and the prevention of severe intergranular cracking of the above cathode by the use of FEC (Fig. 4.11e).

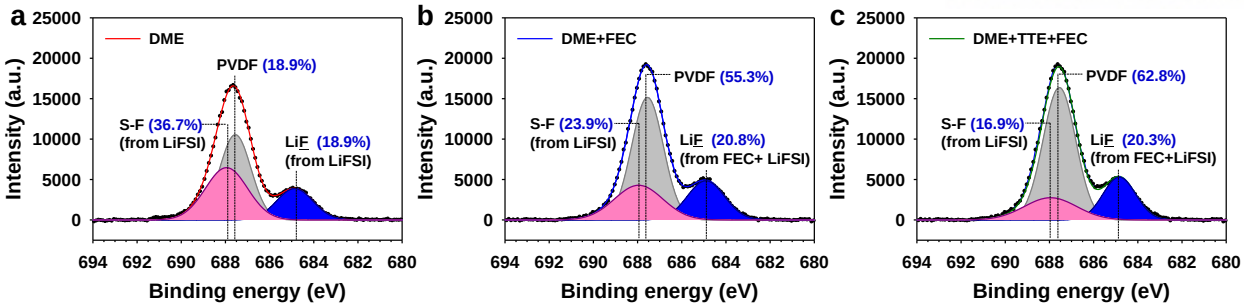

Fig. 4.20 F 1s XPS spectra of NCM cathode in Li/NCM cell with (a) DME electrolyte, (b) DME+FEC electrolyte and (c) DME+TTE+FEC electrolyte after precycle at a rate of 0.1C.

To further confirm the positive impact of DME+TTE+FEC electrolyte on NCM811 cathode performance, the interfacial stability of the NCM811 cathodes at 60 °C was explored (Fig. 4.21). Fully charged (de-lithiated) NCM811 cathodes with the CEI formed by $LiPF_6$-containing and LiFSI-containing electrolytes (DME+TTE+FEC) are stored in each electrolyte at 60 °C for 24 h (Fig. 14.21). Considerable dissolution of Co, Mn, and Ni from the cathode is observed for $LiPF_6$-containing electrolyte because the Brønsted acid HF, formed by hydrolysis of $LiPF_6$ in the electrolyte, leaches transition metal ions from the cathode. The dissolution of Co, Mn, and Ni from the cathode was drastically suppressed in the $LiPF_6$-free electrolyte, DME+TTE+FEC electrolyte. This indicates that the use of concentrated LiFSI electrolytes, which do not generate acidic species, can circumvent transition metal dissolution, a critical limitation of a Ni-rich cathode in $LiPF_6$-containing electrolytes at elevated temperatures (Fig. 4.21b).

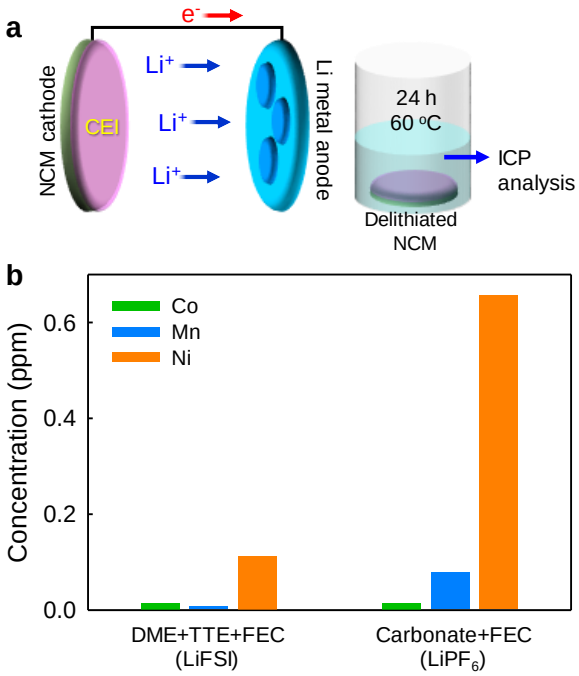

Fig. 4.21 Transition metal dissolution of NCM811 cathode. (a) Schematic of sample preparation procedure for ICP analysis. (b) Amounts of transition metal (Co, Mn and Ni) dissolved in the electrolyte storing with fully charged NCM811 cathode up to 4.2 V *vs.* Li/Li^+ at 60 °C for 24 h. (DM+FEC: 3M LiFSI-DME/TTE (8/2)+1% FEC, $LiPF_6$-based: 1.15M $LiPF_6$-EC/EMC/DEC (2/5/3))

The cycling performance of the Li|NCM811 cell with DME+TTE+FEC was explored using a much thinner Li metal anode with a thickness of 20 μm (corresponding to an areal capacity of 4 mAh cm^{-2}), which enables further improvement in the energy density of the battery compared with a battery using a 100 μm (corresponding to the areal capacity of 20 mAh cm^{-2}) Li metal (Fig. 4.11d). 20 μm Li|NCM811 cells containing DME+TTE+FEC electrolyte delivered discharge capacity of 144.6 mAh g^{-1} and excellent capacity retention of 98.2% with high CE of over 99.4% at 80th cycle. This is the first attempt for Li metal battery employing the Ni-rich cathode surpassing 60% of Ni content and 20 μm Li metal anode. DME+TTE+FEC electrolyte outperformed the cycling performance of Li|$LiNi_{0.5}Co_{0.2}Mn_{0.3}O_2$ (NCM523) cells with a 20 μm thick Li metal anode reported by the Choi's group.[91] Their electrolyte system (3M LiFSI-EC/DEC/toluene electrolyte) in Li|NCM523 cells with a 20 μm thick Li metal anode retained the discharge capacity of 81.6% after 80 cycles. We expect that the results of this study and the associated analysis will contribute to further improvement of the electrochemical performances of high-energy density Li metal batteries with extremely limited Li source.

4.4 Conclusion

We have demonstrated that the realization of high-energy-density Li metal batteries with 4 V-class cathodes necessitates the search for suitable electrolytes and techniques for the surface modification of Li metal anodes and cathodes. It was probed that interfacial engineering of electrodes *via* the formulation of TTE and FEC provides the benefit attaining enhanced cycling stability of full Li metal battery based on Li metal anode and NCM811 cathode. The use of TTE as co-solvent to ether-based electrolytes promoted the construction of an SEI that could effectively decentralize Li ions across the electrode surface without initiating dendritic Li formation and immoderate electrolyte decomposition in Li|Cu and Li|NCM811 cells. Markedly, the FEC-controlled formation of the NCM811 cathode-electrolyte interphase could alleviate the mechanical fracturing of NCM811 cathode particles due to anisotropic volume changes induced by inhomogeneous lithiation/de-lithiation reactions and prevent the oxidative decomposition of electrolytes and the concomitant generation of resistive by-products blocking Li ion transport at the cathode. The use of role-assigned solvents and additives avoiding possible electrolyte shortages is believed to expand the application scope of ether-based electrolytes, which have been ruled out for application to 4 V-class batteries because of their limited oxidation stability.

REFERENCES

1. Hong, S. Y.; Kim, Y.; Park, Y.; Choi, A.; Choi, N. S.; Lee, K. T., Charge carriers in rechargeable batteries: Na ions vs. Li ions. *Energy & Environmental Science* **2013,** *6* (7), 2067-2081.
2. Kim, S. W.; Seo, D. H.; Ma, X. H.; Ceder, G.; Kang, K., Electrode Materials for Rechargeable Sodium-Ion Batteries: Potential Alternatives to Current Lithium-Ion Batteries. *Advanced Energy Materials* **2012,** *2* (7), 710-721.
3. Palomares, V.; Serras, P.; Villaluenga, I.; Hueso, K. B.; Carretero-Gonzalez, J.; Rojo, T., Na-ion batteries, recent advances and present challenges to become low cost energy storage systems. *Energy & Environmental Science* **2012,** *5* (3), 5884-5901.
4. Hwang, T. H.; Jung, D. S.; Kim, J. S.; Kim, B. G.; Choi, J. W., One-Dimensional Carbon-Sulfur Composite Fibers for Na-S Rechargeable Batteries Operating at Room Temperature. *Nano Lett* **2013,** *13* (9), 4532-4538.
5. Xin, S.; Yin, Y. X.; Guo, Y. G.; Wan, L. J., A High-Energy Room-Temperature Sodium-Sulfur Battery. *Advanced Materials* **2014,** *26* (8), 1261-1265.
6. Hartmann, P.; Bender, C. L.; Vracar, M.; Durr, A. K.; Garsuch, A.; Janek, J.; Adelhelm, P., A rechargeable room-temperature sodium superoxide (NaO2) battery. *Nat Mater* **2013,** *12* (3), 228-232.
7. Komaba, S.; Ishikawa, T.; Yabuuchi, N.; Murata, W.; Ito, A.; Ohsawa, Y., Fluorinated Ethylene Carbonate as Electrolyte Additive for Rechargeable Na Batteries. *Acs Applied Materials & Interfaces* **2011,** *3* (11), 4165-4168.
8. Iermakova, D. I.; Dugas, R.; Palacin, M. R.; Ponrouch, A., On the Comparative Stability of Li and Na Metal Anode Interfaces in Conventional Alkyl Carbonate Electrolytes. *Journal of the Electrochemical Society* **2015,** *162* (13), A7060-A7066.
9. Rudola, A.; Aurbach, D.; Balaya, P., A new phenomenon in sodium batteries: Voltage step due to solvent interaction. *Electrochemistry Communications* **2014,** *46*, 56-59.
10. Seh, Z. W.; Sun, J.; Sun, Y. M.; Cui, Y., A Highly Reversible Room-Temperature Sodium Metal Anode. *Acs Central Science* **2015,** *1* (8), 449-455.
11. Yui, Y.; Hayashi, M.; Nakamura, J., In situ Microscopic Observation of Sodium Deposition/Dissolution on Sodium Electrode. *Scientific Reports* **2016,** *6*.
12. Jang, J. Y.; Kim, H.; Lee, Y.; Lee, K. T.; Kang, K.; Choi, N.-S., Cyclic carbonate based-electrolytes enhancing the electrochemical performance of Na4Fe3(PO4)2(P2O7) cathodes for sodium-ion batteries. *Electrochemistry Communications* **2014,** *44*, 74-77.
13. Cheng, X.-B.; Zhang, R.; Zhao, C.-Z.; Zhang, Q., Toward Safe Lithium Metal Anode in Rechargeable Batteries: A Review. *Chemical Reviews* **2017,** *117* (15), 10403-10473.
14. Xu, W.; Wang, J. L.; Ding, F.; Chen, X. L.; Nasybutin, E.; Zhang, Y. H.; Zhang, J. G., Lithium metal anodes for rechargeable batteries. *Energy & Environmental Science* **2014,** *7* (2), 513-537.
15. Bai, P.; Li, J.; Brushett, F. R.; Bazant, M. Z., Transition of lithium growth mechanisms in liquid electrolytes. *Energy & Environmental Science* **2016,** *9* (10), 3221-3229.
16. Wan, G.; Guo, F.; Li, H.; Cao, Y.; Ai, X.; Qian, J.; Li, Y.; Yang, H., Suppression of Dendritic Lithium Growth by in Situ Formation of a Chemically Stable and Mechanically Strong Solid Electrolyte Interphase. *ACS Applied Materials & Interfaces* **2018,** *10* (1), 593-601.
17. Wu, B. B.; Lochala, J.; Taverne, T.; Xiao, J., The interplay between solid electrolyte interface (SEI) and dendritic lithium growth. *Nano Energy* **2017,** *40*, 34-41.
18. Liu, K.; Pei, A.; Lee, H. R.; Kong, B.; Liu, N.; Lin, D. C.; Liu, Y. Y.; Liu, C.; Hsu, P. C.; Bao, Z. A.; Cui, Y., Lithium Metal Anodes with an Adaptive "Solid-Liquid" Interfacial Protective Layer. *Journal of the American Chemical Society* **2017,** *139* (13), 4815-4820.
19. Heine, J.; Hilbig, P.; Qi, X.; Niehoff, P.; Winter, M.; Bieker, P., Fluoroethylene Carbonate as Electrolyte Additive in Tetraethylene Glycol Dimethyl Ether Based Electrolytes for Application in Lithium Ion and Lithium Metal Batteries. *Journal of The Electrochemical Society* **2015,** *162* (6), A1094-A1101.

20. Markevich, E.; Salitra, G.; Chesneau, F.; Schmidt, M.; Aurbach, D., Very Stable Lithium Metal Stripping-Plating at a High Rate and High Areal Capacity in Fluoroethylene Carbonate-Based Organic Electrolyte Solution. *Acs Energy Letters* **2017,** *2* (6), 1321-1326.
21. Zhang, X.-Q.; Cheng, X.-B.; Chen, X.; Yan, C.; Zhang, Q., Fluoroethylene Carbonate Additives to Render Uniform Li Deposits in Lithium Metal Batteries. *Adv Funct Mater* **2017,** *27* (10), 1605989.
22. Song, J.-H.; Yeon, J.-T.; Jang, J.-Y.; Han, J.-G.; Lee, S.-M.; Choi, N.-S., Effect of Fluoroethylene Carbonate on Electrochemical Performances of Lithium Electrodes and Lithium-Sulfur Batteries. *Journal of The Electrochemical Society* **2013,** *160* (6), A873-A881.
23. Qian, J. F.; Henderson, W. A.; Xu, W.; Bhattacharya, P.; Engelhard, M.; Borodin, O.; Zhang, J. G., High rate and stable cycling of lithium metal anode. *Nature Communications* **2015,** *6*.
24. Xu, K., Nonaqueous Liquid Electrolytes for Lithium-Based Rechargeable Batteries. *Chemical Reviews* **2004,** *104* (10), 4303-4418.
25. Chen, S.; Zheng, J.; Mei, D.; Han, K. S.; Engelhard, M. H.; Zhao, W.; Xu, W.; Liu, J.; Zhang, J.-G., High-Voltage Lithium-Metal Batteries Enabled by Localized High-Concentration Electrolytes. *Advanced Materials* **2018,** *30* (21), 1706102.
26. Lee, J.; Lee, Y.; Lee, J.; Lee, S.-M.; Choi, J.-H.; Kim, H.; Kwon, M.-S.; Kang, K.; Lee, K. T.; Choi, N.-S., Ultraconcentrated Sodium Bis(fluorosulfonyl)imide-Based Electrolytes for High-Performance Sodium Metal Batteries. *ACS Applied Materials & Interfaces* **2017,** *9* (4), 3723-3732.
27. Yamada, Y.; Furukawa, K.; Sodeyama, K.; Kikuchi, K.; Yaegashi, M.; Tateyama, Y.; Yamada, A., Unusual Stability of Acetonitrile-Based Superconcentrated Electrolytes for Fast-Charging Lithium-Ion Batteries. *Journal of the American Chemical Society* **2014,** *136* (13), 5039-5046.
28. Han, J.-G.; Lee, J. B.; Cha, A.; Lee, T. K.; Cho, W.; Chae, S.; Kang, S. J.; Kwak, S. K.; Cho, J.; Hong, S. Y.; Choi, N.-S., Unsymmetrical fluorinated malonatoborate as an amphoteric additive for high-energy-density lithium-ion batteries. *Energy & Environmental Science* **2018,** *11* (6), 1552-1562.
29. Lee, S. J.; Han, J.-G.; Park, I.; Song, J.; Cho, J.; Kim, J.-S.; Choi, N.-S., Effect of Lithium Bis(oxalato)borate Additive on Electrochemical Performance of Li1.17Ni0.17Mn0.5Co0.17O2 Cathodes for Lithium-Ion Batteries. *Journal of The Electrochemical Society* **2014,** *161* (14), A2012-A2019.
30. Fei, H. L.; Liu, X.; Li, H.; Wei, M. D., Enhanced electrochemical performance of ammonium vanadium bronze through sodium intercalation and optimization of electrolyte. *J Colloid Interf Sci* **2014,** *418*, 273-276.
31. Komaba, S.; Murata, W.; Ishikawa, T.; Yabuuchi, N.; Ozeki, T.; Nakayama, T.; Ogata, A.; Gotoh, K.; Fujiwara, K., Electrochemical Na Insertion and Solid Electrolyte Interphase for Hard-Carbon Electrodes and Application to Na-Ion Batteries. *Adv Funct Mater* **2011,** *21* (20), 3859-3867.
32. Jang, J. Y.; Lee, Y.; Kim, Y.; Lee, J.; Lee, S.-M.; Lee, K. T.; Choi, N.-S., Interfacial architectures based on a binary additive combination for high-performance Sn4P3 anodes in sodium-ion batteries. *Journal of Materials Chemistry A* **2015,** *3* (16), 8332-8338.
33. Ji, L.; Gu, M.; Shao, Y.; Li, X.; Engelhard, M. H.; Arey, B. W.; Wang, W.; Nie, Z.; Xiao, J.; Wang, C.; Zhang, J.-G.; Liu, J., Controlling SEI Formation on SnSb-Porous Carbon Nanofibers for Improved Na Ion Storage. *Advanced Materials* **2014,** *26* (18), 2901-2908.
34. Yabuuchi, N.; Matsuura, Y.; Ishikawa, T.; Kuze, S.; Son, J.-Y.; Cui, Y.-T.; Oji, H.; Komaba, S., Phosphorus Electrodes in Sodium Cells: Small Volume Expansion by Sodiation and the Surface-Stabilization Mechanism in Aprotic Solvent. *ChemElectroChem* **2014,** *1* (3), 580-589.
35. Komaba, S.; Yabuuchi, N.; Nakayama, T.; Ogata, A.; Ishikawa, T.; Nakai, I., Study on the Reversible Electrode Reaction of Na1–xNi0.5Mn0.5O2 for a Rechargeable Sodium-Ion Battery. *Inorganic Chemistry* **2012,** *51* (11), 6211-6220.
36. Hasa, I.; Passerini, S.; Hassoun, J., A rechargeable sodium-ion battery using a nanostructured Sb–C anode and P2-type layered Na0.6Ni0.22Fe0.11Mn0.66O2 cathode. *RSC Advances* **2015,** *5* (60), 48928-48934.
37. Kim, Y.; Kim, Y.; Choi, A.; Woo, S.; Mok, D.; Choi, N.-S.; Jung, Y. S.; Ryu, J. H.; Oh, S. M.;

Lee, K. T., Tin Phosphide as a Promising Anode Material for Na-Ion Batteries. *Advanced Materials* **2014,** *26* (24), 4139-4144.
38. Li, L.; Seng, K. H.; Li, D.; Xia, Y.; Liu, H. K.; Guo, Z., SnSb@carbon nanocable anchored on graphene sheets for sodium ion batteries. *Nano Research* **2014,** *7* (10), 1466-1476.
39. Li, W.; Chou, S.-L.; Wang, J.-Z.; Kim, J. H.; Liu, H.-K.; Dou, S.-X., Sn4+xP3 @ Amorphous Sn-P Composites as Anodes for Sodium-Ion Batteries with Low Cost, High Capacity, Long Life, and Superior Rate Capability. *Advanced Materials* **2014,** *26* (24), 4037-4042.
40. Kim, H.; Park, I.; Lee, S.; Kim, H.; Park, K.-Y.; Park, Y.-U.; Kim, H.; Kim, J.; Lim, H.-D.; Yoon, W.-S.; Kang, K., Understanding the Electrochemical Mechanism of the New Iron-Based Mixed-Phosphate Na4Fe3(PO4)2(P2O7) in a Na Rechargeable Battery. *Chemistry of Materials* **2013,** *25* (18), 3614-3622.
41. Hong, S. Y.; Kim, Y.; Park, Y.; Choi, A.; Choi, N.-S.; Lee, K. T., Charge carriers in rechargeable batteries: Na ions vs. Li ions. *Energy & Environmental Science* **2013,** *6* (7), 2067-2081.
42. Yui, Y.; Hayashi, M.; Nakamura, J., In situ Microscopic Observation of Sodium Deposition/Dissolution on Sodium Electrode. *Scientific Reports* **2016,** *6*, 22406.
43. Seh, Z. W.; Sun, J.; Sun, Y.; Cui, Y., A Highly Reversible Room-Temperature Sodium Metal Anode. *ACS Central Science* **2015,** *1* (8), 449-455.
44. Yoshida, K.; Nakamura, M.; Kazue, Y.; Tachikawa, N.; Tsuzuki, S.; Seki, S.; Dokko, K.; Watanabe, M., Oxidative-Stability Enhancement and Charge Transport Mechanism in Glyme–Lithium Salt Equimolar Complexes. *Journal of the American Chemical Society* **2011,** *133* (33), 13121-13129.
45. Lee, Y.; Lee, J.; Kim, H.; Kang, K.; Choi, N.-S., Highly stable linear carbonate-containing electrolytes with fluoroethylene carbonate for high-performance cathodes in sodium-ion batteries. *Journal of Power Sources* **2016,** *320*, 49-58.
46. Markevich, E.; Salitra, G.; Chesneau, F.; Schmidt, M.; Aurbach, D., Very Stable Lithium Metal Stripping–Plating at a High Rate and High Areal Capacity in Fluoroethylene Carbonate-Based Organic Electrolyte Solution. *ACS Energy Letters* **2017,** *2* (6), 1321-1326.
47. Iermakova, D. I.; Dugas, R.; Palacín, M. R.; Ponrouch, A., On the Comparative Stability of Li and Na Metal Anode Interfaces in Conventional Alkyl Carbonate Electrolytes. *Journal of The Electrochemical Society* **2015,** *162* (13), A7060-A7066.
48. Mogi, R.; Inaba, M.; Jeong, S.-K.; Iriyama, Y.; Abe, T.; Ogumi, Z., Effects of Some Organic Additives on Lithium Deposition in Propylene Carbonate. *Journal of The Electrochemical Society* **2002,** *149* (12), A1578-A1583.
49. Eshetu, G. G.; Grugeon, S.; Kim, H.; Jeong, S.; Wu, L.; Gachot, G.; Laruelle, S.; Armand, M.; Passerini, S., Comprehensive Insights into the Reactivity of Electrolytes Based on Sodium Ions. *ChemSusChem* **2016,** *9* (5), 462-471.
50. Oltean, V. A.; Philippe, B.; Renault, S.; Félix Duarte, R.; Rensmo, H.; Brandell, D., Investigating the Interfacial Chemistry of Organic Electrodes in Li- and Na-Ion Batteries. *Chemistry of Materials* **2016,** *28* (23), 8742-8751.
51. Vogt, L. O.; El Kazzi, M.; Jämstorp Berg, E.; Pérez Villar, S.; Novák, P.; Villevieille, C., Understanding the Interaction of the Carbonates and Binder in Na-Ion Batteries: A Combined Bulk and Surface Study. *Chemistry of Materials* **2015,** *27* (4), 1210-1216.
52. Nakai, H.; Kubota, T.; Kita, A.; Kawashima, A., Investigation of the Solid Electrolyte Interphase Formed by Fluoroethylene Carbonate on Si Electrodes. *Journal of The Electrochemical Society* **2011,** *158* (7), A798-A801.
53. Schroder, K.; Alvarado, J.; Yersak, T. A.; Li, J.; Dudney, N.; Webb, L. J.; Meng, Y. S.; Stevenson, K. J., The Effect of Fluoroethylene Carbonate as an Additive on the Solid Electrolyte Interphase on Silicon Lithium-Ion Electrodes. *Chemistry of Materials* **2015,** *27* (16), 5531-5542.
54. Dahbi, M.; Yabuuchi, N.; Fukunishi, M.; Kubota, K.; Chihara, K.; Tokiwa, K.; Yu, X.-f.; Ushiyama, H.; Yamashita, K.; Son, J.-Y.; Cui, Y.-T.; Oji, H.; Komaba, S., Black Phosphorus as a High-Capacity, High-Capability Negative Electrode for Sodium-Ion Batteries: Investigation of the Electrode/Electrolyte Interface. *Chemistry of Materials* **2016,** *28* (6), 1625-1635.

55. Okuno, Y.; Ushirogata, K.; Sodeyama, K.; Tateyama, Y., Decomposition of the fluoroethylene carbonate additive and the glue effect of lithium fluoride products for the solid electrolyte interphase: an ab initio study. *Physical Chemistry Chemical Physics* **2016,** *18* (12), 8643-8653.
56. Simone, V.; Lecarme, L.; Simonin, L.; Martinet, S., Identification and Quantification of the Main Electrolyte Decomposition By-product in Na-Ion Batteries through FEC: Towards an Improvement of Safety and Lifetime. *Journal of The Electrochemical Society* **2017,** *164* (2), A145-A150.
57. Liu, Q.; Mu, D.; Wu, B.; Wang, L.; Gai, L.; Wu, F., Density Functional Theory Research into the Reduction Mechanism for the Solvent/Additive in a Sodium-Ion Battery. *ChemSusChem* **2017,** *10* (4), 786-796.
58. Kumar, H.; Detsi, E.; Abraham, D. P.; Shenoy, V. B., Fundamental Mechanisms of Solvent Decomposition Involved in Solid-Electrolyte Interphase Formation in Sodium Ion Batteries. *Chemistry of Materials* **2016,** *28* (24), 8930-8941.
59. Abdul-Karim, R.; Hameed, A.; Malik, M. I., Ring-opening polymerization of ethylene carbonate: comprehensive structural elucidation by 1D & 2D-NMR techniques, and selectivity analysis. *RSC Advances* **2017,** *7* (19), 11786-11795.
60. Jo, H.; Kim, J.; Nguyen, D.-T.; Kang, K. K.; Jeon, D.-M.; Yang, A. R.; Song, S.-W., Stabilizing the Solid Electrolyte Interphase Layer and Cycling Performance of Silicon–Graphite Battery Anode by Using a Binary Additive of Fluorinated Carbonates. *The Journal of Physical Chemistry C* **2016,** *120* (39), 22466-22475.
61. El Ouatani, L.; Dedryvère, R.; Siret, C.; Biensan, P.; Reynaud, S.; Iratçabal, P.; Gonbeau, D., The Effect of Vinylene Carbonate Additive on Surface Film Formation on Both Electrodes in Li-Ion Batteries. *Journal of The Electrochemical Society* **2009,** *156* (2), A103-A113.
62. Etacheri, V.; Haik, O.; Goffer, Y.; Roberts, G. A.; Stefan, I. C.; Fasching, R.; Aurbach, D., Effect of Fluoroethylene Carbonate (FEC) on the Performance and Surface Chemistry of Si-Nanowire Li-Ion Battery Anodes. *Langmuir* **2012,** *28* (1), 965-976.
63. Winkler, V.; Kilibarda, G.; Schlabach, S.; Szabó, D. V.; Hanemann, T.; Bruns, M., Surface Analytical Study Regarding the Solid Electrolyte Interphase Composition of Nanoparticulate SnO2 Anodes for Li-Ion Batteries. *The Journal of Physical Chemistry C* **2016,** *120* (43), 24706-24714.
64. Wang, Z.; Huang, X.; Chen , L., Characterization of Spontaneous Reactions of LiCoO2 with Electrolyte Solvent for Lithium-Ion Batteries. *Journal of The Electrochemical Society* **2004,** *151* (10), A1641-A1652.
65. Aurbach, D.; Chusid , O., The Study of Surface Films Formed on Lithium and Noble Metal Electrodes in Polar Aprotic Systems By the Use of In Situ Fourier Transform Infrared Spectroscopy. *Journal of The Electrochemical Society* **1993,** *140* (1), L1-L4.
66. Osaka, T.; Momma, T.; Matsumoto, Y.; Uchida, Y., Surface Characterization of Electrodeposited Lithium Anode with Enhanced Cycleability Obtained by CO 2 Addition. *Journal of The Electrochemical Society* **1997,** *144* (5), 1709-1713.
67. Suo, L.; Hu, Y.-S.; Li, H.; Armand, M.; Chen, L., A new class of Solvent-in-Salt electrolyte for high-energy rechargeable metallic lithium batteries. *Nature Communications* **2013,** *4*, 1481.
68. Ma, Q.; Fang, Z.; Liu, P.; Ma, J.; Qi, X.; Feng, W.; Nie, J.; Hu, Y.-S.; Li, H.; Huang, X.; Chen, L.; Zhou, Z., Improved Cycling Stability of Lithium-Metal Anode with Concentrated Electrolytes Based on Lithium (Fluorosulfonyl)(trifluoromethanesulfonyl)imide. *ChemElectroChem* **2016,** *3* (4), 531-536.
69. Younesi, R.; Veith, G. M.; Johansson, P.; Edstrom, K.; Vegge, T., Lithium salts for advanced lithium batteries: Li-metal, Li-O-2, and Li-S. *Energy & Environmental Science* **2015,** *8* (7), 1905-1922.
70. Jeong, S. K.; Seo, H. Y.; Kim, D. H.; Han, H. K.; Kim, J. G.; Lee, Y. B.; Iriyama, Y.; Abe, T.; Ogumi, Z., Suppression of dendritic lithium formation by using concentrated electrolyte solutions. *Electrochemistry Communications* **2008,** *10* (4), 635-638.

71. Togasaki, N.; Momma, T.; Osaka, T., Enhanced cycling performance of a Li metal anode in a dimethylsulfoxide-based electrolyte using highly concentrated lithium salt for a lithium-oxygen battery. *Journal of Power Sources* **2016,** *307*, 98-104.
72. Qian, J. F.; Xu, W.; Bhattacharya, P.; Engelhard, M.; Henderson, W. A.; Zhang, Y. H.; Zhang, J. G., Dendrite-free Li deposition using trace-amounts of water as an electrolyte additive. *Nano Energy* **2015,** *15*, 135-144.
73. Zheng, J.; Engelhard, M. H.; Mei, D.; Jiao, S.; Polzin, B. J.; Zhang, J.-G.; Xu, W., Electrolyte additive enabled fast charging and stable cycling lithium metal batteries. *Nature Energy* **2017,** *2*, 17012.
74. Liang, X.; Wen, Z. Y.; Liu, Y.; Wu, M. F.; Jin, J.; Zhang, H.; Wu, X. W., Improved cycling performances of lithium sulfur batteries with LiNO3-modified electrolyte. *Journal of Power Sources* **2011,** *196* (22), 9839-9843.
75. Wu, F.; Qian, J.; Chen, R.; Lu, J.; Li, L.; Wu, H.; Chen, J.; Zhao, T.; Ye, Y.; Amine, K., An Effective Approach To Protect Lithium Anode and Improve Cycle Performance for Li–S Batteries. *ACS Applied Materials & Interfaces* **2014,** *6* (17), 15542-15549.
76. Li, W.; Yao, H.; Yan, K.; Zheng, G.; Liang, Z.; Chiang, Y.-M.; Cui, Y., The synergetic effect of lithium polysulfide and lithium nitrate to prevent lithium dendrite growth. *Nature Communications* **2015,** *6*, 7436.
77. Ding, F.; Xu, W.; Chen, X.; Zhang, J.; Engelhard, M. H.; Zhang, Y.; Johnson, B. R.; Crum, J. V.; Blake, T. A.; Liu, X.; Zhang, J.-G., Effects of Carbonate Solvents and Lithium Salts on Morphology and Coulombic Efficiency of Lithium Electrode. *Journal of The Electrochemical Society* **2013,** *160* (10), A1894-A1901.
78. Miao, R. R.; Yang, J.; Xu, Z. X.; Wang, J. L.; Nuli, Y.; Sun, L. M., A new ether-based electrolyte for dendrite-free lithium-metal based rechargeable batteries. *Scientific Reports* **2016,** *6*.
79. Yu, H.; Zhao, J.; Ben, L.; Zhan, Y.; Wu, Y.; Huang, X., Dendrite-Free Lithium Deposition with Self-Aligned Columnar Structure in a Carbonate–Ether Mixed Electrolyte. *ACS Energy Letters* **2017,** *2* (6), 1296-1302.
80. Becke, A. D., Density-functional thermochemistry. III. The role of exact exchange. *The Journal of Chemical Physics* **1993,** *98* (7), 5648-5652.
81. Stephens, P. J.; Devlin, F. J.; Chabalowski, C. F.; Frisch, M. J., Ab-Initio Calculation of Vibrational Absorption and Circular-Dichroism Spectra Using Density-Functional Force-Fields. *J Phys Chem-Us* **1994,** *98* (45), 11623-11627.
82. Tkatchenko, A.; Scheffler, M., Accurate Molecular Van Der Waals Interactions from Ground-State Electron Density and Free-Atom Reference Data. *Physical Review Letters* **2009,** *102* (7), 073005.
83. Halgren, T. A.; Lipscomb, W. N., The synchronous-transit method for determining reaction pathways and locating molecular transition states. *Chemical Physics Letters* **1977,** *49* (2), 225-232.
84. Govind, N.; Petersen, M.; Fitzgerald, G.; King-Smith, D.; Andzelm, J., A generalized synchronous transit method for transition state location. *Comp Mater Sci* **2003,** *28* (2), 250-258.
85. Delley, B., From molecules to solids with the DMol3 approach. *The Journal of Chemical Physics* **2000,** *113* (18), 7756-7764.
86. Klamt, A.; Schuurmann, G., Cosmo - a New Approach to Dielectric Screening in Solvents with Explicit Expressions for the Screening Energy and Its Gradient. *J Chem Soc Perk T 2* **1993,** (5), 799-805.
87. Noguchi, T.; Hasegawa, T.; Yamauchi, H.; Yamazaki, I.; Utsugi, K., Effect of Using Fluorinated Ether and Sulfone as Electrolyte Solvents for Lithium Ion Batteries with Lithium-Rich Layered Cathodes and Silicon Oxide Anodes. *ECS Transactions* **2017,** *80* (10), 291-303.
88. Hall, D. S.; Self, J.; Dahn, J. R., Dielectric Constants for Quantum Chemistry and Li-Ion Batteries: Solvent Blends of Ethylene Carbonate and Ethyl Methyl Carbonate. *The Journal of Physical Chemistry C* **2015,** *119* (39), 22322-22330.
89. Kobayashi, M.; Inoguchi, T.; Iida, T.; Tanioka, T.; Kumase, H.; Fukai, Y., Development of

direct fluorination technology for application to materials for lithium battery. *J Fluorine Chem* **2003,** *120* (2), 105-110.
90. Choudhury, S.; Archer, L. A., Lithium Fluoride Additives for Stable Cycling of Lithium Batteries at High Current Densities. *Advanced Electronic Materials* **2016,** *2* (2), 1500246.
91. Yoo, D.-J.; Yang, S.; Yun, Y. S.; Choi, J. H.; Yoo, D.; Kim, K. J.; Choi, J. W., Tuning the Electron Density of Aromatic Solvent for Stable Solid-Electrolyte-Interphase Layer in Carbonate-Based Lithium Metal Batteries. *Advanced Energy Materials* **2018,** *8* (33), 1802365.

ACKNOWLEDGEMENTS

오랜 기간 동안 연구에 대한 깊은 가르침을 주신 최남순 교수님께 가장 먼저 감사의 말씀을 드리고 싶습니다. 석박통합과정 중 연구실 내에 박사과정 선배님이 없는 저에게 교수님께서 저의 롤모델이셨습니다. 작은 부분까지 섬세하게 지도를 해 주셔서 정말 감사드립니다. 또한 저의 학위 논문 심사에 아낌없이 조언을 주신 정경민 교수님, 홍성유 교수님, 강석주 교수님, 이현욱 교수님께 감사의 말씀드립니다.

언제나 응원해주신 아버지와 어머니, 누나에게도 감사의 말씀드립니다. 자주 찾아 뵙지 못한 저에게 가족과의 전화는 항상 큰 힘이 되었습니다.

2014 년도에 함께 대학원에 입학하여 연구실에서 저와 함께 가장 오랜 시간을 보낸 정구에게도 고마움을 전합니다. 또한, 리튬 메탈과 소듐 메탈 배터리 실험을 서로 고민하며 즐겁게 진행한 재기, 정민, 영준이에게도 고마움을 전합니다. 무엇보다, 에너지 재료 연구실 랩원 모두에게도 고마움을 전하고 싶습니다. 랩원 모두가 열심히 랩실 생활을 했기 때문에 연구실의 분위기가 항상 밝을 수 있었으며, 서로에게 힘이 될 수 있었습니다.